

ABSTRACT

YILDIZ, OZKAN. High Performance Hybrid Fabrics Containing Carbon Nanotubes. (Under the direction of Dr. Philip D. Bradford).

In response to the ever-growing demand within the textile market, manufacturing hybrid materials using nonwoven fabrics with nanomaterials and nanotechnology has become immensely important. Thus, these hybrid materials will increasingly be used in a diverse range of applications in the future. The use of nanotechnology for the functionalization of materials made with traditional textile techniques provides certain unique characteristics, such as sensory properties, electrical conductivity, and other features. This use of nanotechnology has been achieved through such developments as new materials, fibers, conducting polymers, and carbon nanotubes (CNTs). Owing to their small size, lightweight, and extra-ordinary mechanical, electrical and thermal properties, along with their large aspect ratio and higher specific surface area, CNTs have had significant impact on products that are manufactured in the textile industry. Utilizing CNTs with conventional micro or nano-sized fiber nonwovens is still challenging, yet highly desirable in various fields.

In current literature, there are many studies that utilize CNTs with micro or nano-sized fiber textile materials. In some of this research, CNTs were directly grown on the surface of micro-sized glass or nickel fibers. In others, CNTs were dispersed in polymer solution, which was then electrospun to produce high tensile strength and electrical conductive nonwoven fabrics. However, it is necessary to investigate alternative methods in order to advance the field of CNT-textile hybrid fabrics.

Chemical vapor deposition (CVD) processes, where catalyst nanoparticles are deposited on a substrate, are often used to produce vertically aligned CNT arrays. These one-millimeter long CNTs are highly drawable in nature. In this dissertation, CNT sheets have been incorporated with conventional micro-sized polymeric fibers to investigate aerosol filtration characteristics. Since CNT sheets have small diameters, low basis weight, low packing density and high porosity, these sheets are a great candidate for air filtration structures. The results showed that the CNT-nonwoven hybrid fabric exhibited excellent filtration properties. In addition, the fabric porosity and also the architecture of CNTs in the fabric have been found to be important and that further improvements could be made through further engineering the multi-layered fabric structure.

CNTs have been dispersed into various polymer solutions in order to improve tensile properties and increase the electrical conductivity of electrospun nanofiber nonwovens. However, several factors significantly influence the final nanofiber nonwovens properties. Stable nanoscale hybrid fabrics, containing both polymer nanofibers and separate and distinct carbon nanotubes (CNTs), are highly desirable but very challenging to produce. In this dissertation, the novel CNT-polymer hybrid nonwoven fabrics were created by simultaneously electrospinning nanofibers onto aligned CNT sheets which were drawn and collected on a grounded, rotating mandrel. The filtration characteristics and barrier properties of hybrid fabrics were evaluated.

Significant efforts have been made to explore high specific capacity lithium-ion battery electrodes. Silicon anodes have been found previously to have limited application in

commercial batteries due to the significant volume change (up to 400%) of silicon during cycling, which hinder silicon's application into lithium-ion batteries. Therefore, in order to solve the problems caused by the silicon volume expansion, the hybridization method was used to prepare silicon-carbon nanotube (CNT) hybrid anode architecture. The novel freestanding, binder free CNT-Si-C sheet hybrid exhibited improved performance in terms of excellent cycling capacity, coulombic efficiency, and good capacity retention.

© Copyright 2016 by Ozkan Yildiz

All Rights Reserved

High Performance Hybrid Fabrics Containing Carbon Nanotubes

by
Ozkan Yildiz

A dissertation submitted to the Graduate Faculty of
North Carolina State University
in partial fulfillment of the
requirements for the degree of
Doctor of Philosophy

Fiber and Polymer Science

Raleigh, North Carolina

2016

APPROVED BY:

Dr. Philip D. Bradford
Chair of Advisory Committee

Dr. Jesse Jur

Dr. Xiangwu Zhang

Dr. Saad Khan

DEDICATION

To my parents, Emine, Ahmet, Mehmet, and Mustafa, and my fiance Ozen, whose love and support were essential in the preparation of this dissertation.

BIOGRAPHY

Ozkan YILDIZ was born in Kastamonu, Turkey, January 13th 1984. He grew up in Karabuk where he graduated from high school in 2002. The following fall he started his college career at Uludag University. He graduated in 2006 with a B.S. in Textile Engineering. Few months later, he got a scholarship from Turkish government to study master and Ph.D. in the U.S. He came to Syracuse to study English in 2007. He started to study master at Auburn University. He graduated in 2010 with a Master degree in Polymer and Fiber Engineering. Then he moved to Raleigh, North Carolina to pursue with his Ph.D. in Fiber and Polymer Science at North Carolina State University. He joined Dr. Philip Bradford's research group as a Research Assistance, where he investigated high performance hybrid fabrics containing carbon nanotubes.

ACKNOWLEDGMENTS

First and foremost, I would like to sincerely thank my advisor, Dr. Philip Bradford, for providing me the opportunity to start my graduate career in his group and for the time and guidance he provided along the way. I would also like to acknowledge continues support of my advisory committee- Dr. Jesse Jur, Dr. Xiangwu Zhang and Dr. Saad Khan.

I also want to thank my former and current lab mates. Dr. Kelly Stano and Can Tang, thank you for mentoring me at the start of my research career and guiding me throughout. Dr. Kun Fu, Dr. Shaghayegh Faraji, Dr. James Stahl, Hardik Bhanushali, Spencer Barbour, Brian Wells, Karim Aly, Ang Li and Murphy Carrol, you guys were great lab mates. I also would like to thank Xiaomeng Fang for her great help in my research.

I would like to thank my parents for their support and encouragement throughout many years of my academic endeavors. Last but not the least, I would like to thank my fiance, Ozen Guven, for her love and patience which made the completion of this dissertation possible.

TABLE OF CONTENTS

Chapter 1	Introduction.....	1
Chapter 2	Literature Review	6
2.1	Carbon Nanotubes.....	6
2.1.1	Carbon Nanotube Properties	6
2.1.2	Carbon Nanotube Synthesis	8
2.1.3	Vertically Aligned Spinnable Carbon Nanotubes	10
2.2	Aerosol Filtration	14
2.2.1	The Importance of Aerosol Filters	14
2.2.2	Filtration Mechanisms.....	15
2.2.3	Evaluation of Filtration Performance.....	18
2.2.3.1	Nonwoven Filters	20
2.2.3.2	Electrospun Filters.....	21
2.2.3.3	Carbon Nanotube Filters.....	24
2.2.4	Existing Filtration Theories.....	30
2.2.4.1	Single Fiber Theory	31
2.2.4.2	Cell Model	32
2.2.5	The Parameters that Affect Filtration Properties	35

2.2.5.1	Fiber Orientation.....	35
2.2.5.2	Fiber Diameter.....	37
2.2.5.2.1	Knudsen Number.....	37
2.2.5.2.2	Peclet Number.....	41
2.2.5.3	Packing Density.....	43
2.2.6	Theoretical Calculations.....	44
2.2.7	Pressure Drop.....	45
2.3	CNT Reinforced Nanofiber Fabrics.....	47
2.3.1	Mechanical Properties of Nano sized Fibers.....	47
2.3.2	Improvement of Mechanical Properties of Nano-fiber Nonwovens.....	48
2.3.2.1	Traditional Methods.....	48
2.3.2.2	CNT Reinforced Polymer Nanofibers.....	50
2.3.3	Challenge of Using CNTs to Reinforce Nonwoven Mats.....	51
2.3.3.1	Dispersion and Alignment of CNTs in Polymer Matrix.....	51
2.3.3.2	CNTs Weight & Volume Fraction.....	54
2.3.3.3	Bead Formation.....	56
Chapter 3	Experimental.....	65
3.1	Materials and Methods.....	65

3.1.1	Synthesis of Spinnable MWCNT Arrays	65
3.1.2	Preparation of CNT sheet – Nonwoven Aerosol Filter Structure	65
3.1.3	Preparation of CNT sheet – Polymer Nanofiber Hybrid Fabric	66
3.1.4	Plasma Surface Modification	68
3.2	Characterization	69
3.2.1	Microstructure Analysis	69
3.2.2	Chemical Analysis	70
3.2.3	Electrical Analysis	70
3.2.4	Mechanical Analysis	70
3.2.5	Aerosol Filtration Testing	71
3.2.6	Contact Angle Measurements	71
3.2.7	Moisture Vapor Transmission Rate (MVTR) Test	71
3.2.8	Electrochemical Evaluation	72
Chaper 4 Aligned Carbon Nanotube Sheet High Efficiency Particulate Air Filters.		73
4.1	Introduction.....	74
4.2	Materials and Methods.....	77
4.2.1	Materials and Instrumentation.....	77
4.2.2	CNT Array Synthesis and CNT Sheet Analysis	77

4.2.3	Preparation of CNT Sheet Aerosol Filter Structures.....	79
4.2.4	Filtration Evaluation.....	82
4.3	Results and Discussion	83
4.4	Conclusions.....	97
Chaper 5 Multi-layer CNT Sheet – PET Nonwoven Fabric Structures for High-Performance Aerosol Filtration.....		98
5.1	Introduction.....	99
5.2	Materials and Methods.....	102
5.2.1	Materials and Instrumentation.....	102
5.2.2	CNT Array Synthesis and CNT Sheet Analysis	102
5.2.3	Preparation of CNT Sheet Aerosol Filter Structure	104
5.2.4	Filtration Evaluation.....	107
5.3	Results and Discussion	107
5.4	Conclusion	117
Chaper 6 High Performance Carbon Nanotube – Polymer Nanofiber Hybrid Fabrics		119
6.1	Introduction.....	120
6.2	Materials and Methods.....	123

6.2.1	CNT Synthesis	123
6.2.2	Electrospinning Process and Characterization.....	123
6.2.3	Physical Testing	124
6.2.4	Aerosol Filtration Testing.....	125
6.2.5	Plasma Functionalization	126
6.2.6	Moisture Vapor Transmission Rate (MVTR) Test	127
6.2.7	Contact Angle Measurements	127
6.3	Results and Discussion	128
6.4	Conclusions.....	143
Chaper 7 Flexible Si – CNT Hybrid Anode Architecture for Lithium-Ion Battery		
Electrodes Based on a Hybrid CNT-Nanofiber Structure		
		145
7.1	Introduction.....	146
7.2	Experimental.....	149
7.2.1	CNT Synthesis	149
7.2.2	Hybrid Fabric Preparation.....	150
7.2.3	Characterization	151
7.2.4	Electrochemical Evaluation	152
7.3	Results and Discussion	152

7.4	Conclusions.....	166
Chapter 8	Final Conclusions and Future Work.....	168
8.1	Conclusions.....	168
8.2	Future Work.....	170
REFERENCES.....		173

LIST OF FIGURES

Figure 2.1 a) Schematic diagram of how a graphite sheet is wrapped to form a carbon nanotube, b) illustration of atomic structure of armchair, c) illustration of atomic structure of zig-zag nanotube ^[36]	7
Figure 2.2 TEM images showing carbon nanotube nucleation from iron carbide nanoparticle ^[45]	9
Figure 2.3 Schematic picture of the mechanism for drawing CNT from vertically aligned arrays ^[50]	11
Figure 2.4 The SEM image showing misalignment of drawn CNT sheet	12
Figure 2.5 The common aerosol particles based on their sizes ^[66]	15
Figure 2.6 Particle depositions on the filter Structure ^[67]	17
Figure 2.7 Filter efficiency for individual single fiber mechanisms and total efficiency ^[68] ..	18
Figure 2.8 Schematic of the electrospinning process ^[85]	22
Figure 2.9 A layer of electrospun nanofiber mat (top) on a supporting material (bottom) ^[13] ..	23
Figure 2.10 a) The cross section view of CNTs coated film onto cellulose layer ^[90] b) SEM image of CNTs grown on glass fiber ^[14]	26
Figure 2.11 Schematic of the catalyst loading on a quartz fiber filter and growth of the CNTs ^[97]	27
Figure 2.12 Cell Model	33

Figure 2.13 Kuwabara flow cell ^[103]	33
Figure 2.14 A schematic of fiber orientations a) uni-directional random fiber arrangement, b) random layered (planar) fiber arrangement, c) three-dimensionally fiber arrangement ^[110] ...	36
Figure 2.15 The Kuwabara flow field about a fiber based on the flow regimes with $K_n = 10^{-3}$, 10^{-1} , 10, from left to right ^[69]	41
Figure 2.16 Ideal polymer chains model to produce high strength and high modulus fibers ^[87]	49
Figure 2.17 The SEM image of CNT-PVA electrospun fiber ^[131]	51
Figure 2.18 TEM images of PMMA-CNT nanofibers a) 1 μm scale bar, b) 200 nm scale bar ^[132]	53
Figure 2.19 Optical microscopy on dispersion of CNTs into the polymer solution a) below rheological percolation (1% MWNTs), b) above percolation (4% MWNTs) ^[27]	54
Figure 2.20 a) TEM image of 20% CNT ^[126] , b) TEM image of 5% CNT into polymer solution ^[29]	55
Figure 2.21 SEM images of a) 1% CNT, b) 7% CNT polymer electrospun nonwoven mat ^[27]	56
Figure 2.22The optical microscopy of CNT-PS electrospun nanofibers a) 3% CNT, b) 5% CNT ^[27]	57
Figure 4.1 (a) CNT sheet being drawn from the array using tweezers, (b) SEM image of the side view of the CNT sheet showing the approximate thickness and low density structure, (c)	

High magnification SEM image of the top of the CNT sheet showing the spacing between CNTs and (d) TEM image of CNTs from the sheet..... 79

Figure 4.2 Preparing filters by (a) winding CNT sheets onto the polypropylene fabric, (b) placing CNT sheet - polypropylene fabric layered structure onto a calendaring plate with hole in the middle, (c) covering with a second layer of polypropylene fabric and second calendaring plate and (d) the final calendared fabric with pristine multi-layer structure in which the middle square section was not exposed to heat or pressure. 81

Figure 4.3 SEM images, at two different magnifications, of a-b) polypropylene melt blown fabric (control sample), c-d) 1-layer CNT sheet on the polypropylene fabric, e-f) 3-layer CNT sheet on the polypropylene fabric. 86

Figure 4.4 CNT sheet - polypropylene nonwoven fabric filters with increasing number of CNT sheet layers, evaluated for particle penetration percentage for a range of particle sizes at a face velocity of 10 cm/s. 88

Figure 4.5 (a) SEM and (b) photographic images of the 3-layer CNT filter structure with the cross-ply geometry..... 89

Figure 4.6 The filtration performance of filters consisting of 2-layer, 3-layer, 2-layer cross-ply, and 3-layer cross-ply CNT sheet orientations at a face velocity of 10 cm/s. 90

Figure 4.7 Particle penetration fraction of the different structures as a function of pressure drop at 0.3 μm particle size and 10 cm/s face velocity..... 92

Figure 4.8 Quality factor as a function of DOP particle size, ranging from 0.01-0.3 μm , at 10 cm/s face velocity. 93

Figure 4.9 Comparison of particle penetration vs. pressure drop from nanofiber filters, including CNT coated filters, from the literature. These points were taken from studies using a face velocity of 10 cm/s or lower and with a particle size of 0.3 μm 94

Figure 5.1 a) Aligned CNT sheet was drawn from the array using tweezers, b) the cross-section of the CNT sheet showing the approximate thickness, c) high magnification SEM image of single layer CNT sheet, d) TEM image of CNTs from the sheet. 104

Figure 5.2 Preparing filters by (a) winding CNT sheets onto the PET highly porous fabric, (b) placing CNT sheet – PET multi-layered fabric onto a calendaring plate with hole in the middle, (c) covering with a second calendaring plate and (d) the final calendared fabric with pristine multi-layered structure in which the middle square section was not exposed to heat or pressure. 106

Figure 5.3 SEM images at two different magnifications of (a and b) porous PET melt blown fabric, (c and d) low porosity PET melt blown fabric, and (e and f) CNT sheet structure... 109

Figure 5.4 Filtration performance of a) CNT sheet – high porosity PET melt blown multi-layer filter, b) CNT sheet – low porosity PET melt blown multi-layer filter at face velocity of 5 cm/s. 112

Figure 5.5 The Filtration performance of filters consisting of 3-separated CNT high porosity, 3-separated CNT low porosity, 3-combined CNT high porosity and 3-combined CNT low porosity multi-layer structure at a face velocity of 5 cm/s. 113

Figure 5.6 Particle penetration percentage of a) high porosity CNT sheet multi-layer filter, b) low porosity CNT sheet multi-layer filter as a function of pressure drop at 0.3 μm particle size and 5 cm/s face velocity. 115

Figure 5.7 Quality factor as a function of particle sizes, ranging from 3-800 nm, at a 5 cm/s face velocity. 116

Figure 6.1 Schematic of the hybrid fabric production process where electrospun fibers are taken up simultaneously with aligned CNT sheets. 128

Figure 6.2 a) Setup of the hybrid nanofiber processing equipment, b) CNT – polymer hybrid nonwoven fabrics created with varying weight percentages of CNTs, c) SEM image of the hybrid fabric shows an order of magnitude size difference between CNTs and electrospun nanofibers, d) SEM image showing the same hybrid after calendaring with the melted nanofibers bonding the CNTs together. 130

Figure 6.3 (a) Tensile mechanical properties of the as-produced hybrid fabrics with different CNT loadings, (b) Tensile mechanical properties of the hybrid fabrics after consolidation under pressure, (c) Tensile mechanical properties of the hybrid fabrics after calendaring at 70 $^{\circ}\text{C}$, (d) Comparison of specific strength between control sample and hybrid fabrics, (e) Comparison of our best mechanical properties (calendered, 60% CNT hybrid fabric) to thermally bonded nonwovens from references^[206–212], (f) Strength increases seen for our hybrids as compared to electrospun fabrics with CNTs in the spinning solution from references^[20,23,27,126,130,133,137,142,205,213] 134

Figure 6.4 Electrical conductivity of the as-produced, consolidated and calendared hybrid fabrics and pure as-produced and consolidated CNT sheet samples. 136

Figure 6.5 (a) The hybrid fabrics with different CNT fiber loading, evaluated for particle penetration for a range of particle sizes at a face velocity of 15 cm/s, (b) The hybrid fabrics with different CNT fiber loading after consolidated under pressure, evaluated for particle penetration for a range of particle sizes at a face velocity of 15 cm/s, (c) Particle penetration fraction of the hybrid fabrics at different CNT fiber loading before and after consolidation as a function of pressure drop at 0.3 μm particle size and 15 cm/s face velocity, (d) Quality factor as a function of DOP particle size, ranging from 0.01 to 0.3 μm , at 15 cm/s face velocity..... 140

Figure 6.6 a) MVP results for hybrid fabrics, b) A droplet of hexadecane on a 60% CNT consolidated hybrid fabric..... 141

Figure 7.1 Schematic for producing novel CNT-Si and CNT-Si-C sheet structures. CNT-PMMA-Si hybrid fabric was prepared by simultaneously electrospinning PMMA + Si nanofibers onto aligned CNT sheets, which were drawn and collected on a grounded, rotating mandrel. The self-supported hybrid fabric was treated at elevated temperature to decompose PMMA electrospun fibers. A continuous novel CNT-Si-structure was obtained. Then the novel architecture of CNT-Si sheet was coated pyrolytic carbon as the main active anode material for the LIBs. 154

Figure 7.2 (a) Photographic image of the CNT-PMMA-Si hybrid fabric processing setup, (b) Photographic image for each processing method. From left to right, the fabrics are: (1) as-

produced CNT-PMMA-Si hybrid fabric; (2) after decomposition of electrospun PMMA fabric (CNT-Si); and (3) after carbon coating sample (CNT-Si-C), (c) Photographs of a flexible novel CNT-Si-C sheet composite with different folded structure, (d) A free-standing and binder-free electrode for lithium ion cell testing..... 156

Figure 7.3 Structures of CNT-PMMA-Si, CNT-Si, and CNT-Si-C sheets. Figure a-b is the CNT-PMMA-Si hybrid nonwoven structure at high and low magnification. Figure c-d images of the CNT-Si sheet structure at high and low magnification. Figure e-f are the images of CNT-Si-C sheet structure at high and low magnification. 158

Figure 7.4 TEM images of flexible, novel structures (a) CNT-Si sheet and (b) CNT-Si-C sheet hybrids. 159

Figure 7.5 (a) Raman spectra of novel CNT-Si and CNT-Si-C sheet hybrids to examine characteristic Si peaks, (b) Raman spectra of novel CNT-Si and CNT-Si-C sheet hybrids to examine characteristic carbon peaks, (c) WAXD patterns of flexible novel (1) CNT-Si-C sheet and (2) CNT-Si sheet hybrids. 161

Figure 7.6 Galvanostatic charge-discharge profiles of novel (a) CNT sheet, (b) CNT-Si sheet, and (c) CNT-Si-C sheet composites. 163

Figure 7.7 Cycling performances and coulombic efficiencies of CNT sheet, CNT-Si, and CNT-Si-C sheet hybrids..... 165

Figure 7.8 Rate capability and coulombic efficiency of CVD pyrolytic carbon coated novel CNT-Si-C sheet hybrid cycled at different current densities..... 166

LIST OF TABLES

Table 2.1 The filtration performance of air filters based on CNTs.	29
Table 2.2 Relationship between Knudsen number, fiber diameter, and flow regimes.	38
Table 4.1 Experimental and calculated pressure drop values for the CNT sheet filters.....	95

Chapter 1 Introduction

There has been rapid development of nanoscience and nanotechnology over the past two decades and, during this time, great progress has been made in preparation and characterization of nanomaterials. As an important one-dimensional nanomaterial, nanofibers are able to form a highly porous nonwoven mat and their large surface to volume ratio improves performance for many applications^[1]. A variety of nanofibers can be made for a wide range of applications ranging from medical to consumer products and from industrial to high-tech applications^[2]. Due to high surface area and small fiber diameter, nanofiber nonwovens have greatly attracted attention in filtration area as well. Nanofiber nonwovens have emerged as a promising media, because it can provide greater filtration efficiency and higher performance than conventional fibers.

In the past several decades, aerosol filtration has become more significant in human life since the quality of environment has seriously deteriorated due to rapid urbanization and industrialization^[3,4]. Fine particles, particulate matter that has an aerodynamic diameter less than 2.5 μm , are one of the most serious sources of air pollution which causes acute and chronic health problems, such as lung cancer, bronchitis, aggravating preexisting heart and lung diseases or asthmatic attacks^[5-7]. The main sources of these fine particles are industrial activities, intensive road transportation, biomass burning, secondary nitrate and secondary sulfates^[8,9]. Nowadays, nonwoven fibrous membrane based on glass, polyester, polyethylene (PE), polypropylene (PP), and aramid fibers are widely used in aerosol filtration applications^[10]. However, using conventional fibers for filtration have many structural and

performance disadvantages, such as large fiber diameter, non-uniform fiber diameter, packing density variation, large pore size, low filtration efficiency, and high basis weight^[11,12]. It is well-known that the smaller the fiber diameter, the better filtration performance. Nanofibers boost the filtration efficiency and provide enhanced slip-effect that causes less resistance across the filter media. Several different techniques have been adopted to produce nanofibrous membranes. Among these techniques, nanofiber nonwoven produced via electrospinning is simple, versatile, predominant commercial method to produce polymer fibers diameters down to 100 nm in a continuous process and at a long length scale^[11]. However, even though electrospinning is one of the most promising technologies for lightweight, low basis weight and high efficiency filters, the high pressure drop they produce is the biggest challenge of this method^[12-15].

Electrospinning is a processing method that uses an electric field to draw a polymer solution from the tip of a capillary to a collector. When a voltage is applied to the polymer solution, it causes a jet of the solution to be drawn toward a grounded collector. The fine jets evaporate the polymer solution, and then polymeric fibers are formed which can be collected on a web. Producing smaller fiber diameter is important for aerosol filtration due to high surface area and smaller pore sizes. In addition to controlling fiber diameter, uniform bead-free nanofiber formation is also important. The controlling of the nanofiber diameter, uniformity and structure is not easy and these can be changed depending on several factors, such as solution parameters, electrospinning conditions, or environmental factors. Due to all these factors, it is extremely rare to produce polymer nanofibers with diameters less than 100 nm^[11,12,16]. In order to get small fiber diameter, carbon nanotubes may be the solution.

Nanofiber nonwovens produced via electrospinning have gained significant attention in a broad range of applications due to their small fiber diameter, high specific surface area, high porosity and pore sizes^[17]. However, since they exhibit low mechanical properties due to their highly porous structure, intrinsically low or, random fiber orientation, and low polymer orientation within individual nanofibers, they cannot be used in broad range of applications without a support fabric composed of microscopic fabrics^[12,13]. In order to avoid the use of a base fabric, several different methods were reported to improve mechanical properties include: changing the nonwoven nanofiber mat into self-bundled yarns^[18,19], applying surface modification or post treatments such as stretching, twisting, or annealing^[20–22], and reinforcing the single nanofiber strength by adding carbon nanotubes (CNTs)^[19,23], layered silicates^[24] or graphite nanoplatelets^[25] into the polymer spinning solution. Among these methods, addition of CNTs to polymer electrospun fibers has attracted many researchers due to their high mechanical, electrical and multifunctional properties and strong interactions with electrospun fiber matrices resulting in large interfacial area^[26–28]. However, several factors influencing the final properties of CNTs – polymer nonwoven fabric such as CNT dispersion, orientation, alignment, volume (or weight) content, and interfacial adhesion with polymer. All these factors either change the highly porous nature of CNTs – polymer nonwoven fabric or complicate the electrospinning process^[27,29,30].

This dissertation describes efforts to: 1) study how aligned sheets of CNTs behave in hybrid filtration applications and 2) create and characterize novel CNT – polymer hybrid nonwoven fabrics to evaluate their aerosol filtration, barrier properties, and energy storage properties. Chapter 4 studies the filtration characteristics of the novel CNT – nonwoven

hybrid fabrics in terms of collection efficiency and pressure drop. The aligned CNT sheets were integrated between polypropylene melt blown nonwoven fabrics onto rotating mandrel. Effect of number of CNT sheet layers and CNT sheet structure inside of the hybrid fabrics on aerosol filtration property was investigated. The filtration characteristics of CNT-nonwoven hybrid fabrics were also compared with other nano-sized filter structures. Based on the results of Chapter 4, Chapter 5 presents a new approach to design filter structure. In previous chapter, it was hypothesized that the radial force from the winding process may compact the sheet structure forming more bundles of CNTs, as opposed to individualized CNTs. Therefore, effect of separate CNT sheet layer and fabric porosity on filtration efficiency and pressure drop were examined. Chapter 6 presents a novel approach to produce nanoscale nonwovens through a hybridization of high aspect ratio CNTs and electrospun fabrics. It is the first instance such a hybrid fabric, which can be easily tailored to contain 0-100% millimeter long CNT. Unlike the other methods, which have significantly influence the final nanofiber nonwovens properties, such as CNT dispersion, orientation, alignment, volume (or weight) content, and interfacial adhesion with polymer, this novel process address all these limitations. In order to further examine these novel fabrics, consolidated and heat-calendered hybrid fabrics were investigated. Due to the unique properties of hybrids, the physical, mechanical, aerosol filtration, and barrier fabric properties were examined. The flexibility of this nanofabrication method allows for the use of many different polymer systems which provides the opportunity for engineering a wide range of nanoscale hybrid materials with desired functionalities. Therefore, Chapter 7 reports a new method to develop a silicon - carbon nanotube (CNT) hybrid anode architecture using CNT-polymer hybridization method.

The CVD pyrolytic carbon coating helped maintain Si nanoparticles within CNT sheets and stabilized solid-electrolyte-interface (SEI) formation, so the electrochemical properties of the hybrid samples before and after pyrolytic carbon coating were investigated.

Chaper 2 Literature Review

2.1 Carbon Nanotubes

2.1.1 Carbon Nanotube Properties

It is no doubt that Dr. Sumio Ijima' work^[31] has greatly increased scientific interest in carbon nanotubes since 1991. Due to carbon nanotubes' unique seamless tube structure, CNTs possess unique mechanical, chemical, electrical, and optical properties, so they have opened an entirely new area for research and industry. Due to these unique properties, carbon nanotubes have many potential applications in the areas electronics, chemistry, biomedical, aerospace, automotive and composite industries^[32].

CNTs exhibit high anisotropy of their properties in their axial direction since CNTs have C-C covalent sp^2 bonding and the highly regular symmetric structural morphology. When a single graphene sheet rolled in a cylinder with a diameter on the order of 1 nanometer (nm), it is called single-walled carbon nanotubes (SWNT). Two sheets concentrically rolled are known as double-walled carbon nanotubes (DWNTs), while three or more graphene sheets rolled into concentric cylinders are called multi-walled carbon nanotubes (MWNTs). There is 0.34 nm spacing between the concentric tubes which is characteristic of graphite plane spacing. The graphite layer wrapping, known as the chirality, affects the resulting properties of the CNT. The chirality is represented by integers (n,m) which indicate a vector in two directions within the graphitic layer structure with the specify the chiral vector $Ch = na_1 + ma_2$ where $n \geq m$ ^[33]. The symmetry of the carbon nanotube will differ depends on the values n and m. Three distinct types of nanotubes can be generated by

wrapping the graphene sheet into a cylinder. These are: “armchair” when $n=m$, “zig-zag” when $n > 0, m = 0$, and all others integer combination are called “chiral”. Figure 2.1 provides visual representation of these structures. The chirality affects the electrical properties of CNTs. Armchair nanotubes are metallic whereas zig-zag and chiral nanotubes are semiconducting^[34,35]. The chirality applies to a single wall, so it is easier to determine for SWNTs. However determining the chirality of MWNTs is more complex due to presence of multiple rolled sheets. Most MWNTs are generally a mixture of chiralities and possess both metallic and semiconducting properties.

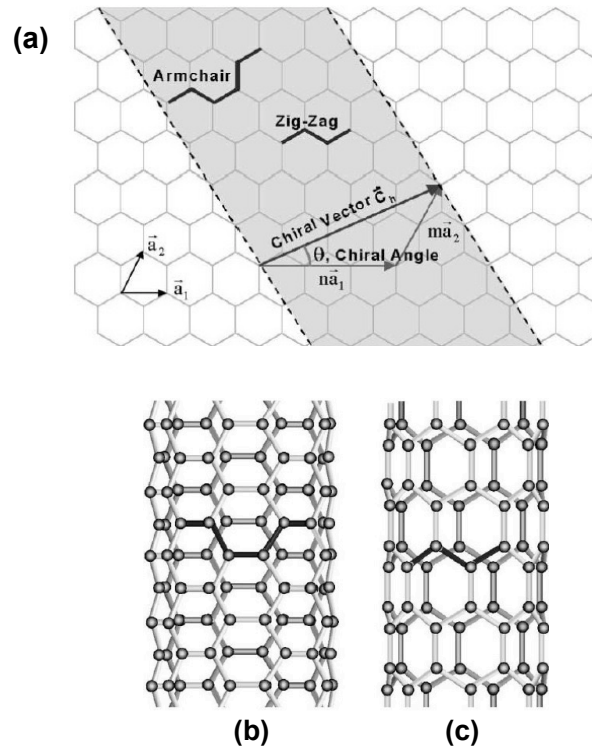


Figure 2.1 a) Schematic diagram of how a graphite sheet is wrapped to form a carbon nanotube, b) illustration of atomic structure of armchair, c) illustration of atomic structure of zig-zag nanotube^[36].

2.1.2 Carbon Nanotube Synthesis

There are many known methods for growing carbon nanotubes, however electric arc discharge^[37], laser ablation^[38], and chemical vapor deposition (CVD)^[39] are the most three common methods. Even though electric arc discharge and laser ablation methods produce consistent nanotubes with few to no defects, they produce only small quantities of product material that requires further purification to produce pure CNT. CVD is able to produce large quantities of CNTs due to its easy control, low cost, and capability to produce vertically aligned CNTs (VACNTs) on substrates. However the consistency is lower and the number of defects is higher compared to other methods. Even though the CNTs quality is lower than other methods, utilizing CVD is a more economically viable option for large scale CNT production.

For CVD growth CNT typically happens at temperature range 500 – 1200 °C. A variety of carbon sources such as, ethylene(C_2H_4)^[39], methane (CH_4)^[40], acetylene (C_2H_2)^[41], and ethanol^[42] etc. have been used as precursors for CVD grown CNTs. Iron, cobalt, and nickel are generally the most effective metal catalyst in CVD of CNTs^[43]. Even though there are several parameters that can vary between CVD processes, the basic steps are the same. A typical CNTs growth in CVD consists of following steps: 1) the catalyst, usually a metal such as iron, cobalt, or nickel, is deposited on a substrate; 2) the chamber in which substrate can be held is heated at certain temperature and then a hydrocarbon gas is flowed; 3) at this elevated temperature, the metal catalyst restructures into nanoparticles and hydrocarbon gases decomposes and then they diffuse and adsorb on a substrate; 4) carbon species

dissolves into the metal till reaching the solubility limit, and then dissolved carbon grows from the catalyst particles in the tubular structure form.^[44] Yoshida and coworkers^[45] made in-situ transition electron microscopy (TEM) observations of the nucleation of the CNT from the carbon saturated iron catalyst particle which is ground breaking view of the process. These TEM images are shown in.

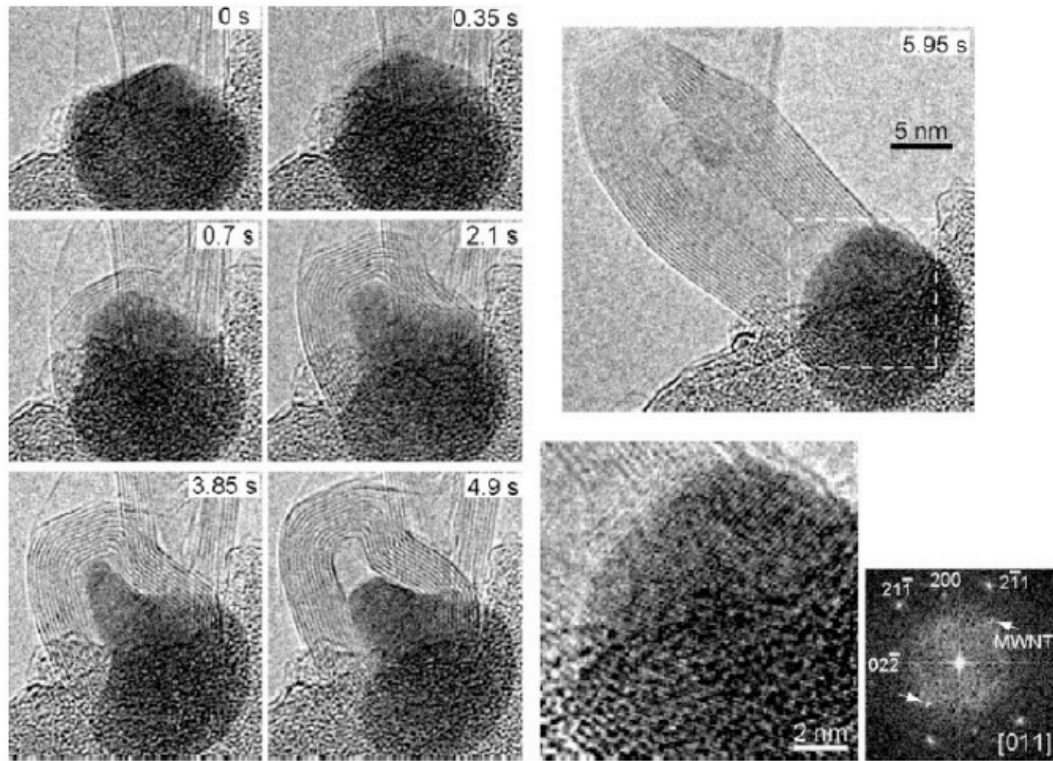


Figure 2.2 TEM images showing carbon nanotube nucleation from iron carbide nanoparticle^[45].

The purposes of using metal catalysts are decreasing the hydrocarbon decomposition temperature and also help arrangement of decomposed radical particles in order to form tubular structure. Iron, nickel and cobalt are the most effective metals due to their catalytic

activity in decomposing carbon compounds, their formation of metastable carbides, and the ability of carbon to quickly diffuse them. The order of catalytic activity of these three metals is $\text{Ni} > \text{Co} > \text{Fe}$. Ni is usually used for catalyzing methane which is more stable than ethylene and acetylene while Fe is often used for decomposing ethylene and acetylene^[46].

The molecular structure of the precursors also affects the CNT structure. Different carbon precursors require different temperature to break down C-H and C-C bonds in order to release free carbon radicals. It directly affects the operation temperature of CVD growth of CNTs. It is a general rule that triple C-C bonds are easier to break than double C-C bonds and single C-C bonds, so CH_4 decomposes at very high temperatures ($> 900\text{ }^\circ\text{C}$) while C_2H_2 decomposes at lower temperature (400-700 $^\circ\text{C}$). In addition, the precursors consisting of cyclic hydrocarbons produce CNT with many bends along their tube axes while linear hydrocarbons such as ethylene and acetylene produce straight CNTs, because they decompose into linear carbon dimers and trimmers at growth temperature^[47].

2.1.3 Vertically Aligned Spinnable Carbon Nanotubes

Growth of vertically aligned spinnable CNT arrays has attracted the attention of many scientists over the past decade. The first spinnable array was reported by Jiang et al. in 2002^[48]. Vertically aligned spinnable CNTs can be grown by CVD, however, there are many variables such as temperature, catalyst, hydrocarbon source, carrier and reactant gas flow rates and ratio, growth time and substrate which directly affects the resulting spinnability of a grown array^[49]. Due to several variables, few research groups can achieve spinnability so far. The mechanism for drawing from CNT array is still controversial. Zhang et al. proposed that

the formation of CNT bundles at the top and bottom of nanotube arrays during the drawing process is the route for continuous drawing^[50].

The catalyst particle size and its size distribution on the substrate is the critical issue for fabrication of spinnable CNT arrays. If nanotubes are uniformly nucleated from densely distributed catalyst particle, aligned, straight and spinnable arrays can be produced. In order to pull CNTs from array, they must have very clean surface which allows for strong Van der Waals interaction with surrounding CNTs^[50]. The strong Van der Waals forces allow the CNTs to support one another and assemble into an aligned structure^[51]. A schematic picture of spinning process can be seen in Figure 2.3.

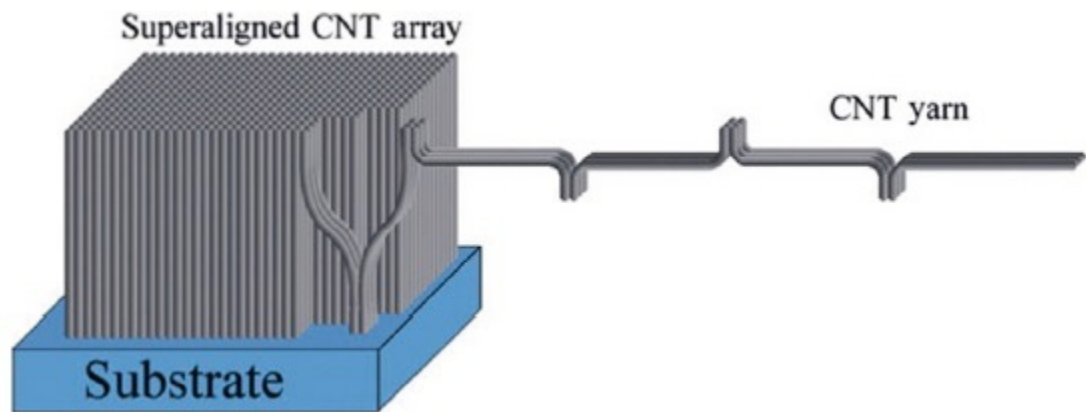


Figure 2.3 Schematic picture of the mechanism for drawing CNT from vertically aligned arrays^[50].

The CNTs can be drawn off in continuous sheets which exhibit preferential alignment and form a network structure for materials which make them great candidate in several applications. Although theoretically the drawn CNT sheets should be highly aligned, the scanning electron microscopy (SEM) images show that they are not, as seen in Figure 2.4.

The misalignment of CNTs within the sheet can function as a defect for lowering mechanical properties. It has also been shown that longer CNTs produce more bundles within drawn sheets compare to shorter CNTs. Even though the presence of bundles improves the electrical properties of CNT sheets, the mechanical and optical properties are adversely affected^[52-54].

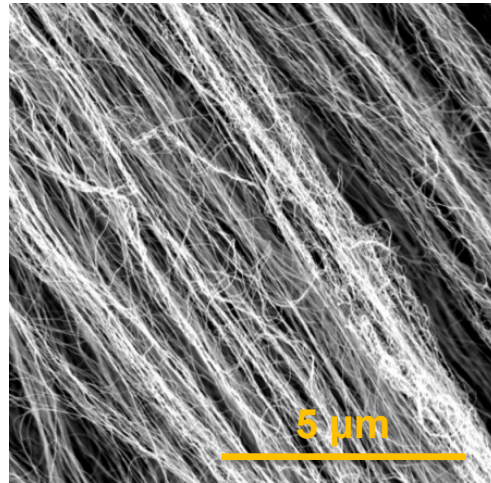


Figure 2.4 The SEM image showing misalignment of drawn CNT sheet

Vertically aligned spinnable CNTs provide an interesting new avenue for potential applications due to their unique structure and properties. The drawn CNT sheet exhibit preferential alignment of CNTs in one direction and they are also extremely thin and porous. They consist of nano-sized, millimeter long CNTs which are impossible to produce with conventional processing methods.

The unique properties of CNT sheets have led to their study in many applications. Their preferential alignment, high surface area, high porosity, and electrical conductivity, have made them useful in lithium-ion batteries and supercapacitors^[55,56]. Since the interconnected network structure of CNTs form conducting paths, no additional metal charge

collectors like aluminum or copper foils are required. In addition, the porous structure of CNT sheets allows them enough free space for volume expansion of active materials during electrochemical cycling. In addition CNT sheets have been used in, actuators^[57], light-emitting diodes^[58], thermal acoustic loudspeakers^[59], reinforcement in high performance polymer matrix composites^[60], and solar energy harvesting devices^[61,62]. Even though aligned CNT sheets have been used in many different applications, they have not been used in textile applications such as aerosol filtration thus far. The unique morphology of the CNT sheets makes them a great candidate for aerosol filtration. The filtration efficiency and pressure drop properties of aligned CNT sheets will be explained in the third chapter of this dissertation.

Due to their excellent mechanical properties, CNTs have been regarded as ideal reinforcement candidate for nano-sized polymer fiber fabrics. Nonwoven fabrics produced from electrospinning cannot normally be used independently due to their low mechanical properties. In order to improve mechanical properties, CNTs have been dispersed in the electrospinning solution to reinforce the resulting nanofibers. However several factors such as poor dispersion, poor alignment, contamination etc. degrade the final product properties. On the other hand, long CNTs like the ones from CNT arrays are ideal structure for electrospun fabrics, however long CNTs are extremely hard to disperse. In order to improve the mechanical properties of electrospun fabrics, a novel method to produce CNT – polymer hybrid fabrics will be introduced in Chapter 4. This extremely high surface area, high porous, low packing density, small diameter CNT – electrospun fabrics maybe great candidate for HEPA and ULPA filtration with low pressure drop.

2.2 Aerosol Filtration

2.2.1 The Importance of Aerosol Filters

The rapidly growing urbanization and industrialization, the quality of the environment has seriously deteriorated in both developing and developed countries since past several decades. Particularly, fine particles are one of the most serious sources of air pollution which turned out to be a major cause of adverse effects on different fields, such as medical, electronics, pharmaceutical, and biological industry^[3,4]. These fine particles especially cause both acute and chronic effects on human health, ranging from minor upper respiratory irritation to chronic respiratory and lung cancer^[5].

These fine particles are separated in two major groups depends on their size: 1- Coarse particulate matter (PM_{10-2.5}) which refers to particle size between 2.5 to 10 μm , 2- Fine particulate matter (PM_{2.5}) which refers to particle size between 0.1 to 2.5 μm ^[63]. The emissions of fine particles are mainly from anthropogenic sources such as, industrial activities, intensive road transport, biomass burning, and others at a global scale. Even though these particles categorized in two size groups, they can be classified by shape and chemical composition, such as normal, medium, and high temperature particles depend on the particle producing conditions^[8].

These fine particles can remain in air for a long period of time. For instance PM₁₀ can be suspended in air from hours to days and travel hundreds of kilometers by wind while PM_{2.5} can remain in air for weeks and travel thousands of kilometers^[63]. In order to prevent

There are four different mechanisms by which an aerosol particle can deposit on an electrically neutral fiber in aerosol filtration. These are inertial impaction, interception, Brownian diffusion, and gravity settling, as seen in Figure 2.6. The effectiveness of the particle capturing for each of these mechanisms depends on particle size, face velocity and fiber diameter. Inertial impaction can be defined as when the inertia of a particle makes it unable to follow the flow of air around a fiber and the particle crosses those streamlines, and impacts the fiber. This mechanism is more effective for collection of larger particles and higher gas velocities. Interception can be defined as when the distance from the center of the particle to fiber surface is equal or less than radius of the particle. In this condition once the particle makes contact with the fiber, the particle sticks to fiber and is removed from the streamline. Brownian motion occurs when the particle size is extremely small compared to the fiber size. Collection the particles via interception mechanism increase with increasing particle size. During diffusion, particle cannot follow its original streamline and move in a random zigzag pattern which causes it to be contact with fibers inside the filter. In gravitational settling, particles are captured by their gravitational force, but this mechanism is negligible for capturing nanoparticles. The effectiveness of particle capture for each of these mechanisms depends on particle size, face velocity and fiber diameter^[67].

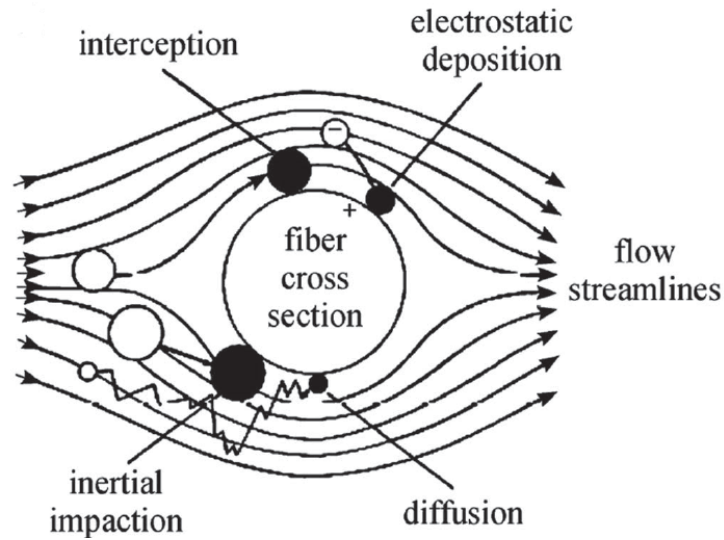


Figure 2.6 Particle depositions on the filter Structure^[67]

A typical collection efficiency as a function of particle size accounting for different collection mechanism is shown in Figure 2.7. As seen in this figure, each mechanism has different effectiveness for different particles sizes. Inertial impaction is more dominant for particles larger than 0.3-1 μm , while diffusion is usually the dominant mechanism for small particles, especially for particles smaller than 0.1 μm . Interception becomes more dominant for the size of particles between 0.1-1 μm . Different mechanisms dominate for different particle size ranges and for one particle size, none of these mechanisms are dominant and shows the lowest filtration efficiency which is called most penetration particle size (MPPS), which is typically around 0.3 μm or smaller for neutral filters^[68].

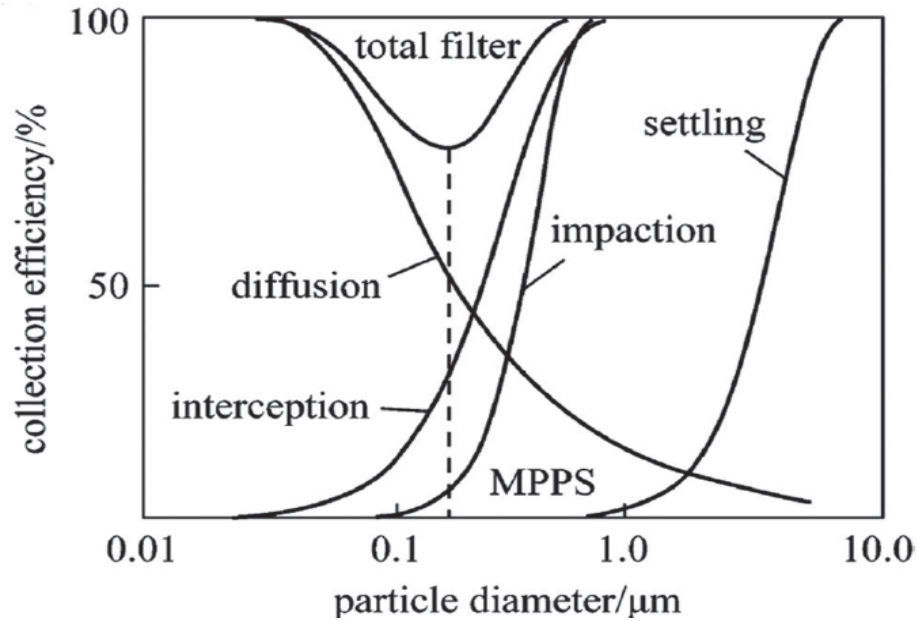


Figure 2.7 Filter efficiency for individual single fiber mechanisms and total efficiency^[68].

The combination of these three mechanism's efficiencies for particle sizes cause V shape curve. This V-shape efficiency curve shifts right or left based upon the gas velocity, fiber diameter or filter type. In literature, when the fiber diameter decreases, the V-shape efficiency curve moves to left side (towards smaller particle sizes) and the size of the V-shape decreases^[69].

2.2.3 Evaluation of Filtration Performance

Fibrous filters are evaluated based on their collection efficiency E and pressure drop ΔP . The expectation from the filter samples based on their collection efficiency changes according to application area or end-use. Some filters are designed to provide high collection efficiency such as HEPA or ultra-low particulate air (ULPA) filters while others are not. The best filter is the one that provides the lowest pressure drop for desired collection efficiency.

Collection efficiency can be defined as the ratio of the particles trapped by a filter over the total number of the particles found in the air upstream of the filter.

$$E = \frac{C_{up} - C_{down}}{C_{up}} \quad \text{Equation 1}$$

where C_{up} and C_{down} are the number concentration of particles at filter upstream and downstream, respectively. Penetration is another term in filtration which is defined as the ability of filter to capture particles.

$$P = 1 - E \quad \text{Equation 2}$$

Collection efficiency and pressure drop are two terms to evaluate filter sample. However, in order to compare filters between each other, quality factor (QF) has been used which is defined as the ratio of collection efficiency to pressure drop.

$$QF = \frac{-\ln P}{\Delta P} \quad \text{Equation 3}$$

There are two standard test methods currently used to evaluate the filters performance in the United States which are ASHRAE (American Society of Heating, Refrigerating, and Air-Conditioning Engineers) Standard 52.1-1992 and ASHRAE Standard 52.2-1999. ASHRAE Standard 52.1-1992 measures a filter's ability to remove larger particles and to capture a mass fraction of coarse test dust, and dust holding capacity. This standard method is suitable for low and medium filtration efficiency filters. ASHRAE Standard 52.2-1999 is a more descriptive test method for filtration efficiency in wide range of particle size^[70].

The 1999 standards evaluate filters based on their particle-size and efficiency results and give them a number from 1 to 20 which is called a minimum efficiency reporting value

(MERV). The higher value of MERV shows the more efficient air filters and the lower value of MERV shows the less efficient air filters. MERV value can be categorized in 5 different groups: 1) the MERV value is 1-4 which is low efficiency filters are used to challenge particle with $d_p > 10 \mu\text{m}$; 2) the MERV value is 5-8 are used to challenge particle with d_p ranging from 3 to $10 \mu\text{m}$; 3) the MERV value is 9-12 are used to remove particle with d_p ranging from 1 to $3 \mu\text{m}$; 4) the MERV value is 12-16 are used to challenge particle with d_p ranging from 0.5 to $1 \mu\text{m}$; 5) the MERV value is 16-20 which is high efficiency filters are used to challenge particle with $d_p < 0.3 \mu\text{m}$ ^[70].

2.2.3.1 Nonwoven Filters

Nonwoven fabrics are broadly defined as sheet, web, or mat structures that are made of natural or man-made fibers, bonded together by entangling fiber or filaments mechanically, thermally, or chemically^[71]. Nonwovens are primarily chosen for filtration applications including disposable respirators, industrial gas cleaning equipment, clean room air purification system, automotive cabin air filter, and indoor air purifiers. They are made of micron diameter fibers which provide physical, particle size-based separation. Nonwoven filters are made of different fibers such as cotton, fiberglass, polyester, polypropylene, polyethylene, ceramic and many other materials^[72]. The solid volume fraction or packing density of nonwovens (α) which is the ratio of volume of all fibers to the total volume of the filter and ranges from 1 to 30 %^[73].

Nonwovens can be made by the meltblowing (MB) and spun-bonding (SB) method, which are typical examples of fibrous media made of from long fibers. Their common

characteristic is that they are made of continuous polymeric filament. These conventional methods are the most well-known techniques to produce nonwoven mats with micro size fiber diameter^[71]. However, conventional fibrous media have suffered from many structural and performance disadvantages, such as large fiber diameter, non-uniform fiber diameter and pore size, relatively low filtration efficiency, and high basis weight^[74]. For instance, the spun-bonding process is limited to producing fiber diameters down to 10–15 μm . In the melt blowing process, thermoplastic polymer melt is rapidly drawn from the spinnerets using high speed air jets and rapidly cooled to form small fibers. The melt blowing process has produced fibers down to approximately 500 nm; fiber diameters generally range from 0.5 to 5 μm ^[75,76]. Limitations of these fabrics for filter, based on the given fibers diameter ranges, are covered in the following sections.

2.2.3.2 Electrospun Filters

It is well known that when fiber diameter decreases, filtration performance is enhanced because of the higher surface area and smaller pore size. Therefore, there are several techniques have been used to produce nanofibrous membrane such as template synthesis, drawing, self-assembly, electrospinning, solvothermal synthesis, phase separation, etc.^[77–79]. Among these techniques, electrospinning is the only process that can routinely and commercially produces fibers down to 100 nm or less. The throughput of the electrospinning process is several orders of magnitude lower than meltblowing and spunbonding processes and produce uniform nanofibers in a continuous process at a long length scale.

Electrospinning is a process of electrostatic fiber formation using electrical charge to produce micro or nano-fibers from a polymer solution. In this method, high electric field is generated between a polymer fluid contained in a glass syringe and a metallic collector. After a high electric voltage is applied, the hemispherical shape of droplet at the end of syringe tip is changed into a conical shape, which is also known Taylor cone. When the applied electric voltage reaches a critical value, the electric force overcomes the surface tension of the droplet, and jet is produced. When a jet travels through the air, the solvent evaporates and then polymeric fibers are formed^[16,80,81]. These fibers are collected on a grounded collector in a web-like pattern. In this method, synthetic polymer fibers such as nylon^[80,82], polyurethane^[83], poly (methylmethacrylate)^[84], polycarbonate^[83], polyethylene oxide^[12] and etc. can be used for electrospinning. The schematic of electrospinning process is shown in Figure 2.8.

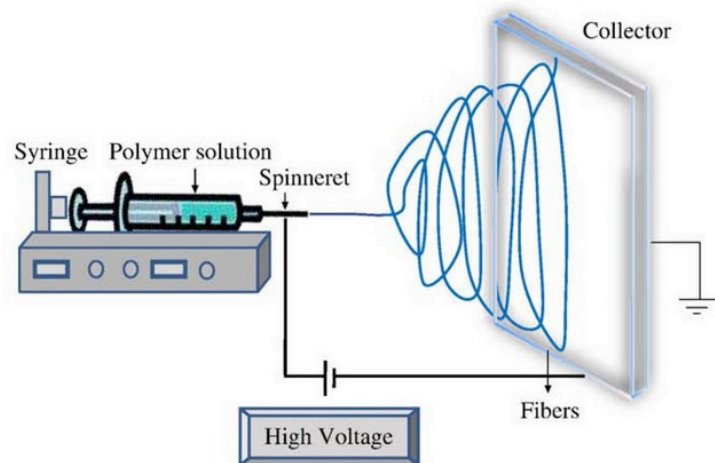


Figure 2.8 Schematic of the electrospinning process^[85].

Electrospun fibrous membranes have several fascinating features that make their nonwoven webs very attractive for aerosol filtration due to their remarkable surface area, high open porosity, and interconnected porous structure^[86]. On the other hand, their highly porous structure, weak bonding between the nanofibers, the intrinsic fiber modulus, small fiber diameter, and the low degree of orientation^[18,87], makes the fibers and fabrics very weak, so it is necessary to use a supporting fabric as shown in Figure 2.9. This supporting fabric provides the essential mechanical properties to maintain structural integrity of the filter while the electrospun nanofiber web enhances the aerosol filtration performance.

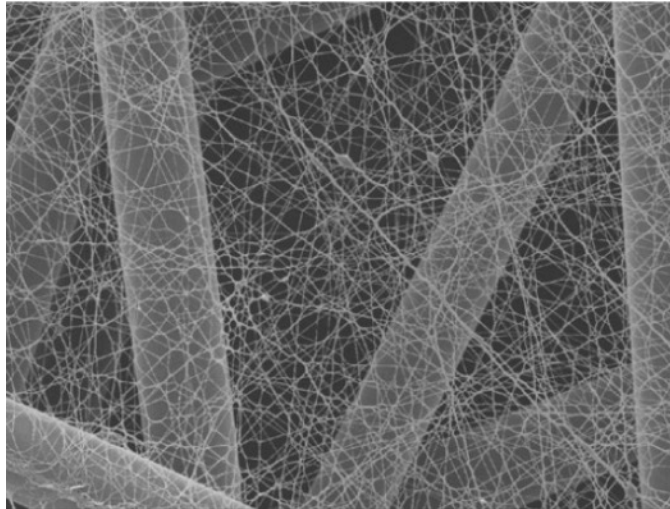


Figure 2.9 A layer of electrospun nanofiber mat (top) on a supporting material (bottom)^[13].

Electrospinning is the predominant commercial method to produce polymer fibers diameters down to 100 nm. Polymer fibers produced from the electrospinning process have relatively uniform diameters, but homogeneity of packing density is the biggest concern^[12,88]. Even though electrospinning is one of the most promising technologies for lightweight, low

basis weight high efficiency particulate air (HEPA) filters, minimizing the high pressure drop they produce is the biggest challenge to their application in filtration^[11]. The main reason for the high pressure drop of electrospun nonwovens is the small pore sizes, high packing density and random fiber orientation. The pressure drop reduction depends on the flow regime in the filter at normal pressure, dilution (reduction the gas pressure), packing density, and fiber orientation^[67]. In order to decrease the pressure drop while keeping the high filtration efficiency, the structure should: (1) have fiber diameters less than 100 nm in order to enhance slip-flow affect. When the flow regime will be changed from slip flow to transition or free molecular flow regime, the slip factor will be increased and the pressure drop will be decreased at normal pressure; (2) have a low packing density, because high packing density causes high pressure drop; (3) the pore structure (pore size and distribution; geometry and interconnectivity of pores) in filter structure should be uniform. However electrospun fabrics cannot currently provide all of these structural features. Therefore, in order to get high filtration efficiency at low pressure drop, small diameter and high surface area CNT-based filters may be the solution.

2.2.3.3 Carbon Nanotube Filters

Due to their very small diameters and high specific surface area, carbon nanotubes (CNTs) have received extensive attention in aerosol filtration area. The diameter of the single-walled and few-walled CNTs is around or less than 10 nm while multi-walled CNTs can be several tens of nanometers in diameter. Even the largest CNTs are smaller than electrospun nanofibers and thus CNTs have been incorporated with conventional polymeric fibers with

the intent of improving filtration efficiency. Depositing CNTs onto nonwoven fabric surfaces increases the fiber surface area and creates a tortuous path for nanoparticles, thus increasing the probability of particle capture ^[14,89,90]. However, the biggest challenges of using CNTs are the dispersion of CNTs and controlling of the thickness and solid volume fraction (SVF) of the filter. A few different methods for incorporating CNTs with polymeric fibers have been reported. The first pioneer work was presented by Viswanathan et al ^[90]. They coated CNTs films onto cellulose filters by a sonication filtration procedure. A thin, continuous layer of MWNTs was formed onto top of the cellulose filter. The SEM images of the coated MWNTs onto cellulose filter are shown in Figure 2.10.a. The diameters of the MWNTs were in the range of 20-50 nm and the thickness of the MWNTs layer was 1-2 μm which is less than 1/100 of the cellulose layer thickness. The MWNTs coating onto cellulose filter increased the filtration efficiency to 99.997%, but the pressure drop also increased dramatically to 29.9 kPa which is 77 times higher than the commercially available HEPA filter which showed 99.97% filtration efficiency and 390 Pa pressure drop at 5 cm/s face velocity^[80]. Even though the diameter size decreased to 20-50 nm, the pressure drop increased dramatically due to the large amount of nanotubes used to get to self-supported films which increased the solidity and thickness. In another method, CNTs were directly grown on the surface of glass fibers^[14], nickel fibers^[89], or metal fibers^[91,92] in order to reduce pore size. The SEM picture of CNTs growth on the glass fiber is shown in Figure 2.10.b. The CNTs coated filters increased the filtration efficiency, especially for small particles (10-80 nm in diameter), but they could not reached HEPA filter properties, as seen in Table 2.1. The drag force on the CNTs coated glass fibers is decreased, so the small

particles could easily diffuse. However the pore structures between the glass fibers did not change, so the CNTs coated glass filter could not reach HEPA filter properties.

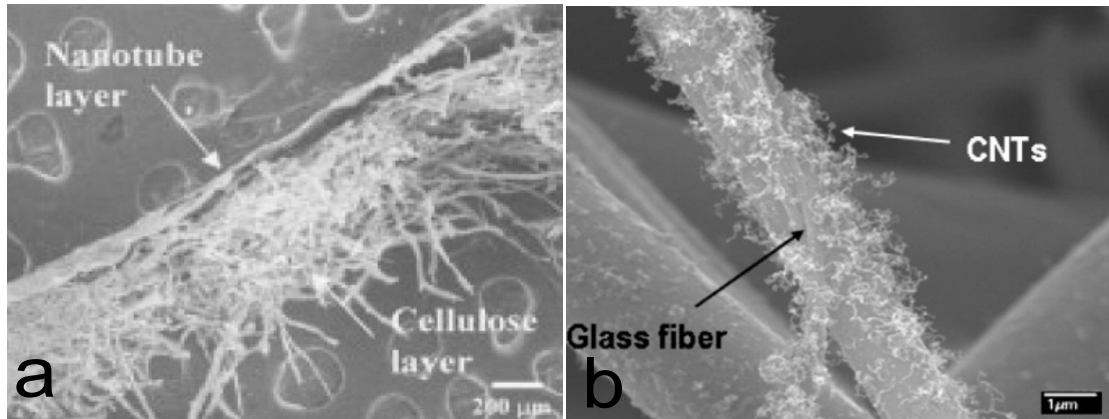


Figure 2.10 a) The cross section view of CNTs coated film onto cellulose layer^[90] b) SEM image of CNTs grown on glass fiber^[14].

Similarly Wei et al.^[93] has grown CNTs onto quartz fiber filter by floating CVD method. The specific area of the CNT/quartz filter increased more than 12 times higher than the pristine quartz filter. Therefore, the filtration efficiency increased to 99.97% but the pressure drop increased to 840 Pa which is two times the pressure drop typical for commercially available HEPA filters. The small CNTs decreased the pore sizes which increased to pressure drop. Park et al.^[91] synthesized CNTs directly on the surface of micrometer-sized metallic fibers. The filtration efficiency increased to 98% and the pressure drop was 245 Pa at 0.3 μm particle size at a 3 cm/s flow rate which is the same pressure drop with the HEPA filter. All the studies improved the filtration efficiency, but their pressure drops increased dramatically too, so the low quality factor was observed as seen in Table 2.1.

Nasibulin et al.^[94–96] developed an aerosol CVD synthesis method to prepare a free-standing CNT film by vacuum filtration method. They prepared free standing SWNT films first collecting nanotubes downstream of the reactor on microporous filters, and then they were transferred to a substrate. The produced SWNTs were 10 μm in length and 1.3-2 nm in diameter. The thickness of the free standing SWNT films can be varied from couple hundreds to a few micrometers depending on the collection time. The 70 nm thick free standing SWNT films showed high filtration efficiency but they showed also high pressure drop at low flow rate.

Wei et al.^[97] developed gradient nano-structure filters (GNF) in order to increase the filtration efficiency at the MPPS. The catalyst aerosols were generated for growth of the CNTs in HEPA quartz filter by atomizing a mixed aqueous solution as seen in Figure 2.11. The results showed that the filtration efficiency increased at the MPPS to 99.997%, because small aerosol particles could easily diffuse on CNTs into the HEPA quartz filter. They coated small amount of CNTs onto the HEPA quartz filter fibers, so the pressure drop did not increase too much.

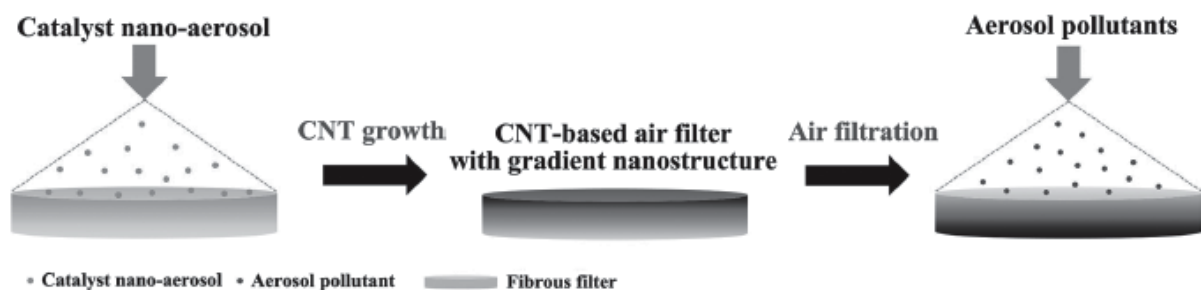


Figure 2.11 Schematic of the catalyst loading on a quartz fiber filter and growth of the CNTs [97].

The summary of the various CNT-based aerosol filters that have been reported lastly is shown in Table 2.1. Even though filtration efficiency is improved by using CNTs in various filter structures, the high pressure drop reduces the overall performance of the filters. Even with their very small fiber diameters, processing the CNTs to produce the required fiber separation and packing densities is incredibly hard, and people have had limited success. Therefore, the biggest challenges of fabricating CNT-based filters are dispersion of CNTs, control of the thickness, and the high packing density.

Depositing CNTs onto nonwoven fabric surfaces increases the fiber surface area and creates a tortuous path for nanoparticles. This increases the probability of particle capture through the interception, diffusion, and impaction mechanisms. However, longer CNT deposition creates CNT web structure, which agglomerates and bundles CNTs together and thus reduces their surface area and increases the packing density. The small CNT diameter enhances the filtration efficiency. On the other hand, high packing density, small pore sizes, and inhomogeneous pore size distribution are other important parameters that increase the pressure drop. Therefore the ideal CNT filter should have a very low packing density, the smallest fiber diameter possible, very low thickness, and high porosity. In order to achieve high filtration efficiency and the lowest pressure drop possible, our goal is to produce filters that meet those requirements using CNT sheets.

Table 2.1 The filtration performance of air filters based on CNTs.

Structure	Test flow velocity [cm/s]	Test Particles [nm]	Pressure drop [kPa]	Filtration Efficiency [%]	Quality Factor [kPa-1]	Ref.
MWNT-coated filter	11.5	300	2.99	99.9976	3.56	[90]
Free standing SWNT film	1.97	44	0.071	99.997	147	[94]
CNT/metallic fiber filter	3	130	0.115	93.8	24.18	[91]
3D CNT Scaffold	2.99	300	25	99	0.18	[98]
CNT-coated glass fiber filter	20	100	0.08	33.3	5.06	[99]
CNT/sintered nickel microfibrous matrix	20	300	0.7	79-80	2.4	[89]
CNT/quartz fiber filter	6.21	300	0.84	99.974	9.89	[93]
CNT/quartz fiber filter with gradient nano-structure	5.31	63.8	0.435	99.9959	23.21	[97]
Agglomerated CNT fluidized bed air filter	1.57	300	0.167	99.988	54.06	[100]

2.2.4 Existing Filtration Theories

In order to predict the filtration efficiency and the pressure drop on the structure of the filter sample, several different theories were proposed based on the flow pattern of air inside of the web. When the flow pattern inside of the web is known, the behavior of the injected aerosol particles can be derived and it helps for better understanding the filtration process^[101].

Depending on the air velocity and the scale of the system, inertia or viscosity of air dominates when air flows past on fibers. The ratio of the importance of inertial effects in the flow to viscous effects in the flow can be determined by the Reynolds number, Re :

$$Re = \frac{\rho VL}{\mu} \quad \text{Equation 4}$$

where ρ is the air density which is approximately 1.20 kg/m^3 , μ is coefficient of viscosity which equals $1.81 \times 10^{-5} \text{ kg/m.s}$ at NTP (Normal Temperature and Pressure – air at 20°C and 1 atm), V is the air velocity. L is the pore diameter.

The flow regimes is identified depends on the Reynolds number. A high Re implies a turbulent flow, and the moderate Re number indicates a laminar flow, while very small Re number implies viscous creeping motion. For nano-sized fiber media filtration, Re is always less than 1, so inertial influence is neglected, and Reynolds number is assumed to be zero. The most important property for the inviscid flow is that the flow pattern does not change depends on the face velocity^[101].

In aerosol filtration, the flow regimes of the gas molecules around the fibers are also important. The Knudsen number, Kn, is a dimensionless number used to define the flow regime of the gas around the fibers. The flow regimes can be classified into the four different types based on Knudsen number: continuum flow regime, slip flow regime, transition flow regime and, free molecular flow regime^[67,101]. During the past decades, there have been many pioneering studies that have presented a filtration theory that represents the best filtration efficiency between theoretical calculated and experimental results^[101–104]. However, since the filtration theories validated by test data only cover continuum flow and aerodynamic slip flow regime, there is an only limited comparison between theoretical and experimental results for fibrous filters which operate in the transition and free molecular flow regime. The most common filtration theories will be briefly summarized in this study.

2.2.4.1 Single Fiber Theory

Since a single fiber is the smallest element in fibrous filter, knowledge about how particles deposits on single-fibers is fundamental importance to deeply understand how the filtration process works^[102].

Filtration Efficiency (E) is defined as:

For single fiber theory, the filtration efficiency of the filter can be obtained by single fiber efficiency, η_f , by the following equation^[68]:

$$E = 1 - \exp \left[-\frac{4\alpha n_f t}{\pi(1-\alpha)d_f} \right] \quad \text{Equation 5}$$

where α is fiber packing density, n_f is single fiber efficiency, t is filter thickness, and the mean fiber diameter is d_f . As we mentioned in section 2.2.2, interception, inertial impaction, and Brownian diffusion are the three mechanisms for catching small particles. Therefore, the single fiber efficiency should be calculated for each mechanism independently and it is less than 1.0^[68].

$$E = 1 - (1 - \eta_R)(1 - \eta_D)(1 - \eta_I) \quad \text{Equation 6}$$

where η_R , η_D , and η_I are the single fiber efficiency due to the interception, diffusion and inertial impaction, respectively.

2.2.4.2 Cell Model

Kuwabara^[103] and Happel^[104] took into account the neighboring fiber interference in aerosol filtration theory. They both independently calculated the flow field in an ordered matrix by setting different boundary conditions. Since they consider the fiber in a finite space, their filtration theories differ from other isolated theories. Even though they both independently studied the neighboring fiber affect in filtration, the Kuwabara model has proven to be a better representation of the flow around fibrous filter than Happel model^[105-108].

The cell model is based on assumption that all fibers in the filter sample have the same flow field and all fibers are perpendicular to the main flow direction, and also filter consists of parallel fibers, spaced randomly transverse to the flow. Kuwabara^[103] assumed each fiber of radius, R_f , was surrounded by an imaginary cylinder of radius, R_{fc} , as seen in Figure 2.12.

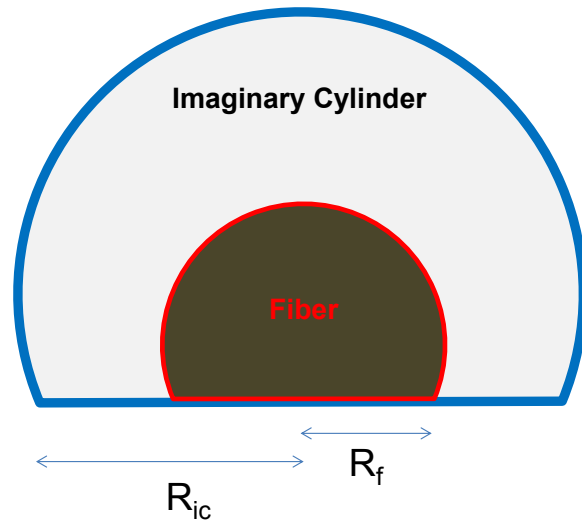


Figure 2.12 Cell Model

Kuwabara assumed that fibers are packed in a hexagonal arrangement and vorticity is zero on the cell bonding lines, and also the positive vorticity on the bottom side of the cell is cancelled by the negative vorticity on the upper side of the cell^[103], as seen in Figure 2.13.

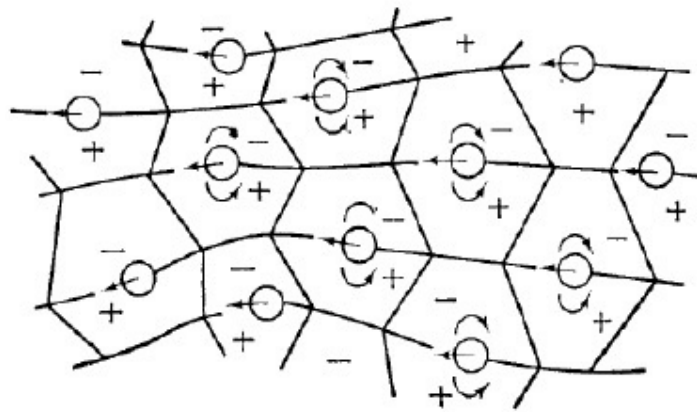


Figure 2.13 Kuwabara flow cell^[103].

Kuwabara calculated the effect of distortion of the flow field around a fiber due to proximity to other fibers which was called Kuwabara hydrodynamic factor (Ku). It depends only on solidity of the fibrous filter, α , when the Reynolds number, $Re < 1.0$.

$$Ku = -\frac{(\ln\alpha)}{2} + \alpha - \frac{\alpha^2}{4} + \frac{3}{4} \quad \text{Equation 7}$$

In order to make precise prediction collection efficiency from the filter sample, several parameters should be calculated: 1) the flow field around the fiber should be known based on the fiber diameter, 2) the particle trajectory based on flow (continuum, slip-flow, transition, and free molecular flow) to be solved for each fiber in the filtration medium, 3) the efficiency for single fiber^[102]. However, even though there is a big range between the fiber diameters, fibers inside the filter are treated the same way for the cell model.

Nonwoven fibrous filters have an irregular structure due to inhomogeneous fiber orientation, and distribution, and variation of fiber diameters. Therefore, these inhomogeneities inside a fibrous filter cause several issues in filtration models^[102]. For instance, some fibers may be at z-direction which is not perpendicular to the flow direction, solidity or packing density of the filter varies with the location, and there may be a wide fiber diameter distribution. Even though several researchers have studied this inhomogeneity factor, unfortunately they have not identified the influence of different inhomogeneity issues. The main reasons for different inhomogeneities in a filter media are: 1) three dimensionality of filter structure; 2) packing density variation; 3) fiber diameter distribution^[109].

Since nonwoven filters have an irregular structure, the cell model cannot correctly account the filtration efficiency of filter sample. Even though many scientists have refined this model, there has not been any theory developed to solve all these parameters.

2.2.5 The Parameters that Affect Filtration Properties

The filtration theories show that the single fiber capture efficiency depends on three dimensionless parameters: 1) Peclet number, 2) Knudsen number, 3) Packing density. In addition, fiber orientation is also another factor that significantly affects the filtration efficiency and the pressure drop. These four parameters explained in detail below.

2.2.5.1 Fiber Orientation

The microstructure of disordered fibrous materials can be classified in three major groups: 1-Unidirectional structures: Axes of all cylindrical fibers are parallel each other, 2-Random layered (planar) structures: Axes of all cylindrical fibers lie randomly in parallel planes and they are often perpendicular to flow direction, 3- Three-dimensionally isotropic structures: Axes of all cylindrical fibers are randomly oriented in any direction in 3-D space^[110], as seen in Figure 2.14.

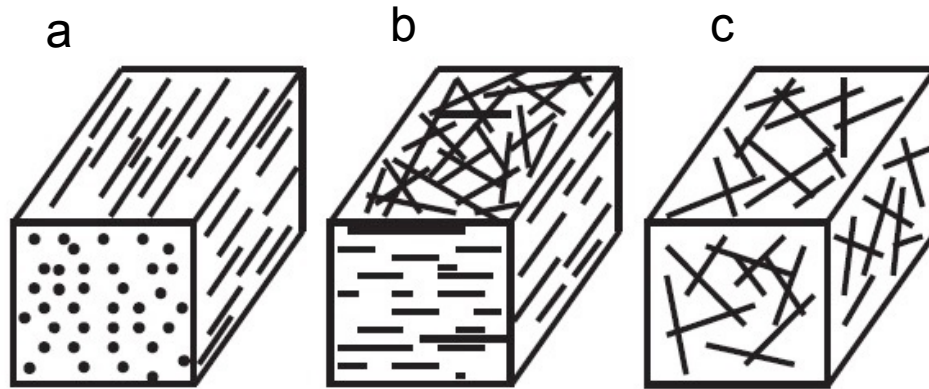


Figure 2.14 A schematic of fiber orientations a) uni-directional random fiber arrangement, b) random layered (planar) fiber arrangement, c) three-dimensionally fiber arrangement^[110].

Fotovati et al^[110]. generated 3-D virtual media using FORTRAN program in order to study the influence of in-plane and through-plane fiber orientation of a fibrous material on filtration efficiency and pressure drop. The fiber orientation in-plane media was varied from 0° to 45° and other parameters keep constant. The results showed that in-plane and through-plane fiber orientation distribution both show little or no influence on filtration efficiency for submicron particle sizes (50 nm to $1\mu\text{m}$). However fibers in-plane and through-plane fiber orientation play significant role for the bigger particle sizes (2-5 μm). When the fiber's directionality increases, the filtration efficiency increases. Therefore 0° angle fiber orientation sample showed the highest filtration efficiency while the 45° angle fiber orientation showed the lowest capturing efficiency. The pressure drop was also compared and the results showed that there is no significant effect associated with the fibers' in-plane orientation. The author in that study used fibrous filters that had a fiber diameter of about 10

μm and 7.5 % solid volume fraction. For the sake of brevity, the author kept the constant the fiber diameter and solid volume fraction of the filter sample.

2.2.5.2 Fiber Diameter

Nano-particles and ultrafine particles can be generated in great quantities from several different processing methods, such as diesel vehicles and the supposedly low-emission liquid petroleum driven vehicles^[111]. In order to the capture of these nano-aerosols, especially nano-particles, using nano-sized filters with large surface area to volume ratio are the most effective method^[112]. Diffusion is the most dominating capturing mechanism for these nano-aerosols especially ultrafine particles less than 100 nm. Eq. (5) shows the single fiber efficiency due to diffusion mechanism. It can be seen that single fiber efficiency depends on three dimensionless parameters: 1- Peclet number (Pe) that represents the relative strength between interception and diffusion mechanism^[88,113], 2- Knudsen number for fiber diameter (Kn_f) that represents the flow regime over nanofibers^[67], and 3- nanofiber packing density or solidity (α)^[12,13]. How these parameters affect filtration efficiency and pressure drop will be explained in details below.

2.2.5.2.1 Knudsen Number

The Knudsen number, Kn , is a dimensionless number used to define the flow regime of the gas around the fibers^[67].

$$Kn = \frac{2\lambda}{d_f} \quad \text{Equation 8}$$

where λ is the mean free path of air molecules (around 66 nm under normal temperature and pressure) and d_f is the diameter of the fiber. Several studies have been worked on to predicting the collection efficiency and the pressure drop these regimes. The flow regimes can be classified into the four different types based on Knudsen number: continuum flow regime, slip flow regime, transition flow regime and, free molecular flow regime. The flow regimes under normal conditions are summarized in Table 2.2 based on fiber diameters.

Table 2.2 Relationship between Knudsen number, fiber diameter, and flow regimes.

Knudsen number (K_n)	The diameter of fiber (d_f)	Flow regimes around fibers
$K_n < 0.001$	$d_f > 132 \mu\text{m}$	Continuum flow
$0.001 < K_n < 0.25$	$528 \text{ nm} < d_f < 132 \mu\text{m}$	Slip flow
$0.25 < K_n < 10$	$13.2 \text{ nm} < d_f < 528 \text{ nm}$	Transition flow
$K_n > 10$	$d_f < 13.2 \text{ nm}$	Free molecular flow

When the fiber diameter of the filter is higher than 132 μm , the Knudsen number is less than 0.001 which the gas can be treated as a continuum fluid. The gas molecular structure can be ignored because the mean free path of the gas molecule is very small compared to the fiber diameter. The interest in using fibers with small diameters for aerosol filtration has increased significantly for several decades. The most commonly used techniques for producing commercially available nonwoven fibers include: melt-blowing and spun-bonding. The spun bonded process is limited to producing fiber diameters down to 10-

15 μm . In the melt blowing process, thermoplastic polymers melt is rapidly drawn from spinnerets using high speed air jets and rapidly cooled down to form small fibers. The melt blowing process has produced fibers down to around 0.5 to 5 μm ^[76,114]. When the fiber diameter of filter sample is between 528 nm to 132 μm , the Knudsen number is around 0.001 $< \text{Kn} < 0.25$ range. The gas fluid can slip over the fiber surface in that Knudsen number range, and the continuum assumption is no longer valid. In order to predict the filtration efficiency and pressure drop, filtration theories were developed by modifying the continuum flow theories to include the slip effect for the slip flow regime. The air filtration theories predict that when the Knudsen number increases, filtration efficiencies increase as well.

The rapid development of fiber fabrication technology, electrospinning, is a process of electrostatic fiber formation using electrical charge to produce micro or nano fibers from polymer solution. Electrospinning is the predominant commercial method to produce polymer fibers down to 100 nm, so electrospun nonwovens have been used in aerosol filtration area. Even though electrospun fibers have been intensively used in aerosol filtration area, the theoretical model has not been made due to the inapplicability of Navier-Stokes equations and complexity of solving the Boltzman equation^[115] in transition flow regime^[103]. The electrospun fibers can decrease the fiber diameter maximum 100 nm, so the Knudsen number cannot be increased more than 1.32. When the fiber diameter is much smaller than the mean free path of gas molecules, the flow field around the fibers is called free molecular flow regime (FMF). It is unfortunately impossible to decrease fiber diameters in conventional fiber making process. Therefore, scientists changed the pressure and the temperature, in order to understand the characteristic of filter sample at higher Knudsen numbers^[69,116]. The results

showed that higher filtration efficiency and lower pressure drop were obtained at high Knudsen number which was acquired at reduced pressure or increased temperature. Zhang et al.^[117] obtained the transition flow conditions in their experimental study by reducing the gas pressure and using ultra fine fibers with mean fiber sizes that varied between 0.25 and 0.83 μm . Their results also proved that the classical theories are not adequate to describe filtration in transition flow regime. On the other hand, by using CNT, especially single walled carbon nanotubes (SWNTs) which have less than 10 nm fiber diameters, the aerosol filter will be in FMF regime under normal conditions. Due to fiber diameters needed to be in the FMF regime, research work on aerosol study in FMF regime is very scarce^[67].

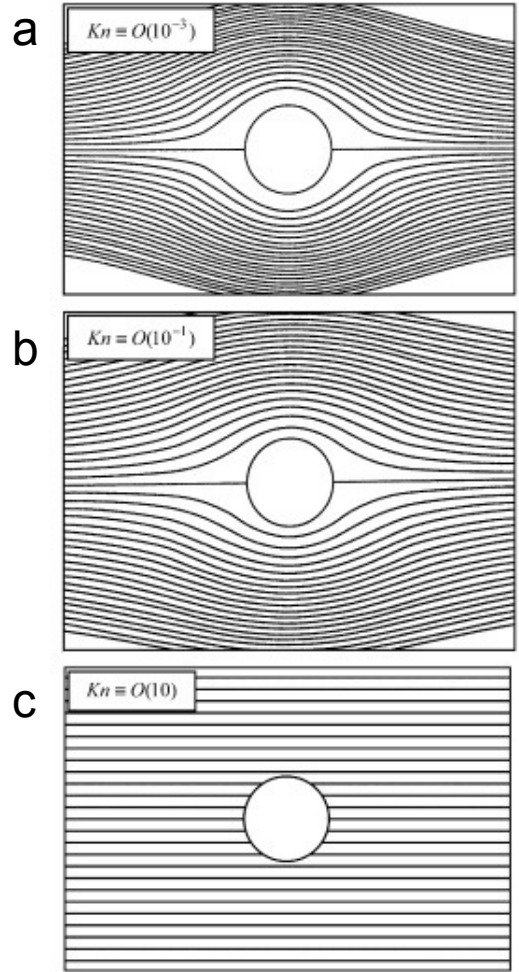


Figure 2.15 The Kuwabara flow field about a fiber based on the flow regimes with $K_n = 10^{-3}$, 10^{-1} , 10, from left to right^[69].

2.2.5.2.2 Peclet Number

Peclet number is a dimensionless number that refers the effectiveness of mass transport by dispersion or diffusion^[88,113]. The equation of Peclet number is:

$$Pe = \frac{u_0 d_f}{D} \tag{Equation 9}$$

where U_0 is the face velocity and D is the diffusion coefficient.

There are two parameters, face velocity and fiber diameter, which directly affect the Peclet number. High Peclet number represents the low diffusion while low Peclet number represents the high diffusion.

Based on this consideration, Hung et al.^[88] investigated the filtration of nano particles (50–500 nm) using nano-fiber filters (Kn_f from 0.62 to 1.44) over an extended Pe range from 0.5 to 21. The mean diameter of electrospun nanofibers was 94, 185, and 220 nm, respectively. Two different face velocities were adopted in order to evaluate how face velocity affected diffusion mechanism. The aim of his study was to investigate the filtration of nanoaerosol using nanofiber filter in the transition flow with large slip wherein Knudsen number is well above unity and low Peclet number.

Several different conclusions were made from the test results. The filtration efficiency results showed that filtration efficiency due to diffusion dramatically increased when the Peclet number decreased to 0.5. When the fiber diameter increased from 94 to 220 nm, the filtration efficiency decreased. The results showed that when Peclet number decreased to single digit, the efficiency due to diffusion increased dramatically. When the face velocity decreased to 1 cm/s, the filtration efficiency also increased due to longer retention time of aerosols in the nanofiber network. It can be concluded from the Hung et al. paper that fiber diameter and face velocity directly affect Peclet number that influence on the filtration efficiency.

2.2.5.3 Packing Density

Packing density, also known solid volume fraction, (α) describes how much filled the fibers in the fabric. Packing density is defined as the follow expression^[12,76,112]:

$$\alpha = \rho_{\text{web}} / \rho_{\text{fiber}} = \frac{W/L}{\rho_{\text{fiber}}} \quad \text{Equation 10}$$

where ρ_{web} (g/cm^3) and ρ_{fiber} (g/cm^3) are the bulk web density and the fiber density, respectively. The homogeneity of the fiber distribution is important for filtration. Since polymer fibers from electrospinning process do not have relatively uniform fiber diameter, the homogeneity of fiber packing is the biggest concern. There are several studies in literature that evaluate how packing density effects the filtration efficiency and the pressure drops. When packing density increases, filtration efficiency and pressure drop both increase, because particles cannot easily pass within the high packed fibers. However, the drag force is also high because high packed fibers do not let air flow pass easily. The increase of the pressure drop outweighs the efficiency for small particles while the increase of the efficiency outweighs the pressure drop for larger particles. Therefore, the quality factor is low for small particles, but the quality factor of filter increases for larger particles.

In order to get high filtration efficiency but low pressure drop, low packing density filters are better^[11]. However, low packing density causes decreasing the filtration efficiency. If fiber diameter decreases, the number of fibers will increases per unit volume, so filtration efficiency will increase without increasing the packing density as long as other parameters keep the same.

2.2.6 Theoretical Calculations

Although many theories have been created, there is a big discrepancy between the theoretical calculations and experimental results due to big range of fiber diameter, fiber distribution, fiber orientation etc.^[118]. The most common used theoretical calculation is shown below^[12,88]:

For nanofiber filters, the interaction diffusion and interception is significant, and inertial impaction is usually neglected.

$$n_f = 1 - (1 - n_D)(1 - n_R)(1 - n_I) \quad \text{Equation 11}$$

where n_D , n_R , and n_I are the single fiber efficiencies due to diffusion, interception, and inertial impaction respectively.

$$n_D = 1.6 \left(\frac{1-\alpha}{Ku} \right)^{\frac{1}{3}} Pe^{-\frac{2}{3}} C_1 C_2 \quad \text{Equation 12}$$

where, Ku is Kuwabara hydrodynamic factor which is defined as:

$$Ku = -\frac{(\ln \alpha)}{2} + \alpha - \frac{\alpha^2}{4} + \frac{3}{4} \quad \text{Equation 13}$$

Pe is Peclet number which is defined as:

$$Pe = \frac{U_0 d_f}{D} \quad \text{Equation 14}$$

where U_0 is the face velocity, D is the diffusion coefficient which is defined as:

$$D = \frac{k_B T C_S}{3\pi\mu D_p} \quad \text{Equation 15}$$

where, k_B is the Boltzmann constant, T is the absolute temperature, μ is the air dynamic viscosity, D_p is the particle diameter and C_S is the Cunningham slip correction factor according to Rader^[119], which is defined as:

$$C_S = 1 + K_n [1.207 + 0.44 \exp\left(-\frac{0.78}{K_n}\right)] \quad \text{Equation 16}$$

where, Kn is the Knudsen number of particle.

$$C_1 = 1 + 0.388 Kn_f [(1 - \alpha) \frac{Pe}{Kn}]^{1/3} \quad \text{Equation 17}$$

where, Kn_f is the Knudsen number of fiber.

$$C_2 = \frac{1}{1 + 1.6 \left[\frac{(1-\alpha)}{Ku}\right]^{1/3} Pe^{-2/3} C_1} \quad \text{Equation 18}$$

$$n_R = 0.6 \left(\frac{(1-\alpha)}{Ku}\right) \left(1 + \frac{Kn_f}{\frac{D_p}{d_f}}\right) \left(\frac{\frac{D_p^2}{d_f^2}}{1 + \frac{D_p}{d_f}}\right) \quad \text{Equation 19}$$

$$n_i = \frac{(Stk)J}{2Ku^2} \quad \text{Equation 20}$$

$$Stk = \frac{\tau V}{d_f} \quad \text{Equation 21}$$

$$\tau = \frac{\rho_p d_p^2 C_c}{18\mu} \quad \text{Equation 22}$$

2.2.7 Pressure Drop

In a fibrous filter, the pressure drop is due to the total drag force on all the fibers. The pressure drop across the filter is the combined effects of the resistance of each fiber while the

air flow passes it. The gas flow based on the value of Knudsen number is important for the pressure drop of aerosol filter^[108].

For the continuum regime, the pressure drop of air filter is a function of its thickness, fiber diameter, solid volume fraction (SVF) or also called packing density, the air viscosity, face velocity and fiber orientation^[68,118].

$$\Delta p = \frac{\eta t U_0 f(\alpha)}{d_f^2} \quad \text{Equation 23}$$

where, η is gas viscosity, U_0 is gas velocity, t is filter thickness, d_f is fiber diameter and α is the SVF of the filter. $f(\alpha)$ changes depends on the theories. All the attempts were made to justify the good correlations with experimental and theoretical models. Davies's experimental correlation is obtained various filter media with SVF ranging from 0.006 to 0.3^[108].

$$f(\alpha) = 64\alpha^{\frac{3}{2}} (1 + 56\alpha^3) \quad (\text{for } 0.006 < \alpha < 0.3) \quad \text{Equation 24}$$

Pich et al.^[120] analyzed the general characteristic of the pressure drop on the gas pressure at different flow regimes (Knudsen number values). He found one of the important relationships between the pressure drop across the filter, ΔP , and the pressure drop across the filter when $\text{Kn} = 0$, ΔP_0 .

For $\text{Kn} < 0.001$ (Continuous Regime)

$$\frac{\Delta P}{\Delta P_0} = 1 \quad \text{Equation 25}$$

For $0.25 < \text{Kn} < 0.001$ (Slip Flow Regime),

$$\frac{\Delta P}{\Delta P_0} = \frac{1 + \frac{0.998Kn_0}{-0.75 - 0.5\ln\alpha}}{1 + \frac{0.998Kn}{-0.75 - 0.5\ln\alpha}} \quad \text{Equation 26}$$

For $Kn > 10$ (Free Molecular Flow Regime),

$$\frac{\Delta P}{\Delta P_0} = \frac{0.57}{Kn} (-0.75 - 0.5\ln\alpha + 0.998Kn_0) \quad \text{Equation 27}$$

He concluded that the pressure drop reduction was depends on the three factors: 1) the character of the flow through a filter at normal pressure (continuum, slip, transitional, and free molecular flow); 2) dilution (reduction of the gas pressure); 3) the packing density (SVF) of the filter.

2.3 CNT Reinforced Nanofiber Fabrics

2.3.1 Mechanical Properties of Nano sized Fibers

When the diameters of polymer fiber materials decrease from micrometers (e.g. 10-100 μm) to submicron or nanometer (e.g. 1 -0.01 μm), there appear several amazing characteristics such as very large surface area to volume ratio, and flexibility in surface functionalities compared to fibers of large diameters^[121]. These outstanding properties make submicron or nanofiber polymer fibers great candidate for many significant applications such as air and water filtration^[80,81], drug delivery^[122], tissue engineering^[26], and regenerative medicine^[123], besides many others involving active materials for photonics and electronics^[121,124]. There are several fabrication and synthesis techniques have been used for production of organic nanostructures and polymer nanofibers such as drawing, template

synthesis, phase separation, self-assembly, electrospinning, etc. in recent years^[20,121]. However, the electrostatic spinning or electrospinning is a unique technology due to its unequalled operational simplicity and effectively up-scaled, opening actual perspectives for industrial production^[20].

Although polymer nanofibers produced from electrospinning have several significant properties, their lack of mechanical integrity relative to conventional cast or nonwovens is one of the biggest disadvantages. Electrospun fabrics typically display lower tensile strength which is relatively weak compare to other processed fibers due to their highly porous structure, weak bonding between nanofibers, and low orientation and chain extension of the polymer chains along the fiber axes^[18,87]. However, many applications require high mechanical property nanofiber nonwovens and for applications like air and water filters and protective clothing aimed at biological and chemical protection^[13]. For those applications, microfibers are still employed as supporting fabrics due to the low mechanical properties of electrospun nanofibers which cannot be used independently^[12,20]. In addition, the general electrospinning has been limited to the fabrication of a variety of anisotropic mechanical properties, which is extremely important for tissue engineering^[125].

2.3.2 Improvement of Mechanical Properties of Nano-fiber Nonwovens

2.3.2.1 Traditional Methods

In order to use nanofibers nonwovens' properties and to avoid the use of a base fabric, Scientists have been trying to improve the mechanical strength of electrospun fiber nonwoven mats or single nanofibers. However, the polymer nanofibers produced by

electrospinning process are not strong as desired because of small fiber diameters, and unoptimized molecular orientation in the electrospun fibers^[19,87,126]. In order to make high performance electrospun nanofibers, first the molecular structures of nanofibers were oriented with chain extension to resemble the ideal polymer chains model in Figure 2.16.



Figure 2.16 Ideal polymer chains model to produce high strength and high modulus fibers^[87].

Even though traditional methods are not feasible for single nanofibers to induce high molecular orientation like post-drawing due to technological difficulties, limited stretching or drawing has been attempted to oriented nanofibers mat in order to generate improved molecular orientation crystallinity. Some people used this method to improve mechanical properties of electrospun nonwoven mats. For instance, Wu et al^[127]. applied sold-state hot-drawing at 135°C to polyacrylonitrile (PAN) nanofiber sheets. They increased the crystallinity of PAN nonwoven sheet from 7.9% to 31.8%, so the tensile strength of PAN nonwoven sheet improved from 100 MPa to 220 MPa. However stretching method is not applicable for most polymer electrospun nonwovens.

2.3.2.2 CNT Reinforced Polymer Nanofibers

In order to improve the mechanical properties of electrospun nonwovens more than applying traditional methods like post-drawing, previous studies have reported several different methods, such as altering the nonwoven nanofiber mat into self-bundled fiber yarns^[19] or reinforcing nanofiber strength by adding carbon nanotubes, layered silicates, or graphite nanoplatelets into polymer solution^[19,23–25,30]. However, many of these approaches to enhance the mechanical properties of electrospun nonwoven mats either change the highly porous nature of nanofiber nonwovens or complicate the electrospinning process^[18]. Among these methods, the addition of CNTs into polymer solution has attracted many researchers due to CNTs - polymer electrospun fibers high mechanical, electrical and multifunctional properties and strong interactions with electrospun fiber matrices resulting in large interfacial area^[26–28].

CNTs have attracted much attention to researchers for decades due to their unique one dimensional structure and a range of fascinating properties. CNTs have been considered to be an ideal reinforcing material due to their extraordinary mechanical properties, high flexibility, low density, and high aspect ratio (typically > 1000)^[128]. Theoretical and experimental studies have shown that CNTs are extremely high tensile strength of 150 GPa with an elastic modulus of about 1.8 TPa which make them ideal materials for reinforcement in high performance electrospun fibers^[129]. In addition to their mechanical^[129] properties, the electrical properties of CNTs can be utilized to impart conductivity to nonconductive polymers which provides electrospun nonwoven mats additional advantage^[27,130].

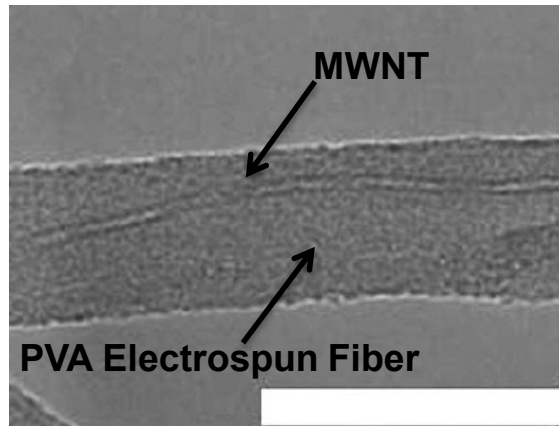


Figure 2.17 The SEM image of CNT-PVA electrospun fiber^[131]

2.3.3 Challenge of Using CNTs to Reinforce Nonwoven Mats

There have been many scientific reports on using SWNTs or MWNTs reinforce nanofibers or nonwoven mats. However, even though CNTs have tensile strength and elastic modulus, the expected degree of reinforcement has not been achieved yet^[129]. There are several factors such as adhesion between the polymer matrix and the fillers, purity, dispersion and alignment of CNTs which may be responsible for the observed results. In order to improve mechanical properties of electrospun nonwoven mats, these factors should be well understood and analyzed how to overcome them. Therefore, all these problems for producing the CNT – polymer electrospun nonwoven mats are explained in this chapter.

2.3.3.1 Dispersion and Alignment of CNTs in Polymer Matrix

The addition of CNTs could increase glass transition, melting and thermal decomposition temperatures of the electrospun nonwoven mats. However, the dispersion of CNTs into the polymer solution and the alignment of CNTs in polymer fiber as well as the interfacial interaction of CNTs with polymer have significant influence on final performance

of the CNTs – polymer electrospun nonwoven mat^[30,132–134]. Due to strong van der Waals interactions among CNTs, they usually exist as stable bundles, so their dispersion and alignment are very difficult to obtain in polymer matrix, which limits their applications in device design^[30,132–134]. Several different methods have been developed to achieve good dispersion of CNTs in the organic solutions of polymer. The most common strategies for dispersion are using high power ultrasonic mixers, functionalization of CNTs, surfactant assisted processing, the addition of coupling agents, and in situ polymerization in the presence of CNTs^[27,29,133–135]. Several papers proved that functionalization of CNTs improved mechanical properties even though it disrupted the extended π conjugation of CNTs, but functionalization reduced the conductivity of CNTs^[130].

Several different methods have been applied to align CNTs in polymer matrix, including ex situ methods and a range of force methods, such as mechanical shear, magnetic and electrical fields. Electrospinning is an ideal method for production of aligned CNTs based nonwoven mats^[136]. During electrospinning, when the electrostatic force applied, the polymer solution is stretched into fibers and CNTs are forced to align along the fiber axes. It is obvious that both single CNTs and bundled CNTs are parallel to fiber axes under the external electrostatic forces^[136]. However, the CNTs in polymer fiber should be straight, since bent, coiled, or spiral-shaped CNTs cannot be embedded in uniformly inside a 300 nm diameter nanofiber^[132], as seen in Figure 2.18. In order to make high strength CNTs – polymer nonwoven mat, pure, straight CNTs with no bent coiled, or spiral-shaped impurities are desired. Therefore, nanotube alignment is important, because in addition to mechanical

properties, functional properties, such as electrical, magnetic and optical properties, of CNTs – polymer nonwoven mat are linked directly to the alignment of CNTs in the matrix.

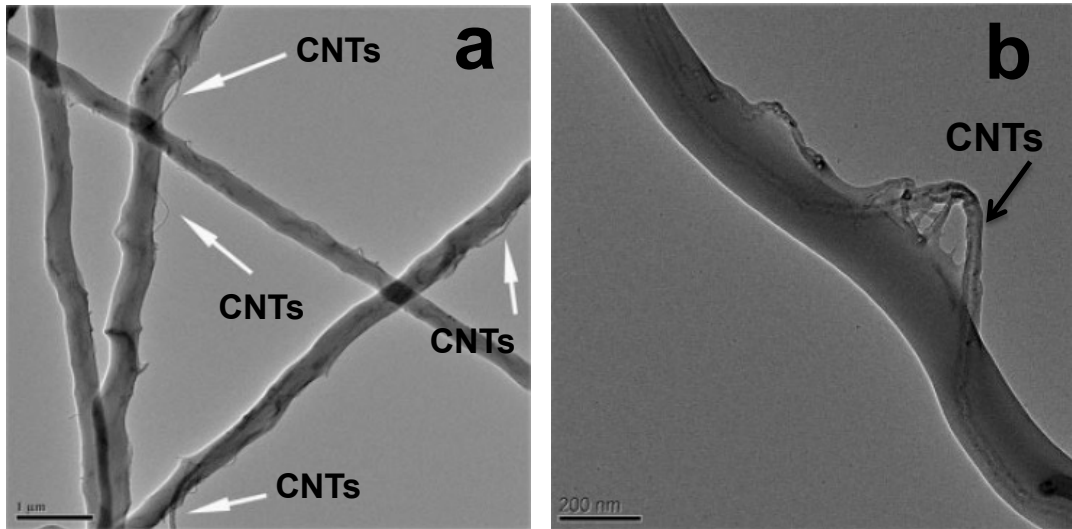


Figure 2.18 TEM images of PMMA-CNT nanofibers a) 1 μm scale bar, b) 200 nm scale bar^[132].

CNTs dispersion and alignment strongly affect the final CNTs – polymer nonwoven mats properties. In order to make good dispersion and alignment of CNTs in electrospun fiber, previous researchers have applied several different methods, such as functionalization of CNTs, surfactant assisted processing, the coupling agents, or in situ polymerization^[27,29,133–135]. Nonetheless, even after applying one of those special processing techniques, good dispersion and alignment of CNTs have not been successfully achieved yet.

2.3.3.2 CNTs Weight & Volume Fraction

One of the biggest disadvantages of CNTs – polymer electrospinning method is the CNTs weight or volume fraction in polymer solutions. Due to strong van der Waals forces interaction among CNTs, they always stay together as bundles. Therefore, addition of more CNTs into the polymer solution, it becomes more difficult to disperse the nanoparticles and large agglomerates are formed^[27], as seen in Figure 2.19. It shows optical microscopy on dispersion of CNTs at below rheological percolation (1% MWNTs, Figure 2.19a) and above percolation (4% MWNTs, Figure 2.19b), respectively. When the weight or volume fraction of CNTs increases in polymer solution, CNTs agglomeration increases.

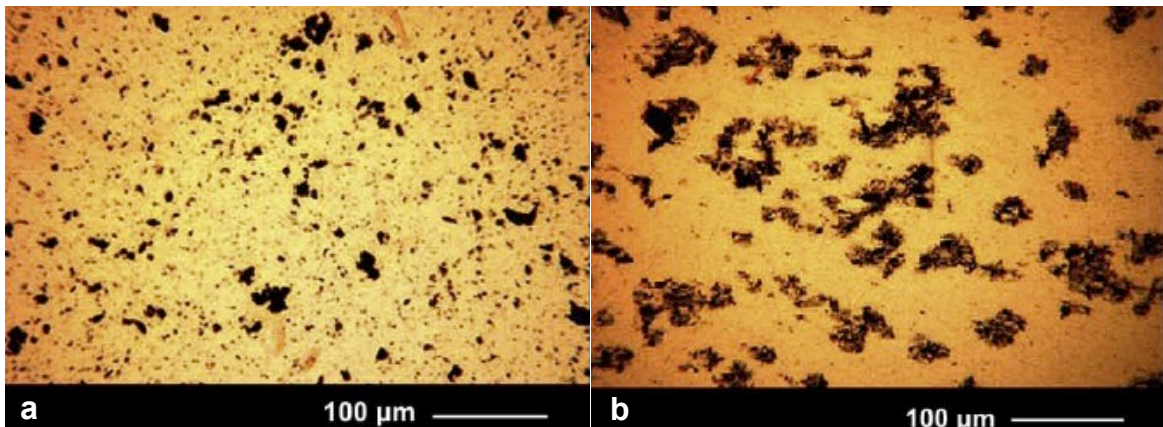


Figure 2.19 Optical microscopy on dispersion of CNTs into the polymer solution a) below rheological percolation (1% MWNTs), b) above percolation (4% MWNTs)^[27]

When CNTs weight or volume ratio is higher in polymer solution, large aggregates are formed inside nanofibers as shown in Figure 2.20. Their formation prevents the fibers from achieving a high degree of individual CNT orientation since it decreases the density of oriented CNTs in alignment direction. In addition, electrospun fiber diameters are strongly

dependent on CNT concentration. An increase CNTs weight or volume fraction enhances the conductivity of the polymer solution and produces a larger electrical current during electrospinning. The addition charge accumulation overcomes cohesive force and intensifies repulsive forces which cause decreasing of electrospun fiber diameter. Therefore, CNTs can easily move out from fiber at higher CNTs ratio. The scientific papers have showed that small fraction of CNTs (Around 1% CNTs) have showed the highest improvement on mechanical properties of CNTs – polymer nonwoven mats. When CNTs weight or volume fraction increases from 1% to 3-5%, the mechanical properties of final nonwoven fabric decrease and become worse than control nonwoven fabric^[27,126,135,137-139]. This is the most disadvantage of using this method, so the mechanical properties of CNTs- polymer electrospun nonwoven mats have not improved as high as the traditional nonwoven mechanical strength yet.

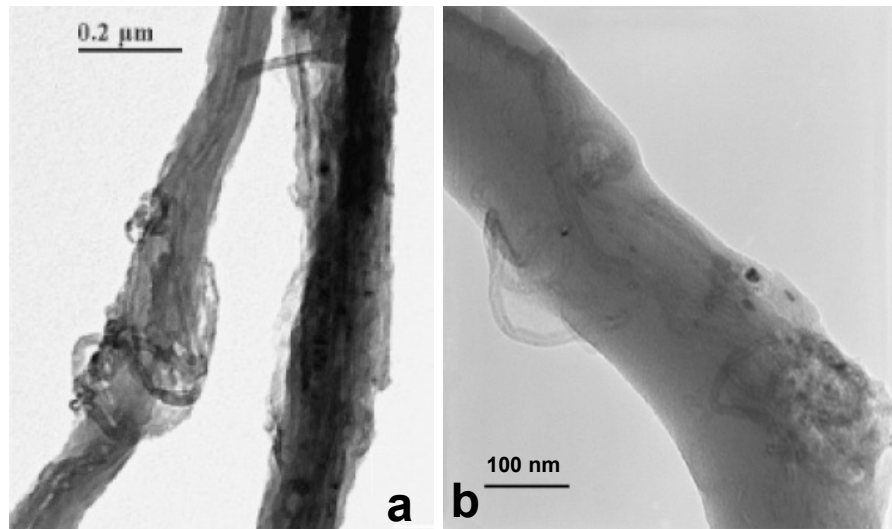


Figure 2.20 a) TEM image of 20% CNT^[126], b) TEM image of 5% CNT into polymer solution^[29].

2.3.3.3 Bead Formation

It is well known that the diameter uniformity and absence of beads in the electrospun nanofibers are the vital importance for fabricating electrospun nonwoven mats with good mechanical properties. As the polymer solution properties such as viscosity, surface tension, solution conductivity and electrospinning conditions, such as voltage, distance greatly influence the morphology of the final fiber structure and also final electrospun nonwoven mat properties^[140,141]. CNTs are directly affect the polymer solution conductivity, surface tension and viscosity. Several studies showed that addition of CNTs considerably decreased the viscosity of polymer solution. The reason for viscosity changes may be because of polymer chains break-up during sonication^[27,28].

Since addition of CNTs cause change the polymer viscosity, bead formation is observed along the fiber axis. Depending on the dispersion condition, addition of CNTs above percolation increases beads formation^[27,28] as seen in Figure 2.21.

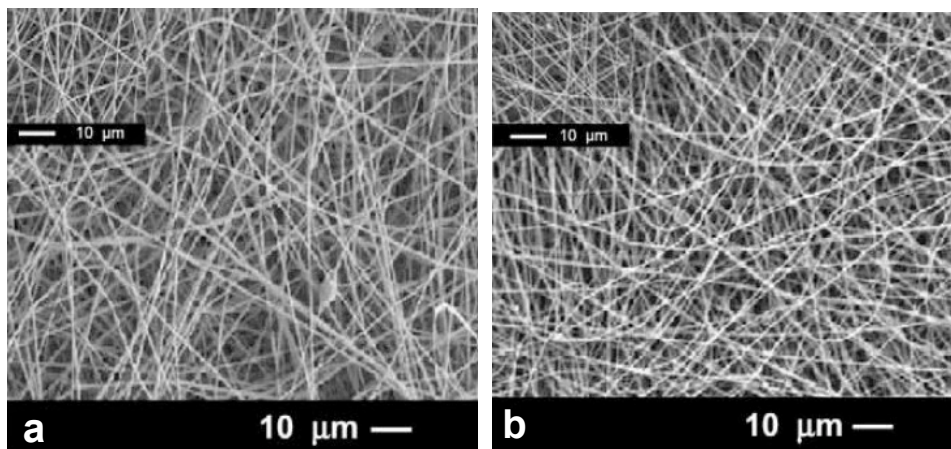


Figure 2.21 SEM images of a) 1% CNT, b) 7% CNT polymer electrospun nonwoven mat^[27].

When CNTs – polymer electrospun nonwoven mats are looked at optical microscope in order to detect CNTs localization inside the fibers, the images show that beads in CNTs-containing sections are filled with CNTs agglomerate, as seen in Figure 2.22. Even though fiber diameter and beads size decrease, the most of those beads contain CNTs. When CNTs ratio is less than electrical percolation threshold, there is no or little beads formation at nonwoven mat. However when CNTs ratio is above electrical percolation threshold, additional CNTs can cause a bead structure formation which is filled agglomerated CNTs. These beads formation negatively affects the mechanical properties of the nanofiber nonwovens due to dispersion of CNTs^[27,28]. Therefore, improvement of CNTs dispersion can help to decrease beads formation.

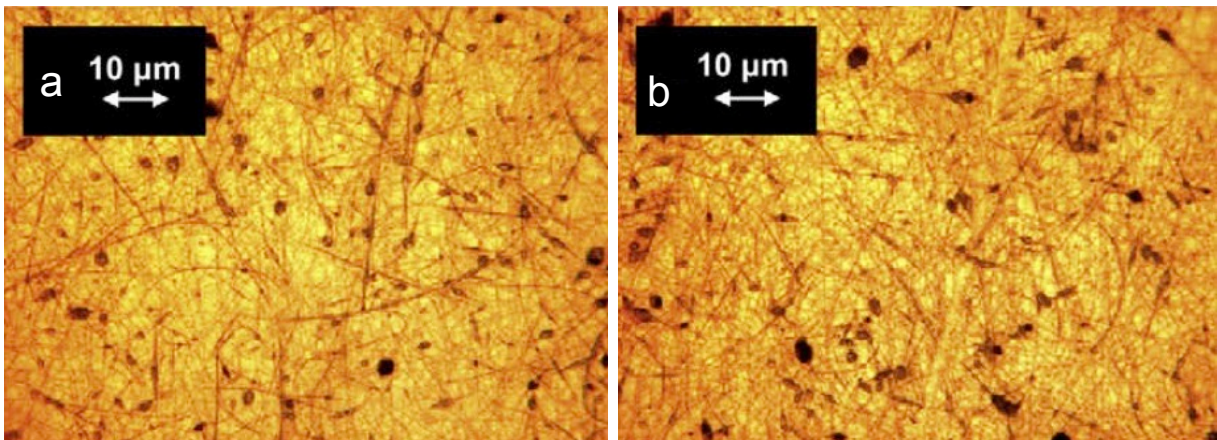


Figure 2.22 The optical microscopy of CNT-PS electrospun nanofibers a) 3% CNT, b) 5% CNT^[27].

Even though theoretical and experimental studies have shown that CNTs are extremely high tensile strength and elastic modulus, the expected degree of reinforcement has not been

achieved yet. The CNT reinforced polymer nanofiber fabrics typically show an increase in mechanical properties, but have been limited to a maximum increase in strength of ~4x while typically much lower gains are observed^[27,28,130,142]. Although CNTs embedded in fibers may help to make nanofiber fabrics strong enough to stand alone, they will not do anything to increase the specific surface area or enhance filtration properties.

2.3 Application of Nanofibers in Li-ion Batteries

2.3.1 Energy Sources and Storages

Energy storage materials and devices have made major advances over the last few decades. Wind, solar, tidal, and geothermal powers are one of the clean and natural energy sources, which make them very attractive, because it does not exchange energy in the price of damaging our environment. All these energy sources are excellent approaches, but they are not sole solution to generate energy. Finding a better source to generate power and energy storage is another direction that attracts last couple decades. There are different technologies available for energy storage in both large and small-scale applications^[143]. Among them electrochemical energy storage systems include battery and capacitors are the best option due to the fact that the approach is much more sustainable and environmental friendly^[144].

Several different materials have been studied in battery applications. Figure 2.23 shows the comparison of rechargeable batteries and their volumetric and gravimetric energy densities. From this figure, it is seen that lithium ion batteries much better than other battery technologies when comparing the volumetric and gravimetric energy densities. Lithium ion

batteries have several advantages such as, long cycle life, low self-discharge, no memory effect, so as a result of their characteristics, they can be used in various applications from personal electrical device including cell phones, laptops, cameras, to automobiles and larger applications, for instances, grids^[145].

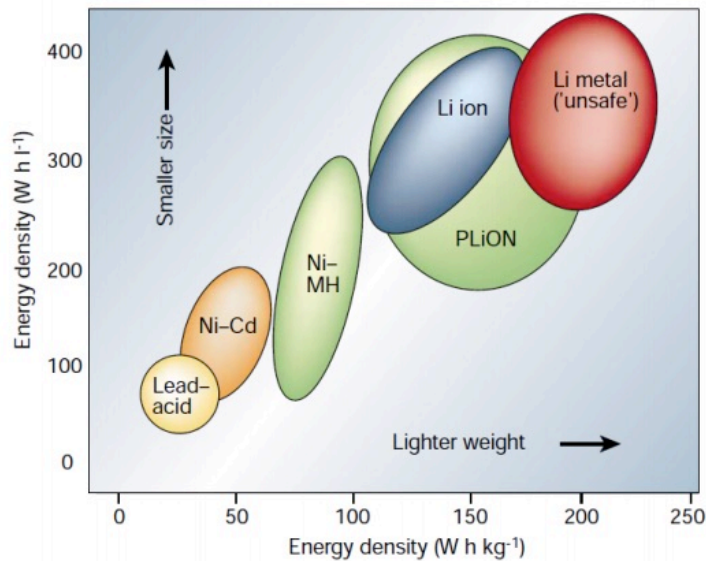


Figure 2.23 Comparison of different battery technologies in terms of volumetric and gravimetric energy densities^[145].

2.3.2 Mechanisms of Li-ion Batteries:

The physical structure of an electrochemical battery consists of three components: two electrodes, a separator, and electrolyte. Figure 2.24 shows the basic operating principle. During charging, lithium ions are produced from the LiCoO_2 , and it passes across the electrolyte, and then intercalate into the graphite layers in the anode. During discharging, lithium ions leave the graphite layers, and they transfer the through the electrolyte, and then

intercalate back into the layered cathode^[146]. The chemical reactions are shown in below:

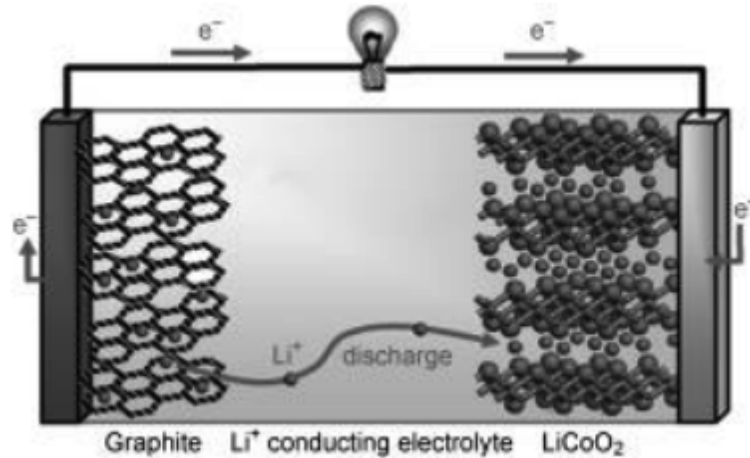
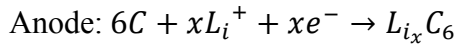
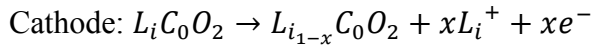


Figure 2.24 Schematic of lithium-ion battery^[146].

For lithium-ion battery electrodes, nano-structural design have attracted many people, because 1) nanostructures can increase the electrical conductivity due to the shortened electron transport pathway^[146,147], 2) nanostructures can improve the ionic conductivity of the electrode since the high surface area allows sufficient contact area with the electrolyte^[146,147], and 3) nanostructures can enhance the rate of lithium insertion and di-insertion of the electrode because of the short lithium ion diffusion distance between active materials^[146,147].

2.3.3 Si as anode materials:

The demand for lithium ion batteries has been increasing dramatically, especially ones that have high power, high capacity, and high rate capability. Graphitic material has been widely used as a commercial anode material for lithium-ion batteries because of its low cost, long cycle capacity, and low flat working potential. However, the theoretical capacity of graphite material is 372 mAh/g, which is insufficient to meet the capacity requirements of future portable electronics, and the high energy-storage demands in the transportation or grid storage applications. In order to meet these requirements, researchers have focused significant attention on alternative anode materials with higher capacities^[145,148,149]. Silicon, tin, germanium and their oxides are other alloy types of anodes, the lithium storage capacities of which are much higher than commercially used intercalation-type graphite anodes^[150,151].

Among all alloy type anodes, silicon (Si) has the highest theoretical capacity of 4200 mAhg⁻¹, which makes it one of the most promising anode materials for next generation lithium-ion batteries^[152,153]. Although Si has the highest capacity, the structural failure induced by large volume change (up to 400%) of Si during electrochemical cycling causes serious pulverization of active Si material and accelerates the formation of solid electrolyte interphase (SEI)^[156,154,155]. To overcome this problem, tremendous efforts have been made to improve the cyclability of Si-based anode materials, including reducing the Si particle size to the nanoscale, creating open spaces for active Si particles, Si anodes with different binders etc^[156,157].

2.3.4 Basic Functions of Binder

Binder is an important component in composite electrodes and plays an essential role in maintaining the mechanical stability of the electrodes. The requirement of binder system maintains high electronic conductivity, mechanical binding, ductility, and electrolyte uptake, because the electrochemical properties of active materials depend on binder systems. Therefore, efficient binder is crucially important for designing high performance battery system. However it is inevitable to decrease the electrical conductivity of active materials due to intrinsic features of binder system (conductive additive and polymer binder). It brings side effects inactive materials and the electrolyte even though the composition of electrode is well controlled. Therefore, inactive binder system detrimentally affects the cycling performance and reduces the overall gravimetric energy density of the electrode, which is extra unnecessary weight in the battery. In addition preparation binder is additional time and high cost which are other drawbacks for using binder system. Therefore, eliminating polymer binder and the conductive additive is crucially important to design high-energy electrodes^[158].

2.3.5 Carbon Nanotube Based Si nanostructures for Li-ion Batteries

CNTs have excellent physical properties such as electrical conductivity, low density and large surface area, which make CNTs as an ideal material for use in energy storage application^[56,56,159,160]. CNTs have been widely used as the conductive additives to form an electrical percolation network. CNTs enhance the number of electrical contact points compare to carbon black, so it increase the rate capability of the electrode. In addition a CNT

network can also provide mechanical strength to prevent the crack and pulverization of the electrode during cycling^[56]. There are many studies using CNT and Si in literature. The first study of CNT-Si electrode was reported from Kumta's group in 2010^[161]. In their work, MWCNTs were synthesized in a CVD system by using liquid injection of xylene (C_8H_{10}) as the hydrocarbon source and $(Fe(C_5H_5)_2)$ as the catalyst, and then silicon was deposited by the decomposition of silane (SiH_4) gas. The CNT-Si core-shell structure helps Si for volume change, but it was just reported 20 cycles charge and discharge process. Since the core-shell CNT-Si structure electrodes exhibited high capacity, researchers started to study core-shell design for better understanding of this structure. Zhang's group at Nanyang Technological University reported rationally design core-shell CNT-Si electrodes^[162,163]. The Si was deposited onto the vertically aligned CNT forest. Due to un-uniform deposition of sputtered Si, the cone shaped Si coating was formed. This rationally design core-shell CNT-Si structure exhibits a significantly improved cycling stability, with 90.4% retention of the initial capacity after 100 cycles. Si was deposited onto CNTs through atomic layer deposition or CVD coating system. In addition self-supported CNT-Si structures were studied in several different group, because CNTs can be easily assembled into self supported paper-like structure that exhibit lightweight, good flexibility, and mechanical stability. Cui's group at Stanford University reported lightweight, free-standing CNT-Si film structure first time^[164]. The CNT film was assembled by drying method, and silicon was deposited onto the CNT film by CVD method. Several other groups studied the similar work during the same period of time. Wang's group at University of Wollongong reported SWCNT-Si paper battery^[165].

Si was deposited onto/into SWCNT by pulsed laser deposition (PLD) method. However, the overall electrode capacity was low due to the small silicon content (<11.0 wt.%).

Several different groups were deposited Si onto CNTs with different methods. However, in Chapter 7, Si was deposited by a novel hybridization method, which provides Si nanoparticles more free volume for expansion in comparison to previous studies. The high capacity is reached, but it gives decreasing trend during long cycling.

Chaper 3 Experimental

3.1 Materials and Methods

3.1.1 Synthesis of Spinnable MWCNT Arrays

Vertically aligned multi-walled carbon nanotubes (MWCNT) were grown by chemical vapor deposition (CVD) on a quartz substrate using iron (II) chloride, anhydrous (99.5%, VWR) as the catalyst. First, iron chloride and substrate were placed inside a quartz tube. Then this inner tube was loaded into outer quartz tube of a horizontal tube furnace. The chamber was sealed and pumped to less than 10 mTorr, and then the chamber was heated to 760 °C. When the chamber's temperature reached 760 °C, the growth gasses, acetylene (600 sccm), argon (395 sccm) and chlorine (5 sccm), were introduced into the chamber. After 20 minutes, acetylene gas flow was turned off, and the arrays were kept treated with argon and chlorine gas flow for additional 20 minutes. Finally the chamber was returned to starting conditions (ambient temperature and atmospheric pressure) while purging with argon. CNT array height (and corresponding CNT length) was approximately 1 mm and the average diameter of CNTs 30-50 nm.

3.1.2 Preparation of CNT sheet – Nonwoven Aerosol Filter Structure

The aligned CNT sheets were formed by dragging a razor blade across one edge of the CNT array. Clean CNT surfaces and sufficient van der Waals interactions between tubes creates an attraction between tubes to allow them to be transferred from the aligned vertical orientation in the CNT array to the aligned horizontal orientation in the CNT sheet. Single

layer CNT sheets are very fragile and can be permanently deformed due to their very small thickness and low density. In order to utilize them in a filter structure, they were drawn onto the polypropylene (PP) melt blown nonwoven fabric to provide mechanical and structural support. The air filter construction process consists of several processes which are: 1) PP melt blown nonwoven fabric was fixed onto the rotating mandrel, 2) 6 cm width aligned CNT sheet was drawn onto the nonwoven fabric and the mandrel was rotated based on how many layers needed. In order to produce cross-ply structures, the sample was turned 90° on the mandrel after each rotation to alternate CNT sheet layers between 0° and 90°, 3) After removing the CNT sheet layer, another PP melt blown nonwoven fabric was placed on top, which sandwiching the CNT sheet layers in between, 4) The sandwich structure was placed between aluminum plates that contained a square cut out hole with the dimensions of 3.8 cm × 3.8 cm, and then the assembly was placed between hot-press platens and left under the load at 115 °C for 5 minutes. All the PP fibers under the aluminum plate were calendared, while the area of cut out of the aluminum was not exposed to the same heat or pressure. The unexposed square area was used for filtration evaluation.

3.1.3 Preparation of CNT sheet – Polymer Nanofiber Hybrid Fabric

In this dissertation, a novel CNT – polymer hybrid nonwoven fabric was created. To manufacture the novel hybrid fabric, the aligned CNT sheet was taken up onto an electrically conductive mandrel that serves one of the electrodes in the electrospinning process. As the mandrel rotates, the CNT sheet is taken up onto the rotating mandrel and at the same time

coated with a layer of electrospun polymer fibers. Two types of polymer were used in this dissertation: 1) Polyethylene oxide (chapter 6) and 2) Polymethyl methacrylate – Silicon (chapter 7).

In chapter 6, PEO polymer solution was chosen for electrospinning, because it is easily electrospun, and melts at low temperature. The 1 mm long CNTs become trapped by the polymer fiber layers, encapsulating them in the fabric. The mass fraction of the CNTs in the hybrid fabrics is easily controlled anywhere from 0–100% by adjusting the mandrel take-up speed during the process. Once the samples were prepared, two additional processing steps were completed to understand the effect of hybrid fabric structure on the properties. The first was to consolidate the fabric under 2 MPa of pressure without heat treatment for 5 min. The second was to calendar the samples at 70 °C and 2 MPa pressure for 5 min. In this chapter, the mechanical, electrical, aerosol filtration, permeability, and barrier properties of the novel hybrid fabrics are evaluated.

In chapter 7, the hybrid fabric was used in different application area by just changing the type of polymer solution. In this chapter, PMMA-Si polymer solution was chosen for electrospinning, because PMMA polymer nanofibers can be easily decomposed at elevated temperature and Si nanoparticles were homogeneously dispersed within the CNT sheets. PMMA solution was prepared by mixing 25 wt% PMMA in dimethylformamide (DMF) solution, and then stirring for one day. Then 15 wt% silicon particles (30-50 nm in diameters that were purchased from Nanostructures & Amorphous Materials, Incorporated) were added in PMMA + DMF solution and then stirred for another day. While producing a 30 layer CNT

– PMMA+Si hybrid structure through this process, 5 layer CNT sheets were rolled on the top and bottom of the hybrid fabric making a sandwich structure. The 5 layer sheets provided for a structure to enclose PMMA+Si electrospun nanofibers within the CNT sheets. The 40 layer CNT – PMMA+Si hybrid structures were placed onto a quartz substrate and then another quartz substrate was put onto hybrid structure. Then it was transferred into the horizontal tube furnace to decompose the PMMA polymer fibers. The decomposition process was carried out in Ar gas with a flow rate of 500 sccms at 500 °C for 1 hour. Then sample was coated with pyrolytic carbon via chemical vapor infiltration. This method was described in detailed elsewhere^[56], proceed by heating the CNT structures in vacuum. When the temperature reached to 760 °C, acetylene gas was flowed at 600 sccm while the system pressure was regulated at 30 Torr. After 60 minutes treatment, the system was shut down and allowed to cool to room temperature while being purged with argon gas at a flow rate of 1000 sccm. After pyrolytic carbon treatment, the hybrid samples were punched to the desired size to use as the anodes in coin cells.

3.1.4 Plasma Surface Modification

In order to make oleophobic polymer-CNT hybrid fabrics, a low surface energy chemical, PFAC8 ($C_8F_{17}CH_2CH_2OCOCH=CH_2$, Fluorochem, Derbyshire, UK) was deposited onto the CNT-polymer hybrid fabrics by using pulsed plasma polymerization. The treatment was carried out in a inductively coupled glass cylindrical glow discharge reactor, (10 cm diameter, $4.3 \times 10^{-3} m^3$ volume, 1×10^{-2} mbar base pressure) connected to a vacuum

pump *via* a liquid nitrogen cold trap. First, the hybrid fabric was placed on a glass slide which was then placed in the centre of the coils. The chamber was then evacuated to the base pressure of the apparatus, typically 1×10^{-2} mbar. Once base pressure had been reached, the PFAC8 vapour was introduced into the reactor. The reactor was purged with the vapour for five minutes, and once the pressure had stabilised at 8×10^{-2} mbar, the radio frequency (RF) generator was switched on to create a 40 W continuous wave plasma. This was allowed to run for 10 seconds. At this point the pulse generator was turned on, at a pulsing sequence of 40 μ s on, 20 ms off. Once a stable plasma deposition rate was established (indicated by uniform pulse envelope, using an RF probe and oscilloscope), the polymerization was allowed to run for two minutes. At the end of the treatment the RF generator was switched off and the reactor purged for 2 minutes with PFAC8 vapor, prior to being evacuated back to base pressure. Once base pressure was reached, the vacuum chamber was isolated from the pump, the system brought up to atmospheric pressure and the samples then removed.

3.2 Characterization

3.2.1 Microstructure Analysis

Scanning electron microscopy (SEM) was conducted on one of the two tools: a FEI XHR-Verios 460L field emission SEM with a beam voltage of 1 kV and Phenom World BV SEM (Model Phenom G1) with a beam voltage of 1.2 kV. All samples were imaged as-prepared without sputtering. Transmission electron microscopy (TEM) images were taken using a Hitachi HF2000 cold field emission TEM with a beam voltage of 200 kV. A probe sonicator was used to disperse small amount of CNTs or hybrid sample (CNT-Si) in 10 mL

of ethanol. The mixture was pulsed sonicated in an ice bath for 30 – 60 minutes. After ultrasonication, a small amount of the dispersion was deposited on holey carbon mesh, Cu TEM grids and then allowed to dry. X-ray diffraction (XRD) experiments were performed on a Rigaku SmartLab Bragg Brentano XD with a Cu K α radiation source ($\lambda = 1.5418 \text{ \AA}$). Step scans were performed for $2\theta = 10\text{-}90^\circ$ with a step with of 0.5° and a scan speed of 3 seconds.

3.2.2 Chemical Analysis

Raman spectroscopy measurements were performed using a Renishaw 2000 Raman microscope with a laser wavelength of 514 nm (50x magnification). Samples were first placed onto a microscope slide prior to spectrum acquisition and at least five spectra were obtained from different locations across the sample.

3.2.3 Electrical Analysis

Electrical properties of the hybrid samples and CNT sheets were measured using a four-probe resistance measurement system. The samples with dimensions of $0.5 \text{ cm} \times 4 \text{ cm}$ were placed onto a glass plate with four parallel gold electrodes across it. To ensure good contact between the sample and the gold electrodes, a square shaped piece of glass and a 500 g weight were placed on top of the samples during the measurements.

3.2.4 Mechanical Analysis

The tensile properties of samples were measured using a Shimadzu EZ-S instrument with a 100 N load cell and two insulating platens. Before tensile testing, a laser cutter (Epilog mini/helix – model 8000) was used to cut the paper frame for mounting the samples. Samples with dimensions of $40 \text{ mm} \times 4 \text{ mm}$ were cut along the longitudinal CNT direction by sharp

blade without damaging hybrid fabric. The thickness of the samples was measured by micrometer. Then samples were mounted to paper tabs with tape on both sides to prevent slipping and reduce stress concentration at the grips. The gauge length of the tensile hybrid samples was 20 mm and testing speed was 0.5 mm min⁻¹.

3.2.5 Aerosol Filtration Testing

The filtration properties of the CNT-nonwoven structures were performed using a TSI Model 3160 Automated Filter Tester. DOP (dioctyl phthalate) particles with diameters between 0.010 and 0.3 µm were generated by a collision type atomizer (DMA, TSI Inc., Model 3081) and were fed into the filter holder with an effective area of 6.45 cm². Two condensation particle counters (CPCs, TSI, Model 3760A) were used to measure the number of DOP particles in the upstream and the downstream flow. The flow rate and resistance were measured by a mass flow meter (TSI Inc., Model 4043) and electronic manometer (TSI Inc., Model 220).

3.2.6 Contact Angle Measurements

Contact angle measurements were conducted using a DropShape Analyser 100 (DSA100, Krüss, Germany). Probe liquids were water, hexadecane, ethylene glycol and diiodomethane (Aldrich UK, except for the water). Contact angle measurements were made using the built in software.

3.2.7 Moisture Vapor Transmission Rate (MVTR) Test

Moisture vapor transmission rate were conducted following ASTM E96 test method by using a MVTR tester machine in standard test condition lab (20 °C, 65% relative

humidity). The hybrid fabrics were sandwiched between two aluminum foil discs (adhesive on one side) that had a punched hole (3.81 cm diameter) in the center. This assembly was sealed in a metal dish (64 mm in diameter and 13 mm in depth) filled with 10 g of water. A vibration free turn table carrying 8 dishes rotated uniformly at 5 meters per minute to insure that all samples were exposed to the same average ambient conditions during the test. The assembled specimens in the metal dishes were allowed to stabilize for two hours before taking the initial weight. The specimens were weighed again after a 24 hours interval. The moisture vapor transmission rate (MVTR) was then calculated in units of $\text{g m}^{-2}\text{-24 hours}$.

3.2.8 Electrochemical Evaluation

The electrochemical properties of the hybrid samples were tested using CR 2032 type coin cells. The electrode mass was measured on a balance with a resolution of 0.01 mg. The average working electrode mass was 0.4-0.5 mg. The counter electrode was lithium ribbon (99.9% Aldrich) and the separator was Celgard 2400 membrane. The electrolyte used was 1 M LiPF_6 /ethylene carbonate (EC) + dimethyl carbonate (DMC) + diethyl carbonate (DEC) (1:1:1 by volume, MTI Corporation). Coin cells were assembled in a high-purity argon-filled globe box. Galvanostatic charge-discharge experiments were investigated the electrochemical performance at a constant current density of 100 mA g^{-1} with cut-off potentials between 0.1-2.0 V using a LAND-CT 2001A battery test system.

Chaper 4 Aligned Carbon Nanotube Sheet High Efficiency Particulate Air Filters

Ozkan Yildiz¹ and Philip D. Bradford^{1*}

¹Department of Textile Engineering Chemistry and Science

North Carolina State University, Campus Box 8301, Raleigh, NC USA 27695

Abstract

Aerosol filters, made with conventional micro-fiber fabrics, are designed to efficiently capture small particles from the air. Filters constructed of nano-fiber fabric structures provide even greater filtration efficiency than conventional micro-fiber fabrics due to their higher surface area and smaller pore size. Carbon nanotubes (CNTs) are very small diameter fibers that have the potential to be integrated into filters to further increase particle capture efficiency. In this study, CNT sheets, drawn from millimeter tall CNT arrays, were integrated between traditional micro-fiber fabrics to produce aerosol filters. The filtration performance of the novel filters showed that when the number of CNTs layers increased, the filtration efficiency increased dramatically, while the pressure drop also increased. In order to meet high efficiency particulate air (HEPA) filter requirements with a reasonable pressure drop, CNTs were laid in a cross-ply structure within the filter. The results demonstrated that the three layer cross-ply structure provided 99.98% filtration efficiency at 0.3 μm particle size at a 10 cm/s face velocity, making it a viable method for producing low basis weight HEPA filters utilizing CNTs as the main filtration component.

4.1 Introduction

Recent research has shown that poor indoor air quality can cause dramatic health problems, such as respiratory diseases, allergies, asthma, and even tuberculosis^[166–169]. Inadequate ventilation, lack of efficient filtration and the presence of numerous synthetic chemical sources and particulates have paved the way for the increase in occurrence of these diseases^[167,169]. One of the most effective strategies for reducing the impact of harmful particulates is to use high efficiency particulate air (HEPA) filters in combination with adequate air ventilation^[170]. Filter products are constantly increasing in performance through higher particle collection efficiency and lower pressure drop across the filters. One area that has generated much research interest lately is the use of small diameter fibers with a nonwoven structure to improve the filtration efficiency at the most penetrating particle size^[171].

Nonwovens are widely used in aerosol filtration products. They are made of micron diameter fibers which provide physical, particle size-based separation. It is well known that when fiber diameter decreases, filtration performance is enhanced because of the higher surface area and smaller pore size^[172]. Filters with fiber diameters on the nanoscale are capable of the best capture efficiency. However, as the fiber size drops, the pressure drop across the filter increases due to decreased pore size. Increased pressure drop increases the energy cost for moving air through ventilation systems or makes breathing uncomfortable in personal respirators. Even though nano-fibers cause higher pressure drops, efficiencies of

particle interception and inertial impaction increase enough to compensate for the higher pressure drop. Therefore, submicron size fibers show the best filtration efficiencies^[171].

The interest in using fibers with small diameters for filtration has increased significantly for several decades. The most commonly used techniques for producing small nonwoven fiber structures include: melt-blowing, spun-bonding and electrospinning. The spun-bonding process is limited to producing fiber diameters down to 10-15 μm . In the melt blowing process, thermoplastic polymer melt is rapidly drawn from the spinnerets using high speed air jets and rapidly cooled to form small fibers. The melt blowing process has produced fibers down to approximately 500 nm; a fiber diameters generally range from 0.5-5 μm ^[76,114]. Electrospinning is a process of electrostatic fiber formation using electrical charge to produce micro- or nano-fibers from a polymer solution^[16,80-82,171]. In this method, synthetic polymer fibers such as nylon-6^[16,80-82], polyurethane^[83], polycarbonate^[83], and polyethylene oxide^[12,83] are electrospun onto a melt blown or spun bond nonwoven fabric surface which acts as a support for the very thin and weak electrospun layer^[12,13]. Electrospinning is the predominant commercial method to produce polymer fibers diameters down to 100 nm. Even though electrospinning is one of the most promising technologies for lightweight, low basis weight HEPA filters, minimizing the high pressure drop they produce is the biggest challenge of this method^[172,173].

Due to their very small diameters and high specific surface area, carbon nanotubes (CNTs) have been incorporated with conventional polymeric fibers with the intent of improving filtration efficiency. Depositing CNTs onto nonwoven fabric surfaces increases

the fiber surface area and creates a tortuous path for nanoparticles, thus increasing the probability of particle capture through the interception, diffusion and impaction mechanism^[14,89,90]. In the first studies of this kind, CNTs were directly grown on the surface of glass fibers^[14] or nickel fibers^[89] in order to reduce the pore size. In another method, CNTs were dispersed in solution vacuum filtered onto the filter media^[90]. However, as liquid dries from CNT solutions, CNTs agglomerate and bundle together, thus reducing their surface area. In those three references, the CNTs were very short and their release or removal from the filter could cause potential health concerns, negating the positive impact of the increased filtration efficiency. Studies have shown that CNTs are hazardous to lung cells over long periods of exposure^[174-177]. The goal of this study was to integrate millimeter long CNTs into traditional fabrics in such a way that the CNTs would be trapped in the fabric and would act only as a filtering agent.

Chemical vapor deposition (CVD) processes, where catalyst nanoparticles are deposited on a substrate, are often used to produce vertically aligned CNT arrays. These arrays can contain CNTs with lengths up to tens of millimeters. Vertically aligned CNTs have been extensively studied in different fields due to their unique structure and unique properties^[178-180]. In special cases, where the quality and morphology of CNT arrays is just right, the CNTs can be drawn off in continuous sheets which exhibit preferential alignment of the CNTs^[179,181,182]. These sheets are extremely thin and semi-transparent. The CNTs within the sheets are, for the most part, not bundled unless liquid is used to consolidate them. These sheets are a great candidate for air filtration structures and have not been examined in this role thus far.

The objective of this study was to prepare novel filters by drawing aligned CNTs sheets and embedding them between polypropylene melt-blown nonwoven fabrics using calendaring. The filters were prepared with an increasing number of CNT sheets in two different layup orientations. The filtration characteristics of the novel filters were collected and the results were evaluated in terms of collection efficiency and pressure drop, and then compared with other studies utilizing CNTs and electrospun fibers.

4.2 Materials and Methods

4.2.1 Materials and Instrumentation

The polypropylene melt-blown fabric, used as the face sheets for the laminated filter structure, was provided by The Nonwovens Institute at North Carolina State University. This fabric's basis weight was 121 g/m². Iron II chloride (FeCl₂) was purchased from Fisher Scientific. The gases used in the CNT synthesis were scientific grade (99.999%), except for the acetylene which was atomic absorption grade (99.5%). Scanning electron microscopy (SEM) data was collected using a Phenom World BV SEM (Model Phenom G1). Transmission electron microscopy (TEM) was used (Cold Field Emission TEM, Model Hitachi HF2000) to determine the CNT diameter range. The filtration and pressure drop data was collected using an TSI Automated Filter Tester 3160 .

4.2.2 CNT Array Synthesis and CNT Sheet Analysis

CNT arrays, with individual CNT diameters of 25-40 nm and length of 1 mm, were synthesized via a chloride-assisted low pressure CVD process, similar to the one demonstrated by Inoue in 2008^[183]. In our method, iron II chloride (FeCl₂) powder and quartz

substrates were placed in a custom built CVD reaction chamber. The reactor had a 76 mm sealed quartz tube inside of a tube furnace. Growth gasses were precisely controlled by mass flow controllers. The chamber was sealed and pumped to less than 10 mTorr, and then the chamber was heated to 760°C. When the growth temperature was reached, acetylene (600 sccm), argon (395 sccm) and chlorine (5 sccm) gases were released into the chamber. The growth gases were turned off after 10 minutes, producing a CNT array 1 mm tall and highly drawable in nature, as seen in Figure 4.1a. Typical array purity was approximately 99.5%, with the remainder being residual iron catalyst, as determined by energy-dispersive x-ray spectroscopy. The thickness of the CNT sheets was approximated by stacking many layers of the CNT sheet material, measuring the thickness using optical microscopy and then dividing by the number of layers. The average thickness of CNTs sheet was determined to be 20-25 μm which corresponded to the individual sheet cross sectional thickness as seen in Figure 4.1b. CNT sheet basis weight was calculated by winding multiple layers of the sheet, measuring the total mass and then dividing by the total area of the wound sheet. Figure 4.1c shows the top surface and typical spacing between CNTs within the sheet while Figure 4.1d shows a TEM image of typical CNTs that make up the sheets.

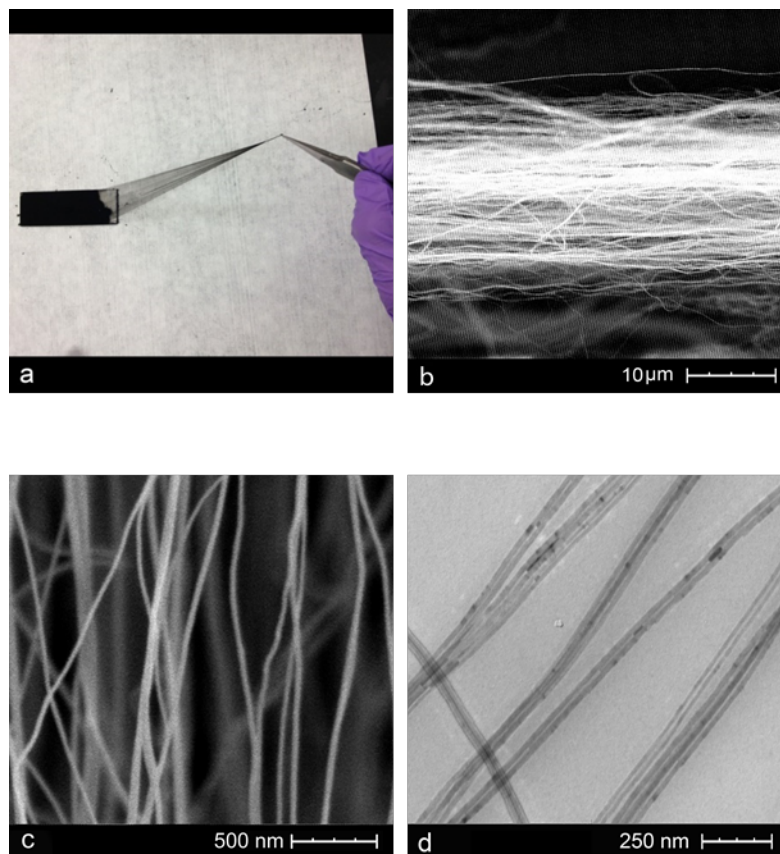


Figure 4.1 (a) CNT sheet being drawn from the array using tweezers, (b) SEM image of the side view of the CNT sheet showing the approximate thickness and low density structure, (c) High magnification SEM image of the top of the CNT sheet showing the spacing between CNTs and (d) TEM image of CNTs from the sheet.

4.2.3 Preparation of CNT Sheet Aerosol Filter Structures

Single layer CNT sheets are very fragile because of their very small thickness and low density. To utilize them in a filter structure, they were drawn onto the polypropylene melt blown fabric to provide mechanical and structural support. The polypropylene fabrics also served as both a pre-filter and a means to trap the CNTs. The air filter construction

process consisted of several steps which are shown in Figure 4.2a-d. In the first step, the polypropylene melt blown nonwoven fabric was fixed onto a mandrel. A 6 cm wide CNT sheet was then drawn onto the fabric. The mandrel was rotated to produce the number of layers needed. To produce the cross-ply structures, in which the CNT layers alternated between 0° and 90° , the sample was turned 90° on the mandrel after each rotation. After removing the CNT sheet coated fabric from the roller, another identical polypropylene fabric layer was placed on top, sandwiching the CNT sheet layers in between. The edges of polypropylene fabrics were thermally bonded together to create a robust filter structure. The three layer structure was placed between aluminum plates that contained a square cut out hole with dimensions of 3.8 cm x 3.8 cm. The assembly was placed between hot press platens and left under load at 115°C for five minutes. All of the polypropylene fibers under the aluminum plate were calendared together, while the area cut out of the aluminum was not exposed to the same heat or pressure, leaving a pristine multi-layer fiber structure for filtration evaluation.

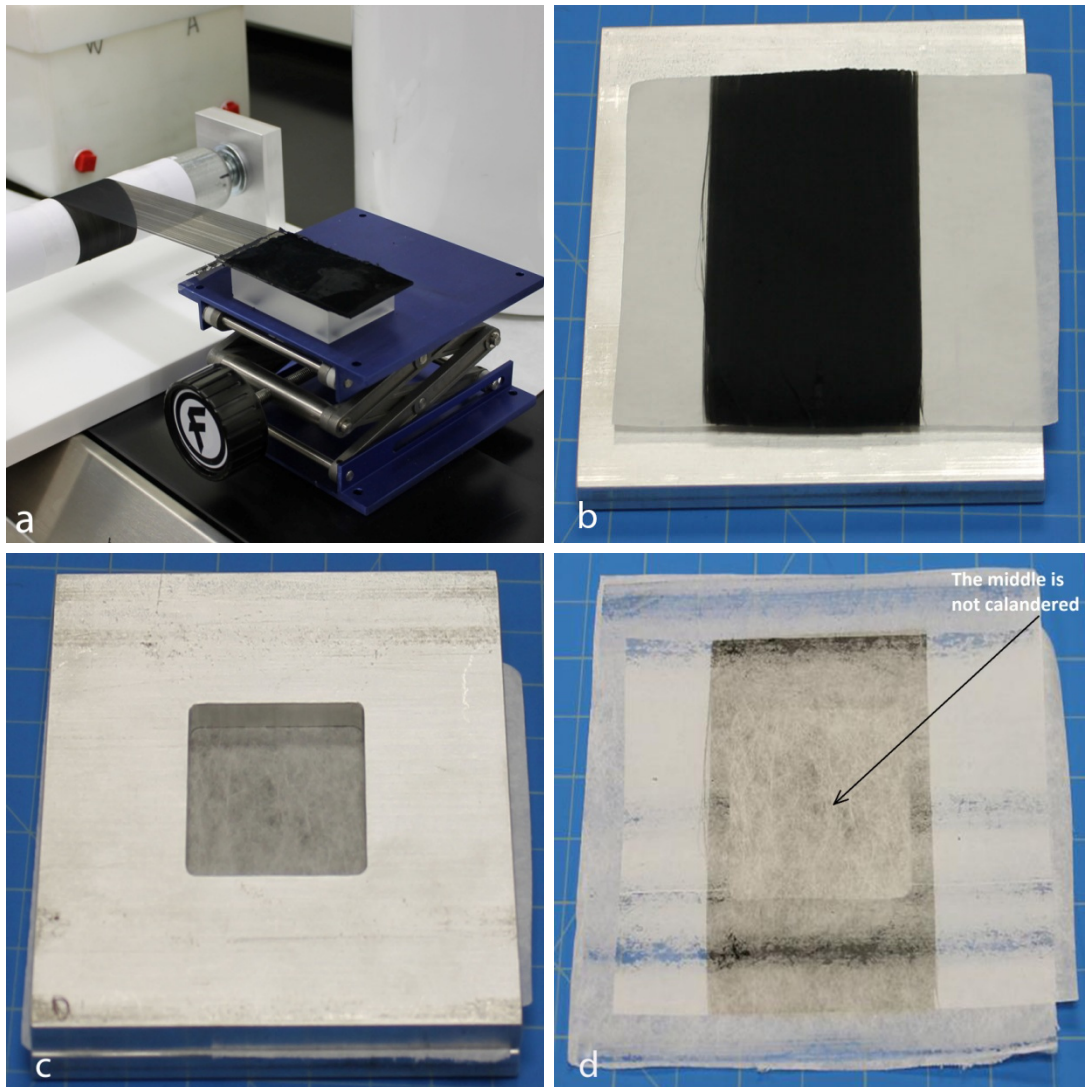


Figure 4.2 Preparing filters by (a) winding CNT sheets onto the polypropylene fabric, (b) placing CNT sheet - polypropylene fabric layered structure onto a calendaring plate with hole in the middle, (c) covering with a second layer of polypropylene fabric and second calendaring plate and (d) the final calendared fabric with pristine multi-layer structure in which the middle square section was not exposed to heat or pressure.

4.2.4 Filtration Evaluation

The filtration properties of the multi-layered fabric structures were tested using a TSI Model 3160 Automated Filter Tester. Specific parts within this tester are listed in the testing description below. The filtration efficiency of the control sample (two polypropylene nonwoven layers only) and samples containing CNT sheet layers were evaluated at 10 cm/s face velocity. DOP (dioctyl phthalate) particles with diameters between 0.010 and 0.3 microns were generated by a collision type atomizer and were fed into the filter holder with an effective area of 6.45 cm². Two condensation particle counters (CPCs, TSI, Model 3760A) were used to measure the number of DOP particles in the upstream and the downstream flow. The collection efficiency was calculated using the following equation:

$$E = 1 - \frac{C_{down}}{C_{up}} = 1 - P \quad \text{Equation 28}$$

where, E is the fractional efficiency of a specific size of DOP particles, C_{down} and C_{up} are the number concentration of particles on the downstream and upstream sides, and P is the particle penetration fraction. An electronic manometer was used to measure the filter resistance.

The pressure drop across a filter, Δp can be estimated using the empirical correlation^[184]:

$$\frac{\Delta p}{L} = \frac{64\mu U}{d_f^2} \alpha^{3/2} (1 + 56\alpha^3) \quad \text{Equation 29}$$

where, Δp is pressure drop, L is filter thickness, U is the face velocity, α is the fiber packing density, μ is the air dynamic viscosity, and d_f is the fiber diameter.

When the fiber size decreases, both the filtration performance and pressure drop increase. The quality factor (QF), the ratio of particle penetration to resistance, takes into account both of these factors and is defined as:

$$QF = -\frac{\ln P}{\Delta p} \quad \text{Equation 30}$$

The QF is a quantitative way to compare filter structures with a range of filtration efficiencies and pressure drops.

4.3 Results and Discussion

A single layer of the CNT sheet material had an average basis weight of 0.0325 g/m², which was approximately 7400 times smaller than the basis weight for polypropylene control fabric. A large array with a mass of 1 g could coat approximately 30 m² of fabric with a single layer of the CNT sheet. The CNT sheet can be drawn from the array very quickly, at speeds up to 0.5 m/s, allowing this method (after scale up of the array growth process), to rival the speed of large scale electrospinning processes. The 6 cm wide sheet used in this study is one of the largest width drawn CNT sheets demonstrated in the literature. The arrays were extremely drawable and their dimensions limited only by the dimensions of the CVD tube furnace. The typical morphology of the polypropylene nonwoven is shown in Figure 4.3a-b. The fibers range from 2-4 μm in diameter. Figure 4.3c-f show SEM pictures of the CNT sheet structure covering the polypropylene fabric. Figures 3c-d show the 1-layer CNT structure, where the underlying polypropylene fabric can be discerned in some areas. Figure 4.3e-f show the 3-layer CNT structure which exhibits fewer gaps than the 1-layer structure

while the underlying fabric became completely hidden. At lower magnifications, the nanofibers appear to be parallel to each other, but when they are viewed at higher magnification, more of the inherent waviness and entanglements are visible. Due to the extremely low density of the CNT sheets and the high depth of field in the SEM images it was difficult to determine the average spacing between CNTs. However there appeared to be a wide range of spacing, with some CNTs bundled together or tens of nanometers apart, and others many hundreds of nanometers apart. We have measured a bulk density for our CNT sheet structures of approximately 0.002 g/cm^3 . Based on an approximate CNT density of 2.0 g/cm^3 , the pore volume of the CNT sheets was 99.9%. Average spacing between the CNTs was calculated to be ~ 400 nanometers based on the theoretical packing of aligned cylinders, taking into account the fiber volume fraction and diameter. This value corresponds well to the CNT spacings seen in Figure 4.1c. The average fiber spacing was larger than the largest particle size used in this study, so mechanical sieving should not be a significant factor in the filtration efficiency. The low density structure and large spacing between fibers can only be explained by the extreme stiffness of the CNTs. The carbon nanotubes have an elastic modulus that is around three orders of magnitude greater than undrawn polymer nanofibers. This mechanical property allows the CNTs to span large distances without sagging under their own weight.

The polypropylene nonwoven fabric was used as a base fabric to provide mechanical and structural support for the CNT sheets. This fabric was chosen because its pores were small enough to trap the CNTs by the outer layers of the fabric, but still large enough that the filtration efficiency of the polypropylene fabrics alone was very low, allowing us to highlight

the effects of the CNT sheets. As seen in Figure 4.3, the pore size of the polypropylene fabric is in the range of tens of microns. Because the CNTs in the sheets are aligned, a single CNT, which is 1 mm in length, will span at least 20 surface pores of the polypropylene fabric. A single CNT will span the whole length of the fabric section seen in Figure 4.3a (which has a width of 400 μm). To demonstrate the effectiveness of the polypropylene fabric in trapping the CNTs, a nucleopore membrane with hole size of 400 nm was placed behind the 3-layer filter assembly to trap any CNTs that might penetrate. The face velocity was doubled to 20 cm/s. After one hour, the porous membrane was removed and examined under SEM. At least 30 random locations were sampled and there was no evidence of millimeter long CNTs or CNT fragments.

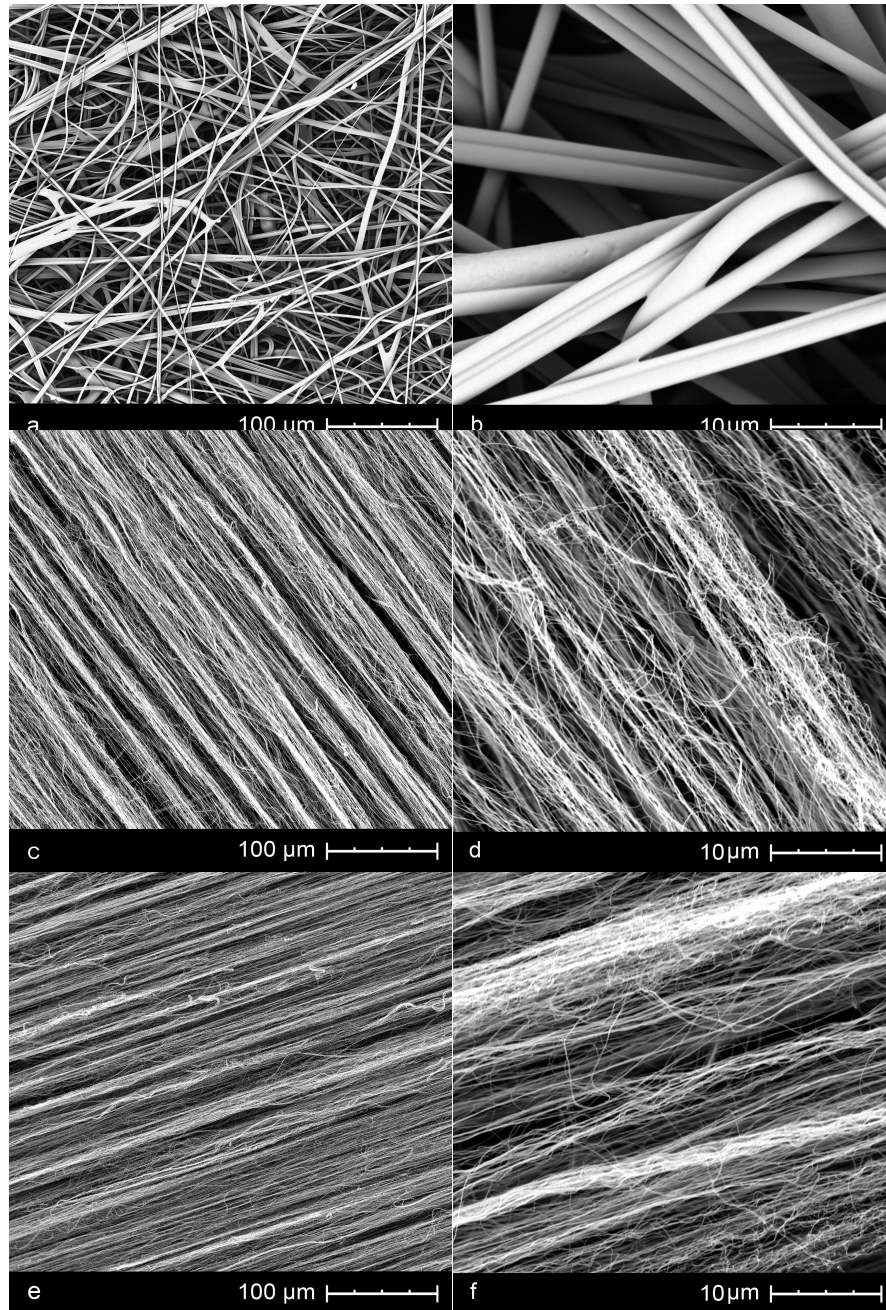


Figure 4.3 SEM images, at two different magnifications, of a-b) polypropylene melt blown fabric (control sample), c-d) 1-layer CNT sheet on the polypropylene fabric, e-f) 3-layer CNT sheet on the polypropylene fabric.

When particles pass through a fibrous filter, they are captured by the filter through a combination of mechanical sieving, Brownian diffusion, interception and inertial impaction^[14,76,89,90]. The specific fiber characteristics and fiber packing geometry will dictate which of the four mechanisms will have the most influence on the capture of particles of a particular size. Filters are, therefore, exposed to a range of particles sizes, because they often behave differently and can have different efficiencies at each particle size. The particle size at which the efficiency is the lowest is regarded as the most penetrating particle size (MPPS). This often occurs at around 0.3 μm which is one of the reasons why that size is chosen for the HEPA filtration standard. The requirements for HEPA designation is a filtration efficiency of 99.97% at 0.3 μm particle size^[82].

Figure 4.4 shows the filtration performance of the multi-layer structures, in terms of the particle penetration percentage, for the 10-300 nm particle size range tested. The plot shows data for the control sample and multi-layer CNT samples where all the CNT sheets are stacked in the same direction. The control sample was inefficient, capturing only 34.04% of the particles at the 0.3 μm particle size. Adding a single layer of the CNT sheet dramatically increased the filtration efficiency to 88.62% at the 0.3 μm particle size. Adding additional layers further increased the efficiency. The 3-layer CNT fabric was very close to meeting the HEPA standard while the 7-layer CNT structure filtered out at least 99.9997% of the particles at 0.1 μm or greater which met the Ultra-low Penetration Air (ULPA) standard of filtering out at least 99.999% of particles greater than 0.12 μm . The MPPS for the filters containing the CNT sheets was around 0.09-0.1 μm which is much lower than that of typical filters (see control sample), but in a similar range to other filters which contain nano-

fibers^[12,13,184]. With the CNT diameter remaining constant, the increase in efficiency, with an increased number of layers, was due to the increase in the CNT sheet solidity and thickness. The single layer filter showed some small gaps, in the range of microns that are inherent to the sheet after it is drawn from the array. After the second layer was added, these gaps were, for the most part, filled. Due to this gap coverage, we propose the large difference in efficiency between layers one and two was partially the result of increased filter solidity and additional layers improved filtration efficiency through increasing the filter thickness^[112].

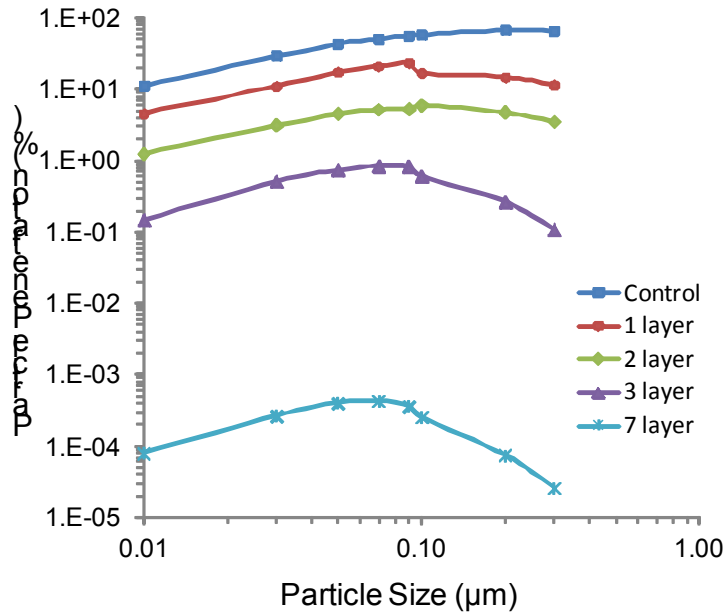


Figure 4.4 CNT sheet - polypropylene nonwoven fabric filters with increasing number of CNT sheet layers, evaluated for particle penetration percentage for a range of particle sizes at a face velocity of 10 cm/s.

It was hypothesized that when multiple CNT sheets are layered on top of each other, the radial force from the winding process may compact the sheet structure forming more bundles of CNTs, as opposed to individualized CNTs. This effect would then decrease the effective fiber surface area and increase the fiber packing density in the sheet, leading to lower capture efficiencies. To test this theory, we produced 2- and 3-layered cross-ply structures to compare to the 2- and 3-layer samples with all CNTs parallel to each other. All of the other fabrication and testing steps remained the same. Figure 4.5 shows images of the 3-layer cross-ply CNT sheets as seen in both SEM and photographic images.

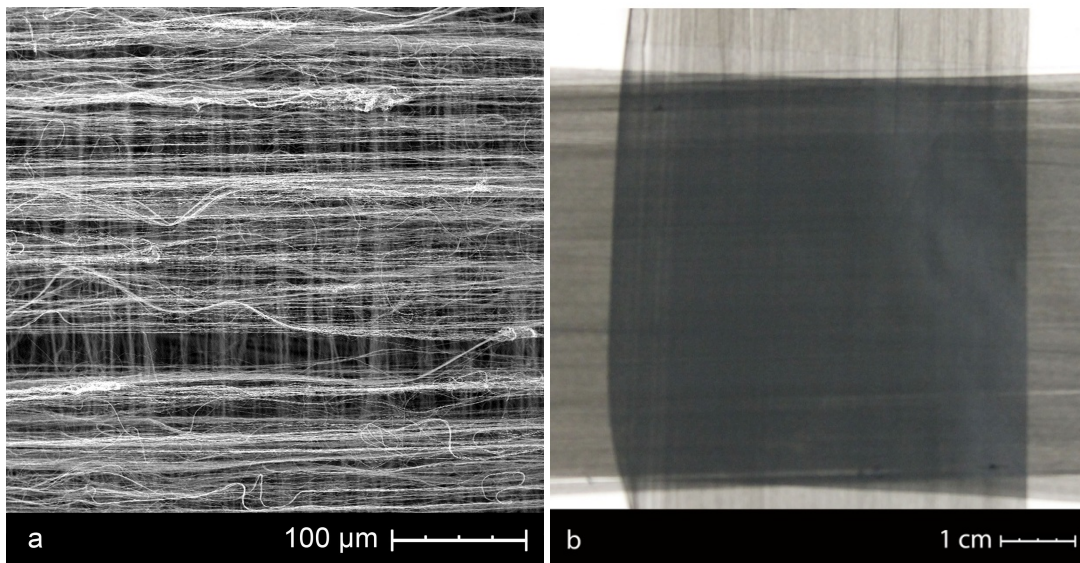


Figure 4.5 (a) SEM and (b) photographic images of the 3-layer CNT filter structure with the cross-ply geometry.

Figure 4.6 shows the filtration performance comparison between the 2-layer and 3-layer CNT sheet structure with the parallel and cross-ply layup directions. The cross-ply geometry provided increased filtration efficiency for both thicknesses. The 2-layer cross-ply structure showed 99.15% filtration efficiency at 0.3 μm particle size while the 3-layer cross-ply met the HEPA filter requirements with the value of 99.98%.

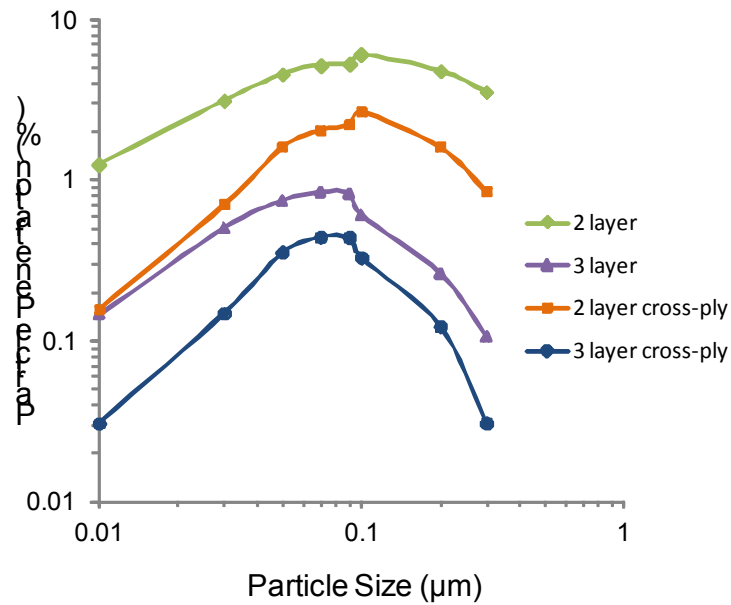


Figure 4.6 The filtration performance of filters consisting of 2-layer, 3-layer, 2-layer cross-ply, and 3-layer cross-ply CNT sheet orientations at a face velocity of 10 cm/s.

Pressure drop is another significant parameter for aerosol filtration. Pressure drop significantly affects energy requirements in large scale filtration processes and breathing comfort in personal filtration; thus, a low pressure drop is always a desired filter property. Pressure drop is affected by face velocity, the solidity, fiber diameter, thickness of filter media and fiber packing density. When the face velocity increases, the pressure drop

increases as well^[14,16,81,112]. In this study, the pressure drop across the test filters was assessed at 10 cm/s face velocity. As seen in Figure 4.7, the control sample gave a 51.3 Pa pressure drop. After depositing a single layer sheet of CNTs onto the polypropylene fabric, the pressure drop increased to 84 Pa. This trend continued for each additional layer added. The 7-layer coated fabric showed very high filtration efficiency but the pressure drop was also higher than desired for most applications. The pressure drops for all samples, excluding the 7-layer, were within a reasonable range for filtration products. The results also showed that cross-ply CNT and unidirectional CNT structures gave similar pressure drop values at the equivalent number of layers; however, the cross-ply geometry exhibited higher filtration efficiency. Fotovati et al. studied the effects of fiber orientation on the performance of aerosol filtration media and found that for nano-fiber filters, decreasing the in-plane orientation increased the quality factor. Cross-plying the CNT sheet structures may produce an equivalent effect of decreasing the average orientation of the CNTs, and therefore increasing the quality factor of the CNT sheet filters.

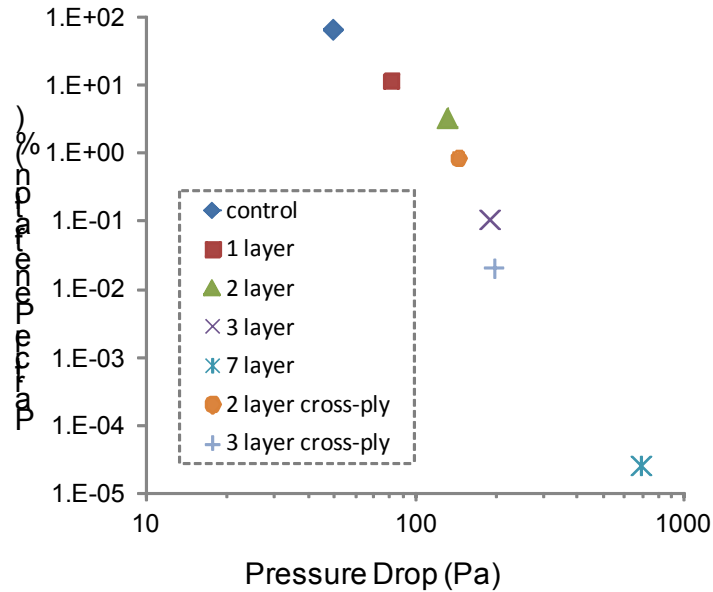


Figure 4.7 Particle penetration fraction of the different structures as a function of pressure drop at 0.3 μm particle size and 10 cm/s face velocity.

The QF was calculated based on experimental data of the filters' efficiencies and pressure drops using Eq. (3). Figure 4.8 shows the comparison of the QF between the CNT sheet filters and the control sample. The control sample had a lower QF, because larger diameter fibers have a lower single fiber filtration efficiency. The QF of the 1-layer CNT sheet coated fabric made a dramatic improvement. When the number of CNT sheet layers increased from one to three, the QF again increased substantially because filtration efficiency increases were more significant than the pressure drop increases. The 3-layer cross-ply structure had the highest quality factor which, again, is in agreement with the findings that decreasing the average orientation of the fibers increases the QF^[110].

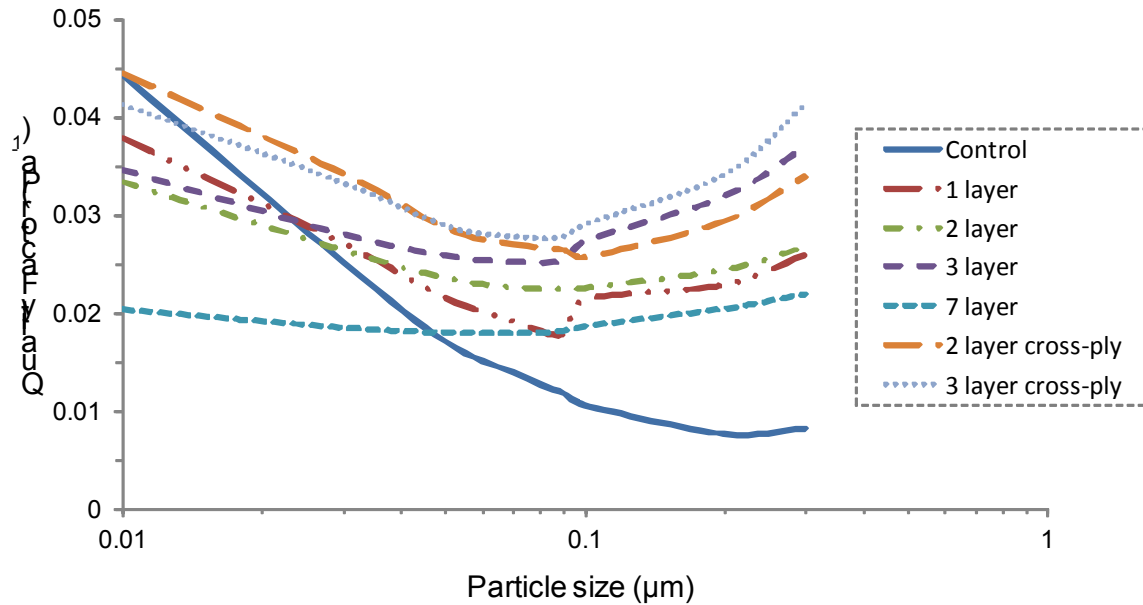


Figure 4.8 Quality factor as a function of DOP particle size, ranging from 0.01-0.3 μm , at 10 cm/s face velocity.

Preparation of aerosol filters, via aligned CNT sheets, is a novel method. In this method, long CNTs were used to increase filtration efficiency. Our review of other nanofiber filtration systems revealed that the filtration efficiency performance of the CNT sheets was comparable to, or higher than, many filters produced by the electrospinning method. Figure 4.9 shows a comparison of our results with other nanofiber filtration systems from the literature that did not use electrical charge to enhance filtration. All of the data points are from experimental data collected at a face velocity of 10 cm/s or lower (lower face velocity gives lower pressure drop) for the particle size of 0.3 μm ^[12–14,16,76,80–83,89,90,112,184–187]. If multiple structures were tested in a single reference, the data point we generated represents the data point closest to the HEPA standard.

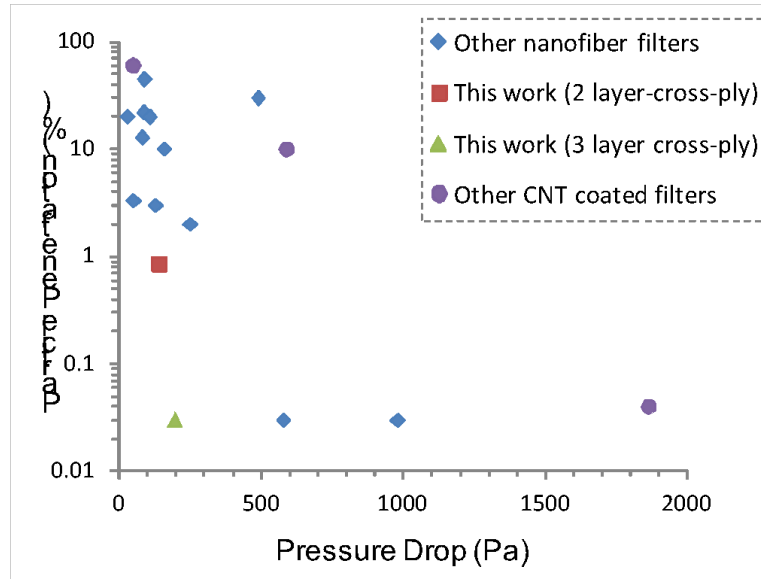


Figure 4.9 Comparison of particle penetration vs. pressure drop from nanofiber filters, including CNT coated filters, from the literature. These points were taken from studies using a face velocity of 10 cm/s or lower and with a particle size of 0.3 μm .

We expected the results of high filtration efficiency because of the small diameter of the CNTs in our filters. However, the relatively low pressure drop values were, at first, surprising. Figure 4.9 shows that our material's filtration efficiency versus pressure drop is comparable to other nano-sized fiber filters. On the other hand, the CNT sheet filter's pressure drop is in the same range as electrospun fiber filters even though CNTs within our filters have fiber diameters that are 3-10 times smaller than most electrospun fibers. There are several reasons that help explain this result. One of the reasons could be the fiber size distribution. SEM and TEM images show that CNT diameters in the CNT sheets are 25-40 nm, while electrospun fiber mats generally have a much wider diameter distribution. Another

explanation can be drawn from Equation 2, that pressure drop is related to fiber diameter, filter thickness, face velocity and fiber packing density. Due to the nature of the electrospinning process, the nanofibers are layered in direct contact with one another in a random fashion. In the CNT sheets, the packing density of the CNTs is extremely low. The calculated packing density (α) was 6.5×10^{-4} , which is lower than other nanofiber structures. We hypothesize that the very low packing density of the CNT sheets is one of the reasons for the high efficiency with relatively low pressure drop. This hypothesis is supported by work of Leung et al. that showed that increasing the fiber packing density of electrospun mats created an increase in pressure drop without significantly changing the filtration efficiency. Equation 2 was used to compare the experimental results of Δp with the theoretical. Those results are shown in Table 4.1. The experimental values were generated by subtracting the pressure drop of the control sample from the pressure drop of the polypropylene-CNT layered filter structures. While the 1-layer and 7-layer values showed less agreement, the 2-layer and 3-layer CNT structures showed some agreement with the calculated values.

Table 4.1 Experimental and calculated pressure drop values for the CNT sheet filters

Sample	Experimental Δp (Pa)	Calculated Δp (Pa)
1-Layer	32	53
2-Layer	82	107
2 Layer Cross-Ply	96	107
3-Layer	140	160
3-Layer Cross-Ply	147	160
7-Layer	642	373

The filtration efficiency of the studied system was also modeled using equations (modified for slip-flow condition) that describe single fiber efficiency due to Brownian diffusion and direct interception, see for example calculations used for nanofiber filters in references^[12,13,112,184]. The filtration efficiency predictions were significantly different from the measured values and so were not included in this work. This discrepancy was mostly likely due to the flow regime of the gas flowing through the CNT sheets. This regime can be described by the Knudsen number (Kn_f) with $Kn_f = 2\lambda/d_f$ where λ is the mean free path of the gas. These classic models are valid when the gas flowing through the filter is in the continuum regime (Knudsen number ($Kn_f < 10^{-3}$) or slip-flow regime ($10^{-3} < Kn_f < 0.25$)^[12,187,188]. The Kn_f of the CNT filters was ~ 4 which is far into the transient regime between slip-flow and molecular flow ($Kn_f > 10$) and much higher than other nanofiber systems. Future work may focus on understanding this discrepancy so that the contributions from each filtration mechanism can be more clearly identified.

This study demonstrates that CNT sheet filters provide very good filtration efficiency at reasonable pressure drop values. This is true of many filtration structures. The CNT sheet filters may have other potential benefits due to the structure and carbon makeup. The basis weight of the 3-layer CNT sheet structure was 0.1 g/m^2 . Used in combination with very low basis weight meltblown fabrics, these structures could be incorporated into HEPA rated personal filtration masks that could be much lighter and thinner than current designs. Electrostatic charge is often added to commercial filters to increase their efficiency, but the applied charge can dissipate over time. The structures produced in this study were not charged; and, thus their filtration properties should remain stable, even when stored for long

periods of time. The CNTs used in this study are also stable in atmosphere at temperatures of at least 400 °C. These sheets could be integrated into glass based compact industrial filters that must operate at very high temperatures while efficiently removing nano-particles.

4.4 Conclusions

Aligned CNT sheets were integrated between micro-fiber polypropylene nonwoven fabrics to produce filters with HEPA level efficiency. The filters contained multiple CNT sheets that were either stacked parallel to the others or in a cross-ply configuration. The filtration efficiency was evaluated by using test particles with diameters of 0.01-0.3 μm . The pressure drop of test filters was measured at 10 cm/s face velocity. The filtration efficiency test results demonstrated that 3-layer CNTs cross-ply filter had the highest quality factor and met the HEPA filtration criteria. The results show that these novel CNT filters have filtration properties that are comparable to electrospun fabrics, making them a viable option for future filtration applications. Due to the continuous nature of the CNT sheet drawing, covering large areas of supporting fabrics very quickly may be possible in the future.

Acknowledgements

The authors acknowledge the Turkish Ministry of National Education for provision of a Ph.D. scholarship to Ozkan Yildiz, and Dr. Behnam Pourdeyhimi, (Associate Dean for Industry Research and Extension; William A. Klopman Distinguished Professor; NCRC Director) at NC State University for supplying the polypropylene nonwoven fabric. The authors also thank Kelly Stano and Hardik Bhanushali for thoughtful discussion.

Chaper 5 Multi-layer CNT Sheet – PET Nonwoven Fabric Structures for High- Performance Aerosol Filtration

Ozkan Yildiz¹, Karim Aly¹, Sheng-Chieh Chen², David Y. H. Pui² and Philip D. Bradford^{1*}

¹Department of Textile Engineering Chemistry and Science

North Carolina State University, Campus Box 8301, Raleigh, NC USA 27695

²Particle Technology Laboratory, Mechanical Engineering

University of Minnesota, Minneapolis, Minnesota, USA

Abstract

Nano-fiber fabrics provide greater filtration efficiency than conventional micro-fiber fabrics due to their higher surface area and smaller pore size. Carbon nanotubes (CNTs) are small diameter and high surface area, which makes them very attractive in the aerosol filtration area. In this study, CNT sheets, drawn from millimeter tall CNT arrays, were integrated between traditional micro-fiber fabrics to produce aerosol filters. To understand the contribution of CNT sheet and micro-fiber fabrics, multi-layer structured filter was designed by using CNT sheet and different porous nonwoven fabrics. The filtration performance of the novel structured filters showed that when the CNT sheet layers were separated from each other, the filtration efficiency increased over similar structures where the CNT layers were directly on top of each other. In addition, physical properties of the fabric significantly contribute filtration characteristics. The results demonstrated that the structure

utilizing three separated CNT layers and the low porosity base fabric structure provided 98.92 % filtration efficiency at 0.3 μm particle size at a 5 cm/s face velocity. The results suggested that this cost-effective novel filter design could be used as a promising material for future aerosol application.

5.1 Introduction

Fine particles, especially those with aerodynamic diameter less than 2.5 μm , are one of the most serious sources of air pollution due to rapid urbanization and industrialization. In order to prevent reduce the impacts of these fine particles to the environment and human bodies, air filtration technology has had greatest interest due to its low equipment cost, relatively low energy consumption, high performance and wide application areas^[3,4]. Fibrous filters have been most often used when particles 1 μm or smaller must be separated from a gas flow with high efficiency ($> 95\%$)^[67]. There is an enormous demand for even more particulate free air in various fields such as semiconductor manufacture, aerospace environments, pharmaceutical processing, bioengineering, and hospitals and airplane cabin air systems which has sparked immense interest in the development of high efficiency filters^[172].

Nano-fiber based aerosol filters can significantly improve the performance of an ordinary filter due to small fiber diameter and high surface area^[11]. In addition, when the fiber diameter is comparable to the mean free path of the air molecules (66 nm under normal conditions), the gas velocity is non-zero at the fiber surface due to slip effect. Therefore, the

drag force because of the airflow on the nano-fibers is greatly reduced. This leads to a lower pressure drop caused by nano-fiber filter when compared to microfiber filter which has the same filtration efficiency^[67].

A variety of methods have been developed to fabricate nanofiber-based aerosol filters to capture fine particles, including melt-blown, phase separation, template synthesis and plasma treatment. However, most of these methods are unsuitable for practical applications and they suffer from high pressure drop and low filtration efficiency^[189]. Electrospinning is one of the most promising technologies for preparation nano and submicron fiber, lightweight, low basis weight HEPA filters. By employing electrospinning process with using several different polymers, polymer nano-fibrous filters have attracted due to their high surface area, high open porosity, interconnected porous structure. However, minimizing the high pressure drop they produce and the limitation for decreasing fiber diameter to less than 100 nm are mainly the biggest challenges of this method^[172,173,190].

CNTs have attracted much interest in the area of aerosol filtration because of their small diameter and high surface area. Using CNTs, especially with diameters less than 10 nm, the airflow will be in free molecular flow (FMF) regime which has thus far been impossible to reach by traditional fiber processing methods^[67,190]. Therefore, CNTs were deposited onto the nonwoven fabric surfaces in order to create tortuous pathway, increase surface area and also increase the effect of diffusion mechanism^[11]. In most studies, CNTs were coated onto the fibers' surfaces or fabric surface^[14,89]. In another method, CNTs were dispersed in solution, and then vacuum filtered to form a thin and continuous layer onto the

cellulose filter^[90]. However, CNTs agglomerate and bundle together after liquid dries, thus reducing their surface area and increase the pressure drop dramatically. In all these studies, CNTs have short length and they can be released during continuous airflow, which can cause more dramatic health issue problems^[174,175]. Therefore, in this study, the CNTs were both millimeter long and were integrated in between traditional nonwoven fabrics, ensuring that CNTs would act only as a filtration element.

Vertically aligned CNT arrays, produced from chemical vapor deposition (CVD), have several fascinating characters that make them very attractive in the aerosol filtration area. Using the right growth conditions, the CNTs can be drawn off in continuous sheets using tweezers, which exhibit preferential alignment of the CNTs. These sheets are extremely thin, highly porous, semi-transparent and have an interconnected pore structure. The aerosol filtration characteristics of aligned CNT sheets were first studied in the previous chapter, and the results showed the CNT sheet significantly improved the filtration efficiency at reasonable pressure drop^[11]. In order to understand the substrate and CNT sheet contribution to filtration characteristics and to develop high-performance filtration membranes, different porous nonwoven fabrics and different multi-layer CNT-nonwoven hybrid structure were designed.

The objective of this study was to fabricate multi-layer filter membranes by drawing aligned CNT sheets and embedding them between nonwoven fabrics using calendaring. To understand the effect of fabric porosity and CNT sheet design in the filter membrane, the combined and separated CNTs structure filters were prepared with using two different types

of porous fabrics and with an increasing number of CNT sheet layers. The filtration characteristics of the multi-layered filters were obtained and the results were evaluated in terms of collection efficiency and pressure drop, and then compared between each other.

5.2 Materials and Methods

5.2.1 Materials and Instrumentation

Two types of base nonwoven fabrics were used in this study. The high porosity polyester (PET) melt-blown fabric was provided from the General Nonwoven Factory from Gaziantep in Turkey. The low porosity PET melt blown fabric was provided from the Nonwovens Institute at North Carolina State University. These fabrics were used as the face sheets for the laminated filter structure. The high and low porosity fabrics' basis weights were 12 g/m² and 50 g/m² in respectively. Iron II chloride (FeCl₂) was purchased from Fisher Scientific. Scanning electron microscopy (SEM) data was collected using a FEI XHR-Verios 460L Field Emission SEM with a beam voltage of 1.0 kV. Transmission electron microscopy (TEM) was used (Cold Field Emission TEM, Model Hitachi HF2000) to determine the CNT diameter range. The filtration efficiency and pressure drop data was collected using an TSI Automated Filter Tester 3776.

5.2.2 CNT Array Synthesis and CNT Sheet Analysis

Vertically aligned multi-walled carbon nanotubes (MWCNT), with individual CNT diameters 30-50 nm and length of 1 mm, were grown in a tube furnace via a modified version of the chlorine mediated chemical vapor deposition route. The aligned CNT arrays were synthesized on a quartz substrate at 760 °C and 3 Torr with Iron II chloride (anhydrous

99.5% VWR) as a catalyst and acetylene as the carbon precursors. The reaction took place for 20 min under the flow of acetylene (600 sccm), argon (395 sccm) and chlorine (5 sccm). A detailed procedure of the growth method was explained in our previous work^[190].

The CNT arrays were highly drawable in nature, as seen in Figure 5.1 a. The aligned CNT sheets were formed by dragging a razor blade across one edge of the CNT array, and then pulled with tweezers. The thickness of the CNT sheets was approximated by stacking many layers of CNT sheets around the two rotating parallel glass rods, and then it was measured by using optical microscope. Then the thickness was divided by number of layers and it gave us the average thickness of each CNTs sheet. The average thickness of CNT sheet was determined to be 20-25 μm which corresponded to the individual sheet cross sectional thickness, as seen in Figure 5.1 b. The basis weight of both CNT sheets was measured by winding multiple layers of the sheet, measuring the total mass, and then dividing by the total area of the wound sheet. The top surface and typical spacing between CNTs within the sheet are shown in Figure 5.1 c. The diameter of CNTs was determined from TEM image as seen in Figure 5.1 d.

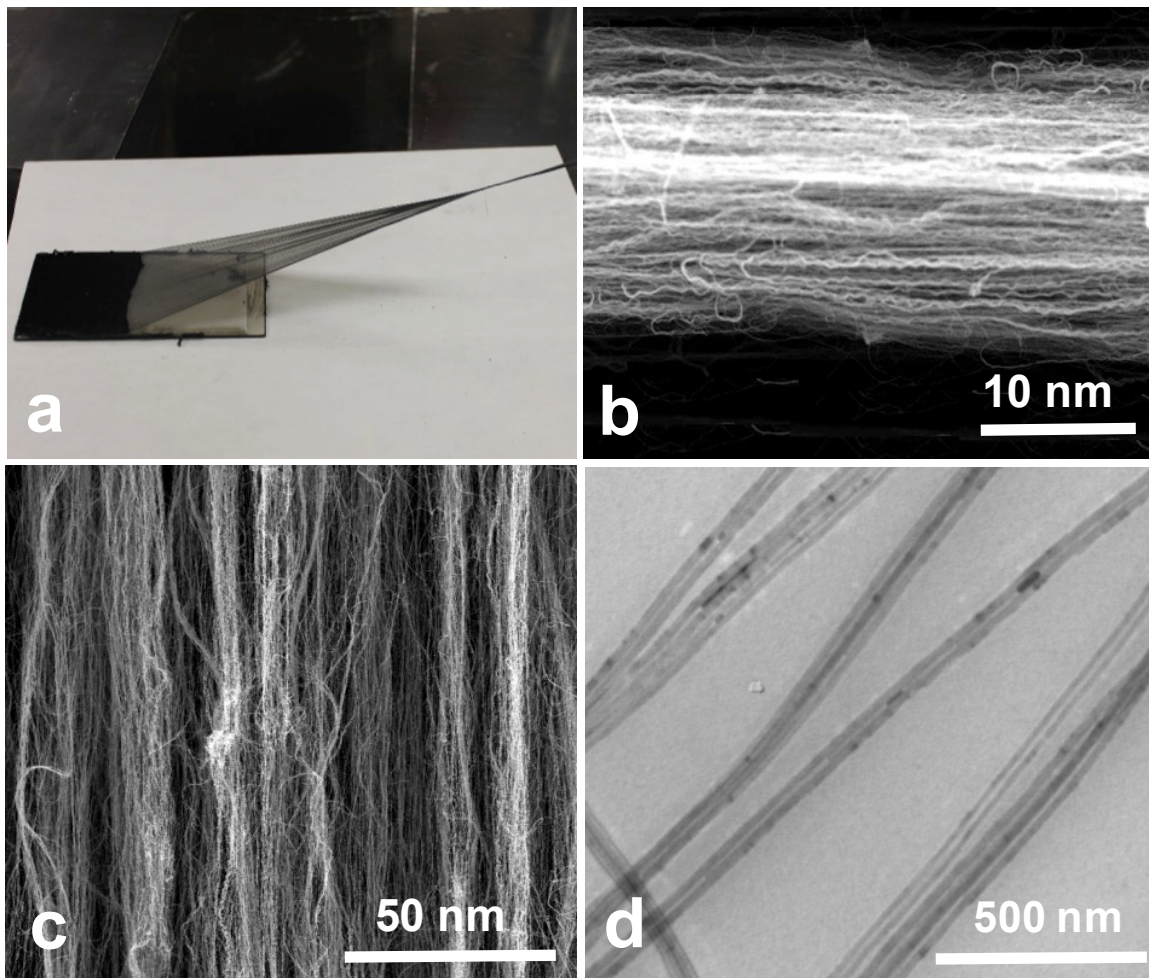


Figure 5.1 a) Aligned CNT sheet was drawn from the array using tweezers, b) the cross-section of the CNT sheet showing the approximate thickness, c) high magnification SEM image of single layer CNT sheet, d) TEM image of CNTs from the sheet.

5.2.3 Preparation of CNT Sheet Aerosol Filter Structure

Due to CNT sheets very small thickness and density, they are very fragile and need to be supported in their application to aerosol filtration. In order to utilize them in a filter structure,

they were placed between the polyester (PET) meltblown fabrics to provide mechanical and structural support. The PET meltblown nonwoven fabric served as a prefilter and also to confine the CNTs. Because of the small density and thickness of the CNT sheet, the radial force from the winding process may compact the sheet structure forming more bundles of CNTs when multiple layers of CNT sheets are layered on top of each other. Therefore, in order to understand this effect, two different structures were prepared using CNT sheets; one where the CNT sheet layers were combined and one where the CNT sheet layers were separated by additional layers of the PET fabric. The process of the preparation of CNT – PET meltblown air filter samples consisted of several steps, which are shown, in Figure 5.2 a-d. For the samples with separated CNT layers, 2 pieces of 10 cm x 15 cm PET meltblown nonwoven fabrics fixed onto the two rotating glass rods. After a 6 cm wide CNT sheet was drawn onto the fabric, another PET nonwoven fabric was wound onto the structure. This process was repeated till three CNT sheets were fixed into the structure. Finally one more PET fabric was wound onto the structure (Fabric – CNT – Fabric – CNT – Fabric – CNT – Fabric). To produce the samples that had the combined CNT layers, three CNT sheet layers were wound onto two PET fabric layers, and then another two layers of PET fabric was wound on top of the CNTs (Fabric – Fabric – CNT – CNT – CNT – Fabric – Fabric). After removing the sandwich structure from the glass rods, the sandwich structures were placed between aluminum plates that contained a square hole cut out with dimensions of 3.8 cm × 3.8 cm. The assembly was placed between hot press platens and left under load at 200 °C for 10 minutes. The edges of the PET nonwoven fabrics were thermally bonded to create a robust edge. All the PET fibers under the aluminum plates were calendered together while

the middle area of the aluminum plates was not exposed the same heat or pressure, leaving a pristine multi-layer sandwich structure for filtration evaluation.

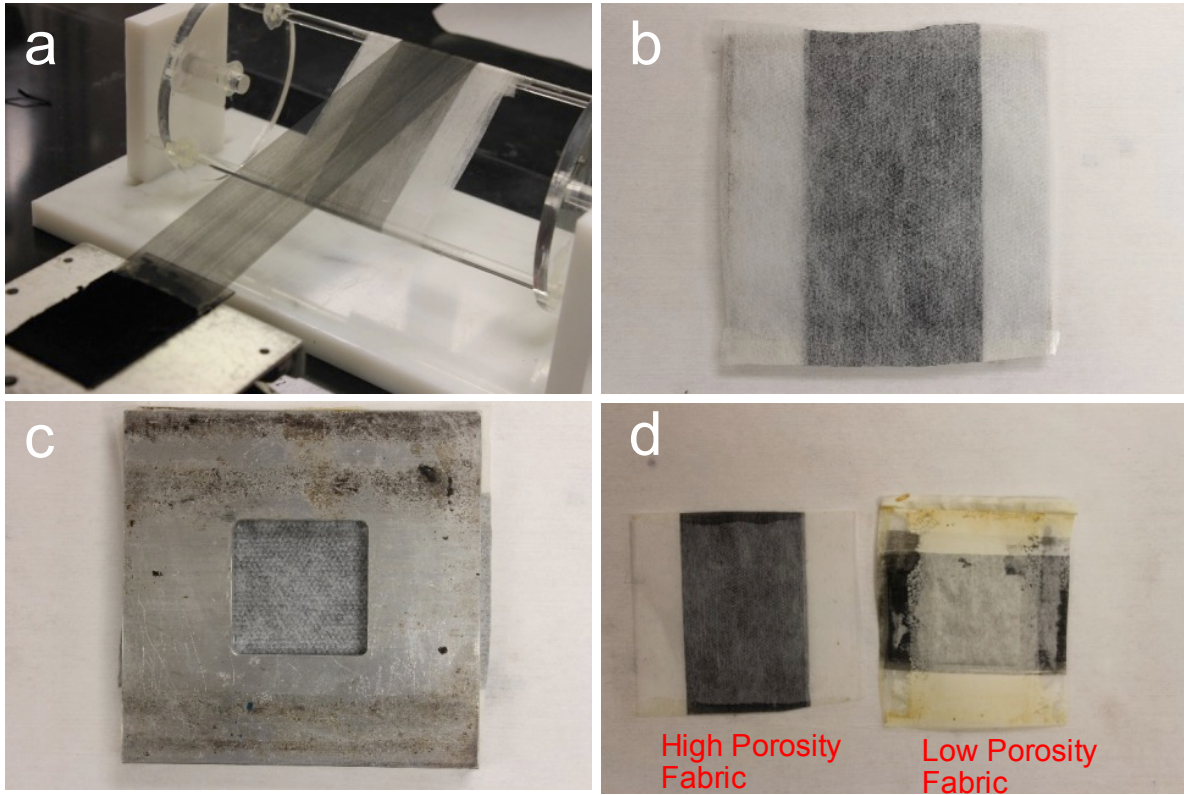


Figure 5.2 Preparing filters by (a) winding CNT sheets onto the PET highly porous fabric, (b) placing CNT sheet – PET multi-layered fabric onto a calendaring plate with hole in the middle, (c) covering with a second calendaring plate and (d) the final calendared fabric with pristine multi-layered structure in which the middle square section was not exposed to heat or pressure.

5.2.4 Filtration Evaluation

The filtration efficiency test has been performed using 3-20 nm silver particles, 20-800 nm KCl particles. Silver particles were generated in an electric furnace by heating a pure silver powder source. Then silver particles were classified in a nano-differential mobility analyzer (nano-DMA) and neutralized before being fed to challenge the filters. KCl particles were generated by a collision type atomizer and classified by a DMA. Then all the particles were fed into the filter holder with an effective area 6.45 cm². An ultrafine condensation particle counter (UCPC) was used to measure the number of particles in the upstream and downstream flow after the particle concentrations were stable. The filter testing system has been detailed in different work^[13]. The collection efficiency was calculated using the following equation:

$$E = 1 - \frac{N_{down}}{N_{up}} = 1 - P \quad \text{Equation 31}$$

where, E is the fractional efficiency of a specific size of the particles, N_{down} and N_{up} are number of particles on the downstream and upstream sides, and P is the fraction of penetration.

5.3 Results and Discussion

Vertically aligned CNT arrays were extremely spinnable in nature, and it can be drawn quickly at speeds up to 0.5 m/s. CNT arrays used in this study had dimensions of 60 mm × 100 mm and their dimensions limited only by the dimensions of CVD tube furnace. A

single CNT sheet layer had an average basis weight of 0.1 g/m^2 , which was approximately 120 times and 500 times lower than high and low porosity fabrics, respectively. Figure 5.3 shows the typical morphology of high and low porosity fabrics and aligned CNT sheet structure. As seen in Figure 5.3 a-b, the highly porous PET nonwoven fabric's fibers range from $4\text{-}6 \mu\text{m}$ in diameter. Figure 5.3 c-d shows the low porosity PET nonwoven fabric which the fibers range from $2\text{-}3 \mu\text{m}$ in diameter. The SEM images of 1-layer CNT sheet structure are shown in Figure 5.3 e-f. As seen in Figure 5.3 e, the CNTs appear to be parallel to each other when they are viewed at lower magnifications. However, at higher magnification, more of the inherent waviness and entanglements are visible. It is difficult to determine the average pore sizes of the CNT sheet due to the extremely low density of the CNT sheets, but there appeared to be a wide range of spacing. The bulk density of our CNT sheet structure was approximately 0.0054 g/cm^3 . The pore volume of the CNT sheets was 99.9% based on approximate CNT density of 2.0 g/cm^3 .

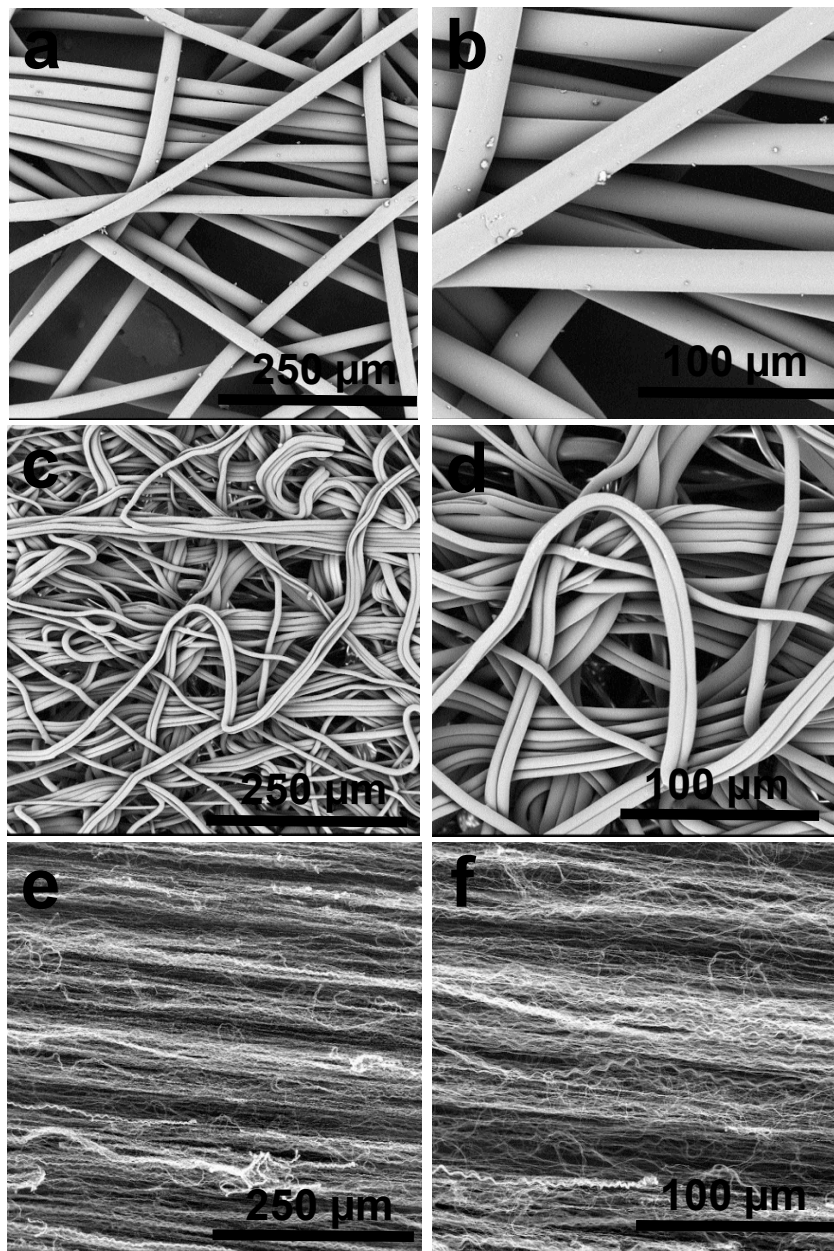


Figure 5.3 SEM images at two different magnifications of (a and b) porous PET melt blown fabric, (c and d) low porosity PET melt blown fabric, and (e and f) CNT sheet structure.

As-drawn aligned CNT sheet structures are easily deformed through application of any force, so the PET melt blown nonwoven fabrics were used as a based fabric to provide mechanical and structural support for the CNT sheets. Two different pore size melt blown fabrics were chosen, because their pore sizes were small enough to trap CNTs, encapsulating them in the fabric. However, their pore size, pore size distribution and fiber diameters are different, which gave different filtration efficiency and pressure drop.

Figure 5.4 shows the filtration performance of the two different multi-layer structures which were prepared from different PET nonwoven fabrics, in terms of the particle penetration percentage, for the 3–800 nm particle size range tested. Figure 5.4 a shows data for the high porosity control sample and multi-layer CNT samples where all the CNT sheets are stacked in the same direction. The control sample was inefficient, capturing only 7.66% of the particles at the 0.3 μm particle size. Adding a single layer of the CNT sheet dramatically increased the filtration efficiency to 53.96% at the 0.3 μm particle size. Adding additional layers further increased the efficiency. The 3-combined layer CNT fabric increased the filtration efficiency to 70.38% at the 0.3 μm particle size while the 3-separated layer CNT structure increased the filtration efficiency to 79.15% at the 0.3 μm particle size. Figure 5.4 b shows data for the low porosity PET melt blown control sample and multi-layer CNT samples. The standard deviation of filtration efficiency for each particle sizes is less than 0.001, so it cannot be seen in the Figure 5.4.

There are mainly three different mechanisms by which an aerosol particle can deposit on aerosol filter. These are Brownian diffusion, interception, and inertial impaction^[11,14,76].

The effectiveness of the particle capturing for each of these mechanisms depends on particle size, face velocity and fiber diameter. When particles pass through a fibrous filter, the filter captures them through a combination of these three mechanisms. However, different mechanisms dominate for different particle size ranges and for one particle size, none of these mechanisms are dominant and shows the lowest filtration efficiency which is called most penetration particle size (MPPS), which is typically around 0.3 μm or smaller for neutral filters. The MPPS for the filters containing the CNT sheets was around 0.1-0.2 μm which is lower than the control sample filters. Other studies have also shown that nanofiber coatings on microfiber substrates have MPPS values lower than the conventional microfiber filters^[12]. With the CNT diameter remaining constant, when number of CNT layers increased, filtration efficiency also increased due to the increase in the CNT sheet solidity and thickness. In addition, when the CNT sheet layers were separated, the filtration efficiency also increased. It is thought that when all CNT sheets are stack together, it compacts the CNT sheets increasing the packing density and increasing the bundles size (effective fiber diameter). Thus, when CNT sheets were separated, it could not form these bundlers between CNT layers.

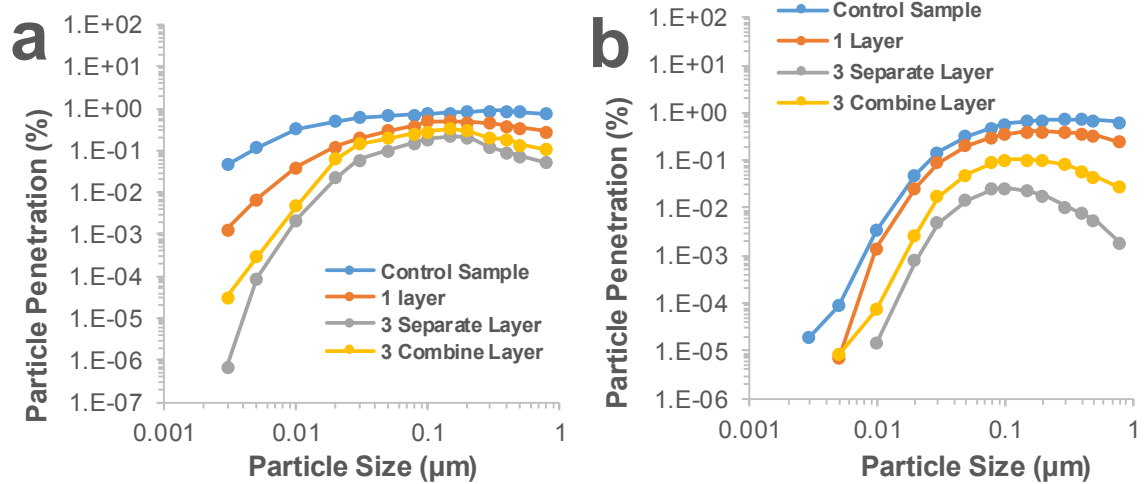


Figure 5.4 Filtration performance of a) CNT sheet – high porosity PET melt blown multi-layer filter, b) CNT sheet – low porosity PET melt blown multi-layer filter at face velocity of 5 cm/s.

Figure 5.5 shows the filtration performance comparison between 3-separated and 3-combined layer CNT structure with using high and low porosity fabric. The 3-separated layer CNT samples greatly improved the filtration efficiency more than 3-combined layer CNT samples. It can be explained that the radial force from the winding process and also the airflow during the testing compacted the sheet structure forming more bundles of CNTs, as opposed the individualized CNTs. The separating each CNT sheet layer prohibited forming more bundles, which increase the filtration efficiency. In addition, fabric porosity affected the filtration characteristics. The results showed that the CNTs having smaller distance to span, so they are more stable during handling and airflow in the low porosity fabric. Thus, low porosity 3-separated layer CNT fabric gave the highest filtration efficiency as seen in Figure 5.5.

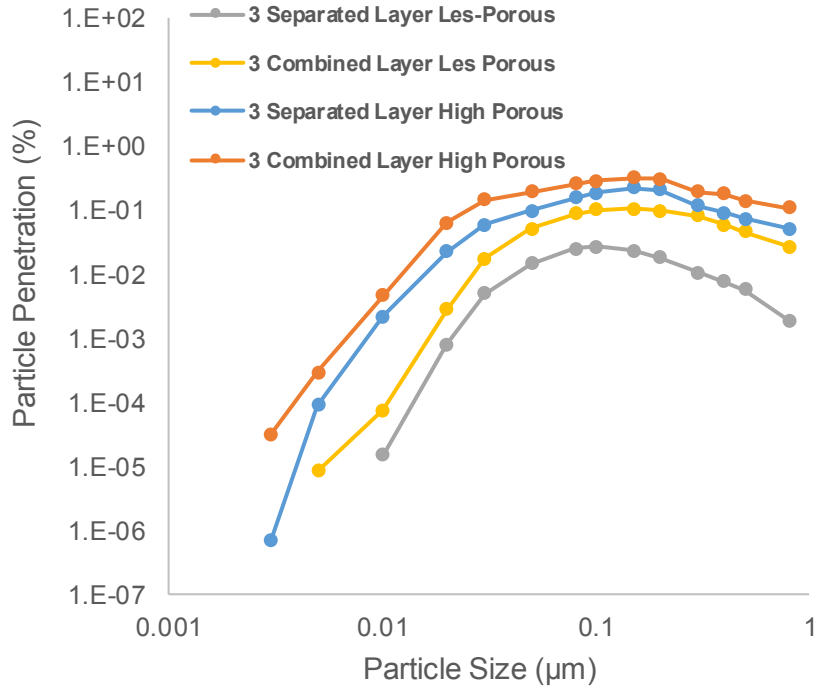


Figure 5.5 The Filtration performance of filters consisting of 3-separated CNT high porosity, 3-separated CNT low porosity, 3-combined CNT high porosity and 3-combined CNT low porosity multi-layer structure at a face velocity of 5 cm/s

Another important parameter for aerosol filtration is pressure drop. The average pressure drop over the filter is directly proportional to energy consumption, so low pressure drop is always a desired filter property. The pressure drop across the filter is caused by the combined effects of the resistance each fiber to air during the airflow. Therefore, the flow regime of the gas around the fibers significantly affect pressure drop of the filter sample. Knudsen number is dimensionless number that characterizes the flow regime of the gas around the fiber^[67].

$$Kn = \frac{2\lambda}{d_f}$$

Equation 32

where λ is the mean free path of air molecules (around 66 nm under normal temperature and pressure) and d_f is the diameter of the fiber. The flow regime can be categorized into four different types, which are continuum flow regime, slip flow regime, transition flow regime, and free molecular flow regime. When the fiber diameter smaller than 132 μm , the slip flow regime starts and the pressure drop decreases due to gas slip at fiber surface. Pressure drop is also affected by face velocity, the solidity, fiber diameter, and thickness of filter media^[11].

Figure 5.6 shows the pressure drop of the two different multi-layer structures, which were prepared from different PET nonwoven fabrics. Figure 5.6 a shows the high porosity fabric CNTs hybrid fabric's pressure drop results. The control sample gave a 2.16 Pa pressure drop. After depositing a single layer sheet of CNTs within the PET melt blown fabric, the pressure drop increased to 13.7 Pa. 3-combined CNT sheet gave a 33.1 Pa pressure drop while 3-separated-layer CNT sheet gave a 49.8 Pa pressure drop. This trend was the same for low porosity fabric and 3-combined CNT sheet gave a 77.8 Pa pressure drop while 3-separated-layer CNT sheet gave a 105.4 Pa pressure drop. The pressure drops for all samples were within a reasonable range for filtration products. The results showed that the separated structures gave higher pressure drop than the combined structures, because when all CNTs stacked together, it compacts the CNT sheets increasing the bundles size and increasing the pore sizes, which cause less pressure drop. On the other hand, when CNT sheets separated each other, it decreased the number of bundling and it does not affect the pore sizes, which cause higher pressure drop. The results also showed that when the fabric pore sizes decrease, the pressure drop is also increases.

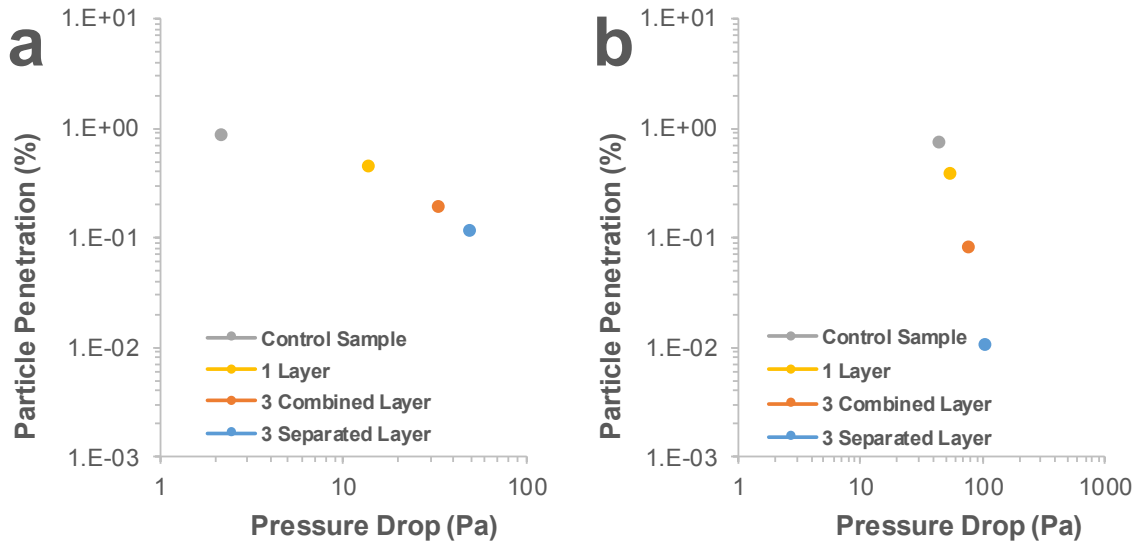


Figure 5.6 Particle penetration percentage of a) high porosity CNT sheet multi-layer filter, b) low porosity CNT sheet multi-layer filter as a function of pressure drop at 0.3 μm particle size and 5 cm/s face velocity.

The best filter is the one that gives the highest filtration efficiency with the lowest pressure drop. Filter quality factor (QF) is a parameter used to compare filter types and filters of varying thickness, and is a ratio between filtration efficiency and pressure drop^[190].

$$QF = \frac{-\ln P}{\Delta P} \quad \text{Equation 33}$$

where P is the filter penetration and Δp is the pressure drop. The most efficient filter is the one that has the greater value of QF. Figure 5.7 shows the comparison of the QF between the

high porosity multi-layer CNT hybrid fabrics and the low porosity multi-layer CNT hybrid fabrics. The QF of the 3-separated layer CNT sheet low porosity PET nonwoven fabric was higher because their filtration efficiency increases were more than the pressure drop increases.

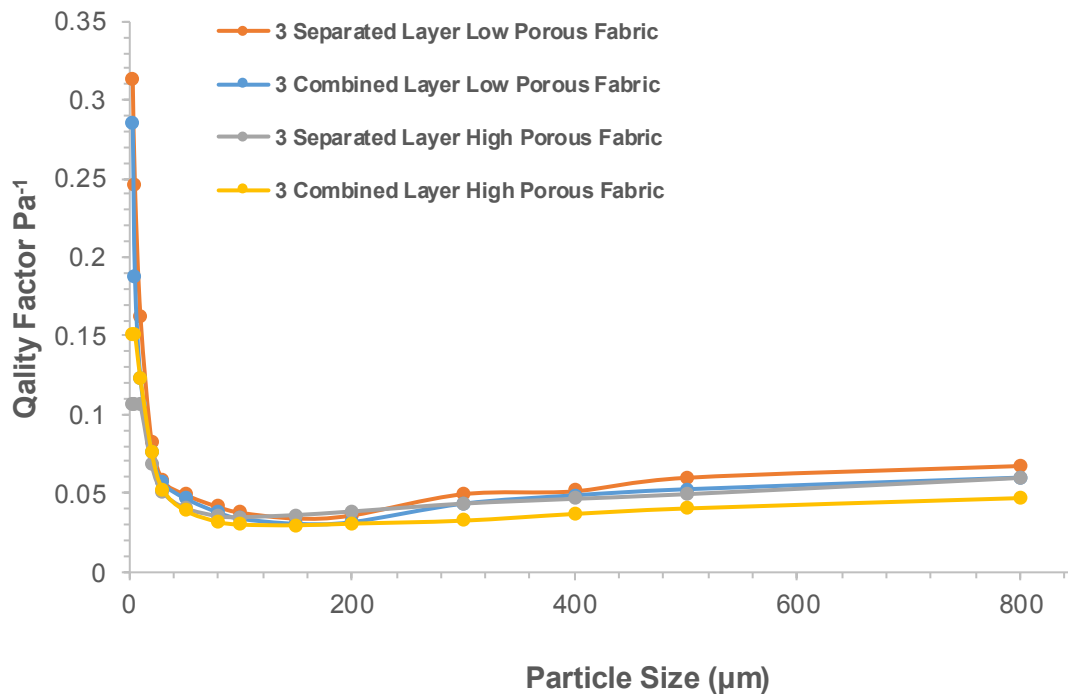


Figure 5.7 Quality factor as a function of particle sizes, ranging from 3-800 nm, at a 5 cm/s face velocity.

This study demonstrates that CNT sheet provides very good filtration efficiency at reasonable pressure drops when the nonwoven fabric has different pore structures. This is because of aligned CNT sheets' unique properties. The first, the Kn_f of the CNT filters was

around 4-6 which is in high transition flow regime. The experimental results showed that the penetration and the pressure drop in the filter were reduced significantly by an increase in the Knudsen number. The calculated packing density of the CNT sheets was 7.9×10^{-4} which is lower than that of other nanofiber filters. Thus, the low packing density is one of the reasons for high efficiency and low pressure drop, because Leung et al.'s study proved that increasing the fiber packing density of electrospun mats created an increase in pressure drop without significantly changing the filtration efficiency. CNTs diameter range 30-50 nm which is 3-10 times smaller than the most electrospun nanofibers. However, due to CNT sheets very small thickness and density, they can easily bundle which is directly affect the filtration efficiency. In order to take advantage of this unique CNT sheet structure and improve the filtration efficiency, fabricating multi-layer structured CNT sheet membrane is simple and economical solution^[11].

5.4 Conclusion

Fabricating novel multi-layer structured filter using CNT sheets and PET melt blown nonwoven fabrics exhibited improved filtration efficiency. The multi-layer structured CNTs filters prepared different porous PET melt blown nonwoven fabrics. The filtration efficiency was evaluated by using test particles with diameters of 3–800 nm. The pressure drop of test filters was measured at 5 cm/s face velocity. The filtration efficiency test results demonstrated that 3-separated layer CNTs low porosity multi-layer filter had the highest filtration efficiency and quality factor. The results showed that separated-CNT structure

improved filtration performance because of less bundling, small packing density and high surface area. Therefore, this simple solution improved the filtration performance compared to combined-CNT structure. In addition, the architecture of CNT sheet is important and that further improvements could be made through further engineering the multi-layered fabric structure.

Chaper 6 High Performance Carbon Nanotube – Polymer Nanofiber Hybrid Fabrics

*Ozkan Yildiz, Kelly Stano, Shaghayegh Faraji, Corinne Stone, Colin Willis, Xiangwu Zhang, Jesse S. Jur, and Philip D. Bradford**

Ozkan Yildiz, Kelly Stano, Shaghayegh Faraji, Prof. Xiangwu Zhang, Prof. Jesse S. Jur, and Prof. Philip D. Bradford

Department of Textile Engineering Chemistry and Science, North Carolina State University, Campus Box 8301, Raleigh, NC USA 27695

Dr. Corinne Stone, Dr. Colin Willis

Defence Science and Technology Laboratory, Salisbury, Wiltshire SP4 0JQ, UK

Abstract

Stable hybrid fabrics containing both polymer nanofibers and carbon nanotubes (CNTs) are highly desirable but very challenging to produce. Here, we report the first instance of such a hybrid fabric, which can be easily tailored to contain 0-100% millimeter long CNTs. The novel CNT – polymer hybrid nonwoven fabrics are created by simultaneously electrospinning polyethylene oxide (PEO) nanofibers onto aligned CNT sheets which are drawn and collected on a grounded, rotating mandrel. Due to the unique properties of the CNTs, the hybrids show very high tensile strength, very small pore size, high specific surface area and electrical conductivity. In order to further examine the hybrid fabric properties, they

are consolidated under pressure, and also calendared at 70 °C. After calendaring, the fabric's strength increases by an order of magnitude due to increased interactions and intermingling with the CNTs. The hybrids are highly efficient as aerosol filters; consolidated hybrid fabrics with a thickness of 20 microns and areal density of only 8 g/m² exhibit ultra-low particulate (ULPA) filter performance. The flexibility of this nanofabrication method allows for the use of many different polymer systems which provides the opportunity for engineering a wide range of hybrid materials with desired functionalities.

Key Words: Hybrid fabric, carbon nanotube sheets, mechanical properties, aerosol filtration, multi-functional

6.1 Introduction

Due to their small fiber diameter, high specific surface area, high porosity and small pore sizes, polymer nanofiber nonwovens produced via electrospinning have gained attention in a broad range of applications such as aerosol and liquid filtration^[80,81,191,192], protective garments^[193], barrier membranes^[194], tissue scaffolds^[26], catalyst support structures, and others^[18,86,87,121,195]. These applications require well defined nonwoven properties such as pore diameters, internal surface area, permeability, as well as high mechanical strength^[86,87]. However, nanofiber nonwovens typically exhibit low individual fiber and web mechanical strength compared to conventional nonwovens due to their highly porous structure, intrinsically low or, random fiber orientation, weak bonding between nanofibers and low polymer orientation within individual nanofibers. These structural parameters hinder their

performance and use in many applications^[18,87,129,196]. The result is that nanofiber nonwovens are supported and adhered to a base fabric composed of macroscopic fibers.

To avoid the use of a base fabric, previous studies have reported several methods to improve nanofiber mechanical strength^[18,87,197]. These routes include: changing the nonwoven nanofiber mat into self-bundled yarns^[18,19], applying surface modification or post treatments such as stretching, twisting, or annealing^[20–22,198,199], and reinforcing the single nanofiber strength by adding carbon nanotubes (CNTs)^[18,19,23], layered silicates^[24] or graphite nanoplatelets^[25] into the polymer spinning solution. Many of these approaches either change the highly porous nature of nanofiber nonwovens or complicate the electrospinning process. Among these methods however, the addition of CNTs to polymer electrospun fibers has attracted many researchers due to their high mechanical, electrical and multifunctional properties and strong interactions with electrospun fiber matrices resulting in large interfacial area^[26–28,126,130,136,200]. However, several factors significantly influence the final nanofiber nonwovens properties, such as CNT dispersion, orientation, alignment, volume (or weight) content, and interfacial adhesion with polymer^[27,29,30,132–134,201]. Above the CNT electrical percolation threshold, additional CNTs can cause a bead structure formation which negatively affects the mechanical properties of the nanofiber nonwovens^[27,28]. Since CNTs usually exist as stable bundles and their dispersion and alignment in polymer matrices are very difficult to achieve due to strong van der Waals interactions among CNTs, several different processing methods have to be applied to disperse CNTs such as high power ultrasonic mixers, functionalization or the addition of coupling agents or surfactants^[27,29,133–135,202,203]. Another disadvantage of using this method is the limitation of the CNTs content in

polymer solutions. When the CNT weight or volume fraction is higher than approximately 1-5% in polymer solution, the mechanical properties of nanofiber nonwovens decrease and become lower than pure polymer samples^[27,126,135,137-139]. In order to address these limitations and to improve final nanofiber nonwoven properties, new processing techniques are needed where CNTs can be utilized in high concentrations, dispersed homogenously and aligned in preferential directions.

Continuous CNT sheets are excellent candidates for producing nanofiber nonwoven fabrics due to their high surface area, alignment, electrical conductivity and mechanical properties^[11,56,204]. In this work, a novel CNT – polymer hybrid nonwoven fabric is created by simultaneously electrospinning PEO nanofibers onto aligned CNT sheets, which are drawn and collected on a grounded, rotating mandrel. PEO polymer solution was chosen for electrospinning because it is easily electrospun, and melts at low temperature. However any polymer that can be electrospun should be able to be integrated with the CNT webs to form the same hybrid fabrics. As a result of this novel hybridization method, continuous electrospun polymer nanofibers are fully integrated among the aligned CNT sheets (diameter ~30 nm, aspect ratio ~50,000) trapping them inside the fabrics. Due to the unique properties of CNTs, the hybrid fabrics show very high strength, small pore size, high specific surface area and electrical conductivity. This novel process demonstrates a new technology which overcomes the numerous physical and mechanical limitations of traditional electrospun nonwovens, and is promising for some of the most demanding nanofiber applications. In this communication, the mechanical, electrical, aerosol filtration, permeability, and barrier properties of the novel hybrid fabrics are evaluated.

6.2 Materials and Methods

6.2.1 CNT Synthesis

Vertically aligned multi-walled carbon nanotubes (MWCNT) were grown by chemical vapor deposition (CVD) on a quartz substrate using iron II chloride (FeCl_2) as the catalyst^[11]. First, iron chloride and substrate were placed inside a quartz tube. Then this inner tube was loaded into outer quartz tube of a horizontal tube furnace. The chamber was sealed and pumped to less than 10 mTorr, and then the chamber was heated to 760°C. When the chamber's temperature reached 760°C, the growth gasses, acetylene (600 sccm), argon (395 sccm) and chlorine (5 sccm), were introduced into the chamber. The reaction took place 20 min, after which time the chamber was returned to starting conditions (ambient temperature and atmospheric pressure).

6.2.2 Electrospinning Process and Characterization

PEO of M_w 600,000 was purchased from Sigma Aldrich. A 5% weight fraction of PEO solution was prepared by mixing PEO in water and then stirring for 1 day. When PEO was completely dissolved in water, the polymer solution was loaded into a 10 mL syringe with luer-lock connection and used in conjunction with a 1.27 cm, 22 gauge blunt tip needle. The electrospinning apparatus included a syringe pump from New Era Pump Systems (model NE-300), which operated at a flow rate of 1 mL/h. The high voltage power supply was from Gamma (High Voltage model ES40P-20W/DAM). The operating voltage varied from 10 to 15 kV and the distance between the collector and needle was 15 cm. The mandrel served as one of the electrodes in the electrospinning process and the mandrel was rotated by a

Regulated DC Power Supply (model DIGI 360). Different CNT weight fraction samples were produced by changing the winding speed during electrospinning. The surface morphology of CNT – polymer hybrid nonwoven fabrics were examined using a FEI XHR-Verios 460L Field Emission SEM with a beam voltage of 1.0 kV. All samples were imaged as-prepared without sputter coating.

Once the samples were prepared, two additional processing steps were completed to understand the effect of hybrid fabric structure on the properties. The first was to consolidate the fabric under 2 MPa of pressure without heat treatment for 5 min. The second was to calender the samples at 70 °C and 2 MPa pressure for 5 min.

6.2.3 Physical Testing

In order to understand the effect of super aligned CNTs on the physical properties of hybrid fabrics, their mechanical and electrical conductivity properties were evaluated. Samples with dimensions of 40 mm x 4 mm were cut along the longitudinal CNT direction by sharp blade without damaging hybrid fabric. The thickness of the samples was measured by micrometer. Tensile strength of the samples was tested using a Shimadzu EZ-S instrument with a 100 N load cell. Before testing, samples were mounted to paper tabs with tape on both sides to prevent slipping and reduce stress concentration at the grips. The gauge length of the tensile hybrid samples was 20 mm and testing speed was 0.5 mm/min. Electrospun fabric strength is sometimes calculated from fiber cross sectional area only (based on the mass of sample and density of the fibers) which gives inflated strength values. In this work, engineering stress

was determined by dividing the load on the fabric by the fabric cross sectional area calculated using the measured fabric thickness.

A four probe resistance measurement system was used to measure electrical properties of the samples. Samples with dimensions of 0.5 cm x 4 cm were placed onto a glass plate with four parallel gold electrodes across it. To ensure good contact between the sample and the gold electrodes, a square shaped piece of glass and a 500 g weight were placed on top of the samples during the measurements.

6.2.4 Aerosol Filtration Testing

The filtration properties of the hybrid fabrics were tested using a TSI Model 3160 Automated Filter Tester. The filtration efficiency of the control sample (eight layers of PEO electrospun fabric that was produced at lower mandrel speed) and seven layer hybrid fabrics (CNT weight fraction of 15%, 30% and 60%) were evaluated at 15 cm/s face velocity. DOP (dioctyl phthalate) particles with diameters between 0.010 and 0.3 microns were generated by a collision type atomizer and evaporated through a membrane dryer, and then neutralized by a Kr-85 radioactive source. The neutralized DOP aerosol particles were fed into the filter holder with an effective area of 6.45 cm² and their number concentrations measured upstream and downstream of the hybrid fabric by using two condensation particle counters (CPCs, TSI, Model 3760A). The collection efficiency was calculated using the following equation:

$$E = 1 - \frac{C_{down}}{C_{up}} = 1 - P \quad \text{Equation 34}$$

where, E is the fractional efficiency of a specific size of DOP particles, C_{down} and C_{up} are the number concentration of particles on the downstream and upstream sides, and P is the particle penetration fraction.

6.2.5 Plasma Functionalization

In order to make oleophobic polymer-CNT hybrid fabrics, a low surface energy chemical, PFAC8 ($C_8F_{17}CH_2CH_2OCOCH=CH_2$, Fluorochem, Derbyshire, UK) was deposited onto the CNT-polymer hybrid fabrics by using pulsed plasma polymerization. The treatment were carried out in a inductively coupled glass cylindrical glow discharge reactor, (10 cm diameter, $4.3 \times 10^{-3} \text{ m}^3$ volume, 1×10^{-2} mbar base pressure) connected to a vacuum pump via a liquid nitrogen cold trap. First, the hybrid fabric was placed on a glass slide which was then placed in the centre of the coils. The chamber was then evacuated to the base pressure of the apparatus, typically 1×10^{-2} mbar. Once base pressure had been reached, the PFAC8 vapour was introduced into the reactor. The reactor was purged with the vapour for five minutes, and once the the pressure had stabilised at 8×10^{-2} mbar, the radio frequency (RF) generator was switched on to create a 40W continuous wave plasma. This was allowed to run for 10 seconds. At this point the pulse generator was turned on, at a pulsing sequence of 40 μ s on, 20ms off. Once a stable plasma deposition rate was established (indicated by uniform pulse envelope, using an RF probe and oscilloscope), the polymerization was allowed to run for two minutes. At the end of the treatment the RF generator was switched off and the reactor purged for 2 minutes with PFAC8 vapour, prior to being evacuated back to base

pressure. Once base pressure was reached, the vacuum chamber was isolated from the pump, the system brought up to atmospheric pressure and the samples then removed.

6.2.6 Moisture Vapor Transmission Rate (MVTR) Test

Moisture vapor transmission rate of hybrid fabrics were measured following ASTM E96 test method by using a MVTR tester machine in standard test condition lab (20°C, 65% relative humidity). The hybrid fabrics were sandwiched between two aluminum foil discs (adhesive on one side) that had a punched hole (3.81 cm diameter) in the center. This assembly was sealed in a metal dish (64 mm in diameter and 13 mm in depth) filled with 10 g of water. A vibration free turn table carrying 8 dishes rotated uniformly at 5 meters per minute to insure that all samples were exposed to the same average ambient conditions during the test. The assembled specimen in the metal dishes were allowed to stabilize for two hours before taking the initial weight. The specimens were weighed again after a 24 hours interval. . The moisture vapor transmission rate (MVTR) was then calculated in units of $\text{g/m}^2\text{-24 hours}$. The MVP of the hybrid fabrics is determined by normalizing the MVTR results.

6.2.7 Contact Angle Measurements

Contact angle measurements were made using a DropShape Analyser 100 (DSA100, Krüss, Germany). Probe liquids were water, hexadecane, ethylene glycol and di-iodomethane (Aldrich UK, except for the water). Contact angle measurements were made using the built in software.

6.3 Results and Discussion

Figure 6.1 shows a schematic of the process that has been developed. In this novel process, the aligned CNT sheet is taken up onto an electrically conductive mandrel. This mandrel serves as one of the electrodes in the electrospinning process. As the mandrel rotates, the CNT sheet is taken up and at the same time covered with a layer of electrospun nanofibers. Vertically aligned CNT forests were grown on quartz substrate via chloride-assisted low pressure chemical vapor deposition (CVD) and were drawn horizontally to produce the continuous aligned CNT sheet ^[11,56]. The width of the CNT sheet can be controlled by the size of the quartz substrate and is limited only by the dimensions of the CVD furnace. In this study, the drawn CNT sheet was approximately 6 cm wide with an individual CNT length of 1 mm.

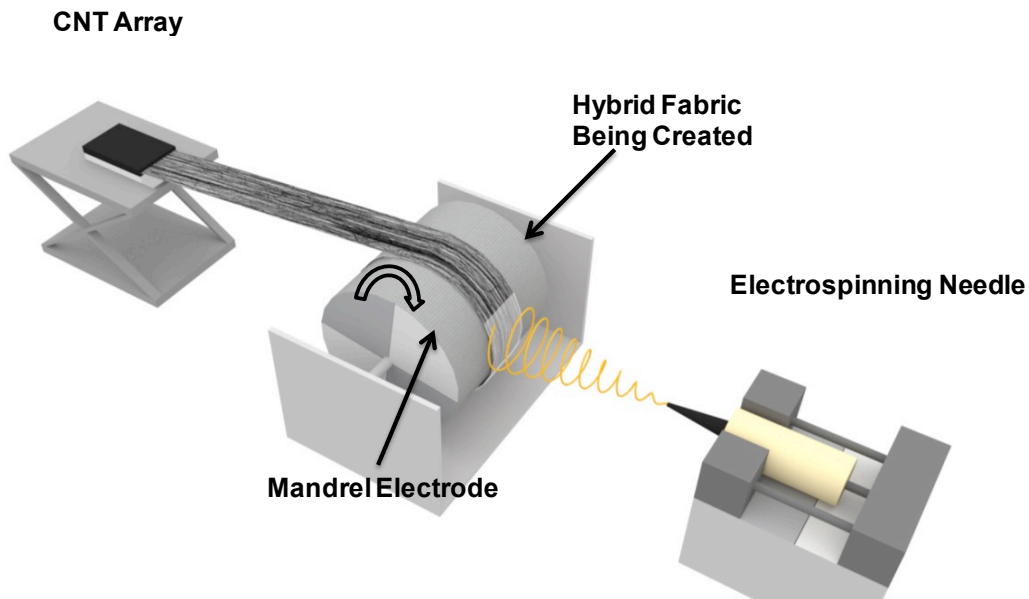


Figure 6.1 Schematic of the hybrid fabric production process where electrospun fibers are taken up simultaneously with aligned CNT sheets.

Figure 6.2 shows an actual picture of the hybridization process, photographic images of the CNT – polymer hybrid nonwoven fabrics and SEM images of representative samples. One of the additional advantages of this process is that the 1 mm long CNTs become trapped by the polymer fiber layers, encapsulating them in the fabric. This significantly reduces the likelihood of CNTs escaping into the environment ^[11]. The mass fraction of the CNTs in the hybrid fabrics is easily controlled anywhere from 0-100% by adjusting the mandrel take-up speed during the process. Slower speed allows for more electrospun fibers to build up while higher speed allows for less polymer fibers to build up.

Figure 6.2 shows a picture of five different samples; two control samples (0% CNTs and 100% CNTs) and samples where the CNT mass fraction was approximately 15%, 30% and 60%. Once the samples were made, we also completed two additional processing steps to understand their effect on the hybrids' properties. The first was to consolidate the fabric under pressure but no heat. The second was to calendar the sample at 70 °C under pressure. Figure 6.2 c-d also show SEM images of the hybrid fabrics' morphology before and after heated calendaring, respectively. Before calendaring, the separate components of the hybrid structure can be clearly seen. The electrospun nanofibers had an average diameter of 250 nm while the CNTs had an average diameter of 30 nm. After heat pressing, a new morphology was created. At low CNT weight fractions, a solid composite film was created. When the CNT weight fraction was high, a porous CNT fabric with melted fiber bond points was created. Surprisingly, a majority of the fabric still retained the individualized CNT structure.

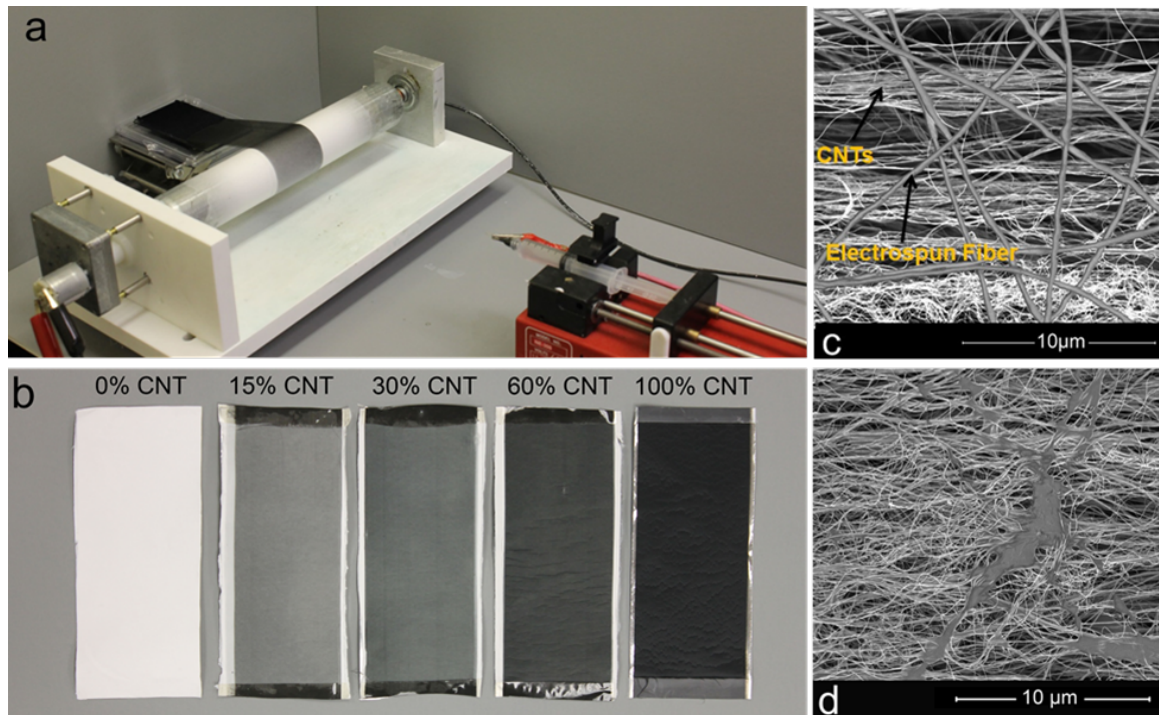


Figure 6.2 a) Setup of the hybrid nanofiber processing equipment, b) CNT – polymer hybrid nonwoven fabrics created with varying weight percentages of CNTs, c) SEM image of the hybrid fabric shows an order of magnitude size difference between CNTs and electrospun nanofibers, d) SEM image showing the same hybrid after calendaring with the melted nanofibers bonding the CNTs together.

The mechanical properties of CNT – polymer hybrid nonwoven fabrics were investigated using a Shimadzu mechanical tester and are shown in Figure 6.3 a. The pure PEO electrospun material exhibited low mechanical properties that were similar to others found in the literature^[28,130,205]. While it is no surprise that the CNTs would reinforce the hybrid fabrics, the level of reinforcement was completely unexpected. The 15% CNT hybrid fabric showed the highest mechanical properties and had a tensile strength, which was 15x higher

than the control sample. Above 15% CNTs, the tensile strength gradually decreased but was still over an order of magnitude higher than the control. The tensile properties of the hybrid fabrics, which were consolidated under pressure, are presented in Figure 6.3b. All of the consolidated samples increased in strength, but the pure consolidated electrospun material still exhibited very low mechanical properties. Among the consolidated hybrid fabrics, the 30% CNT hybrid fabric exhibited the highest tensile strength which was 21x higher than the control sample. It is likely that the applied pressure created more direct contacts between CNTs and PEO nanofibers which provided better load transfer to the CNTs.

Figure 6.3 shows that the tensile strength of the hybrid fabrics increased dramatically after calendaring. Tensile strength of the 15% CNT hybrid fabric increased to 75 MPa, while the 30% CNT hybrid fabric exhibited a tensile strength of 172 MPa which was 49x higher than the control and three orders of magnitude greater than the as-produced PEO nanofiber fabric.

All of these tensile testing results showed a very important relationship. The combination of the carbon nanotubes and polymer nanofibers always exhibited higher mechanical properties than the individual fiber components. When one thinks of a “composite” material typically the mechanical properties lie in between the mechanical properties of the individual components and are skewed towards the component with higher fraction. Here, the samples exhibit a synergistic effect where each component needs the other to develop the high mechanical properties demonstrated. That being said, the strength results for these unique structures are still sometimes counterintuitive. One might assume that increasing the percentage of CNTs would always result in an increase in the mechanical performance.

However, in the case of the as-produced samples the one containing the lowest level of CNTs actually has the highest performance. In these very low density hybrid structures, fiber to fiber contact is essential for transferring load. The sample with the lowest amount of CNTs developed the highest number of contacts with the polymer nanofibers to transfer load. The samples with larger amounts of CNTs have a lower number of interconnections with the polymer nanofibers reducing the effective load transfer. Samples that are pressed and or calendared act more like real composites, where there is an optimal loading of the “strong” component, which are the CNTs in this case. This is because the hybrid structures density increase significantly with pressure and calendaring, making the number of interaction and interconnections between CNTs and polymer nanofiber go up likely by orders of magnitude.

The specific tensile strengths of the fabrics are shown in Figure 6.3d. The as-produced and consolidated 60% CNT hybrid fabrics exhibited the highest specific strength due to its lower density. After heated calendaring, the specific strength of 30% CNT hybrid fabric increased to 239 MPa/gcm⁻³ which is 60x higher than the control sample. In general, when the CNT ratio increased in the hybrid fabric, the specific strength went up, because CNTs are the stronger component and the CNT sheet structure has lower packing density compared to electrospun fibers.

Commercial nonwoven fabrics, which contain drawn microfibers, are much stronger than fabrics made exclusively from nanofibers. One of the goals of the nonwovens industry is to make stand alone nanofiber fabrics which have similar mechanical properties to their commercial products. Using our technique, it appears that this goal is attainable. A

comparison of the CNT-nanofiber hybrid fabrics to traditional thermally bonded micro-fiber nonwoven fabrics is shown in Figure 6.3e. Units are given in grams per tex which is a textile unit of specific strength typically used to quantify strength of nonwoven fabrics. Before calendering, the fabrics strengths were on par with the common range of values found for thermally bonded nonwoven fabrics. After calendering, the fabrics' specific strength increased significantly and was larger than any thermally bonded nonwoven fabrics found in the literature^[206–212].

Figure 6.3f shows the summary of our results next to other examples of CNT reinforced polymer nanofiber fabrics produced using the electrospinning technique. Many research groups have tried to improve the mechanical and electrical properties of electrospun webs by dispersing short CNTs into the spinning solution^[126,136]. Due to dispersion issues, a maximum loading of a few weight percent is possible with this method. The resulting fabrics typically show an increase in mechanical properties, but have been limited to a maximum increase in strength of 4x and typically much lower gains are observed^[27,28,130,142]. Using our process however, we have seen strength increases in our material of up to 49x due to the addition of the CNTs. This is mainly attributed to the large CNT aspect ratios and the much higher CNT loading levels.

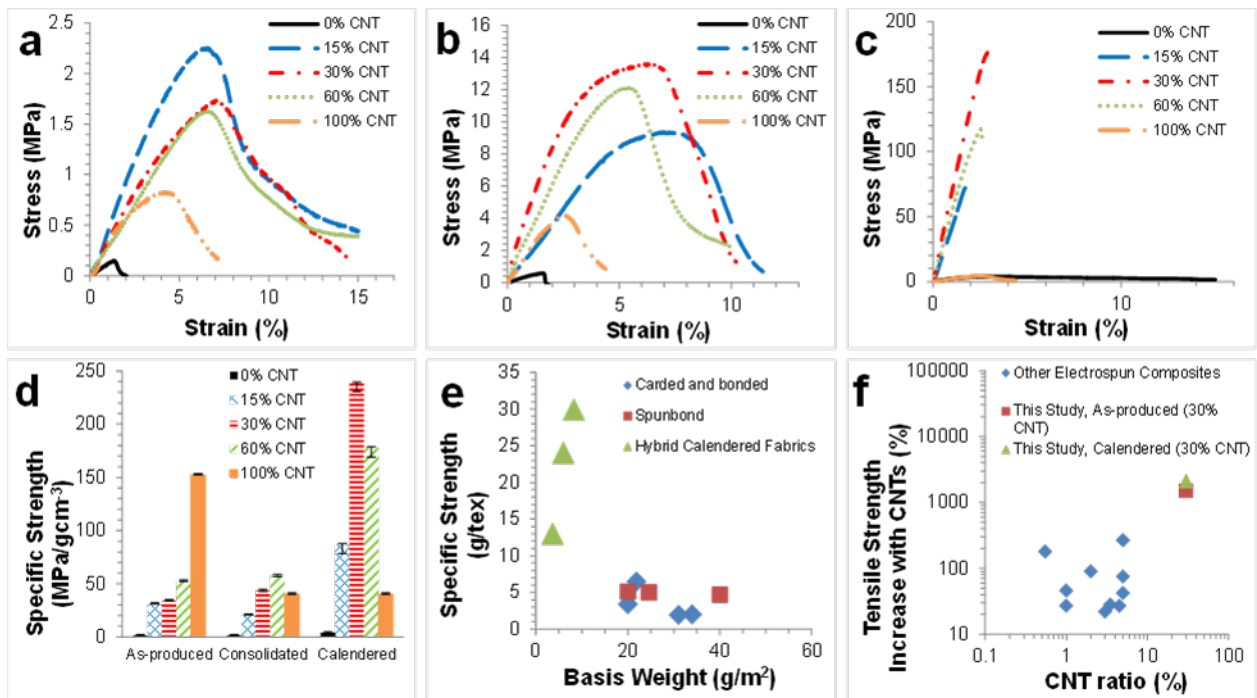


Figure 6.3 (a) Tensile mechanical properties of the as-produced hybrid fabrics with different CNT loadings, (b) Tensile mechanical properties of the hybrid fabrics after consolidation under pressure, (c) Tensile mechanical properties of the hybrid fabrics after calendaring at 70 °C, (d) Comparison of specific strength between control sample and hybrid fabrics, (e) Comparison of our best mechanical properties (calendered, 60% CNT hybrid fabric) to thermally bonded nonwovens from references^[206–212], (f) Strength increases seen for our hybrids as compared to electrospun fabrics with CNTs in the spinning solution from references^[20,23,27,126,130,133,137,142,205,213].

Electrical conductivity of hybrid fabrics was measured using a 4-probe setup where the fabrics were laid across four sputtered gold electrodes. The results showed that as-produced hybrid fabrics had similar conductivity as seen in Figure 6.4. This result proved that even though nonconductive polymer nanofiber layers were deposited in between layers of the

CNT sheet, a number of CNTs were still able to make electrical contact allowing every CNT sheet layer to contribute to the conductivity. Even the hybrid with 15% CNTs showed electrical conductivity. After consolidation under pressure, the electrical conductivity increased to 50 S/cm for 30% and 60% CNT hybrid fabrics. However, since the interconnection between the layers was likely lower for the 15% CNT hybrid fabric, the electrical conductivity did not increase as much as the other consolidated hybrid fabrics. When hybrid fabrics were calendared, electrospun fibers between CNT layers melted and the CNT interconnections reached a maximum level while the thickness was decreased. This increased the electrical conductivity to 205 S/cm for the 60% CNT hybrid fabric. After consolidation, the pure CNT sheet exhibited an electrical conductivity of 115 S/cm meaning that the 60% CNT hybrid fabric showed higher electrical conductivity than pure consolidated CNTs. We hypothesized that after calendaring the hybrid fabrics, the polymer shrank and helped the CNTs to come into closer permanent contact with each other. This behavior has also been reported previously in the literature by others that have melted polymer-CNT assemblies^[214].

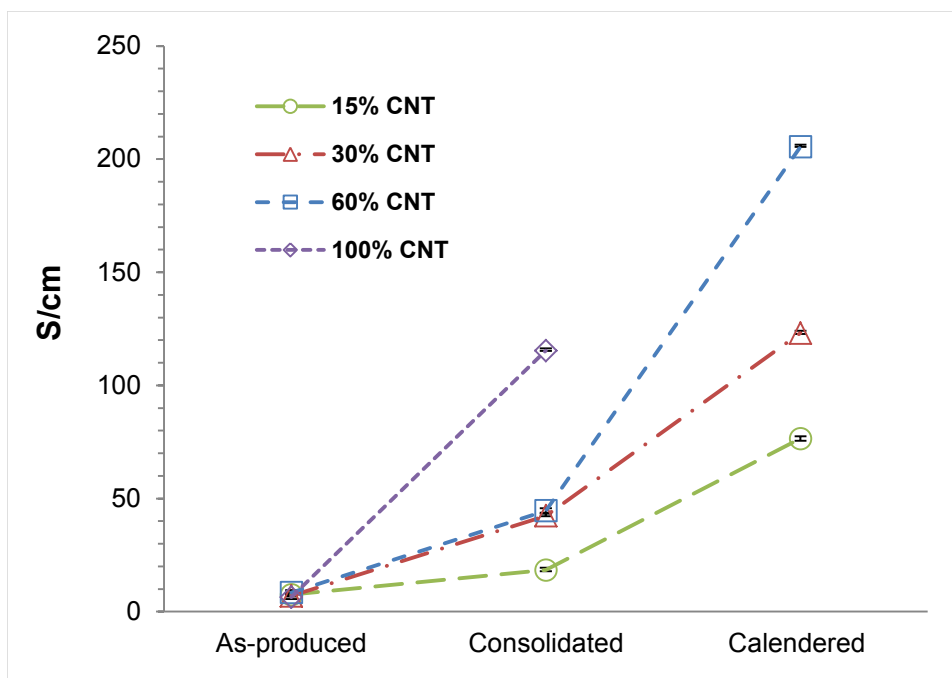


Figure 6.4 Electrical conductivity of the as-produced, consolidated and calendered hybrid fabrics and pure as-produced and consolidated CNT sheet samples.

One of the major applications of nanofiber fabrics is in air filtration. Electrospun nanofibers typically show a significant advantage in aerosol filtration efficiency due to their large specific surface area and small pore size in comparison to commercial textiles^[80,81]. However their lower tensile strength means that they have to be used with supporting nonwoven fabrics^[12,13]. Recently it was shown that filters containing aligned CNT sheets also exhibit excellent filtration properties. The CNTs have smaller fiber diameters and higher filtration efficiencies at lower pressure drops compared to electrospun fibers^[11]. CNTs must be permanently trapped in the fabric so that they act only as a filtering agent^[11]. The CNT-nanofiber hybrid fabrics show high potential in the area of filtration because they work around many of the disadvantages of CNT and nanofiber based filters.

Figure 6.5 shows filtration performance of CNT – polymer hybrid nonwoven fabrics, in terms of the particle penetration percentage, for the standard 10-300 nm particle size range tested. There are three basic mechanisms that lead to capture of an aerosol particle in neutral fibrous filters: interception, inertial impaction and Brownian diffusion. The total particle collection efficiency of a filter is the combination of these three capturing mechanisms^[14,89]. Overall filtration performance is a function of the fiber diameter, packing density, filter thickness, and the sum of single fiber efficiencies due to these three different deposition mechanisms^[12]. The filtration performance of 7-layer CNT – polymer hybrid nonwoven fabrics with different CNT loadings are shown in Figure 6.5a. The penetration for the control sample was 10.54%, while the 60% CNT hybrid fabric decreased penetration to 0.024% at the 0.3 μm particle size. The 15% CNT hybrid fabric decreased penetration one more order to 0.0019% at the 0.3 μm particle size due to more electrospun fibers in the hybrid fabric (lower mandrel rotation speed but same number of total rotations). Due to the small diameters of CNTs, the most penetrating particle size (MPPS) of hybrid fabrics was around 70 nm which is lower than for conventional micro fibers^[12]. Addition of the CNTs to the hybrids increased the overall surface area of the fabrics which enhances the filtration efficiency in diffusion regime^[89].

Filtration of ultrafine particles is accomplished by using HEPA (high efficiency particulate air) or ULPA (ultra-low penetration air) filters. The requirement for a HEPA filter is at least 99.97% filtration efficiency at the 0.3 μm particle size. The ULPA designation requires at least 99.999% filtration efficiency of particles 0.12 μm particle or larger^[11]. All the as-produced hybrid fabrics reached the HEPA filter standards and the 15% CNT consolidated

hybrid fabric met the ULPA filter requirements with the value of 0.0019% penetration at 0.1 μm particle size. This was achieved with a fabric with a thickness of only 20 microns and areal density of 8 g/m^2 .

Pressure drop is another important parameter for aerosol filters. A low pressure drop is always a desired filtration property due to energy requirements in large scale of filtration process. Fiber diameter, thickness of the filter media, fiber packing density, and face velocity directly affect pressure drop^[11]. Figure 6.5c shows the particle penetrations versus pressure drops of as-produced and consolidated hybrid fabrics at 15 cm/s face velocity. The as-produced hybrid fabrics showed a lower pressure drop compared to the consolidated hybrids due to decreased pore sizes and high packing density after consolidation.

It is desirable to have the highest filtration efficiency and the lowest pressure drop in any filter. Filter quality factor (QF) is a parameter used to compare filter types and filters of varying thickness, and is a ratio between filtration efficiency and pressure drop^[11,13].

$$QF = -\frac{\ln P}{\Delta p} \quad \text{Equation 35}$$

where P is the filter penetration and Δp is the pressure drop. The most efficient filter is the one that has the greater value of QF. Figure 6.5d shows the comparison of the QF between the 60% CNT hybrid fabrics and the control samples before and after consolidation. The as-produced and consolidated control samples both had the lowest QF. The QF of the 60% CNT

hybrid fabrics was significantly higher because their filtration efficiency increases were more significant than the pressure drop increases.

The calendered hybrid fabrics showed much higher pressure drop making them less attractive for filtration applications. However, at the 60% CNT loading level the fabric appeared very porous making this material attractive for micro-porous membranes. Micro-porous membranes and laminated fabrics, are used as barrier materials for protective clothing applications, and can provide a high level of protection from liquids while still allowing water vapor to escape^[193,194,215–217]. However, these types of fabrics typically have lower water vapor permeability which lowers the comfort level for the wearers^[193,194,216]. Therefore, the most common expectations from barrier materials for protective clothing applications are a combination of adequate barrier performance and comfort, simultaneously^[193,194,215]. Electrospun nonwoven mats have improved breathable barrier fabric properties due to high specific surface area, high porosity and small pore sizes. However, since electrospun nonwoven mats have low mechanical properties, they are commonly laminated on to thicker supporting fabrics which may affect the barrier and comfort performance of the final material^[216,218].

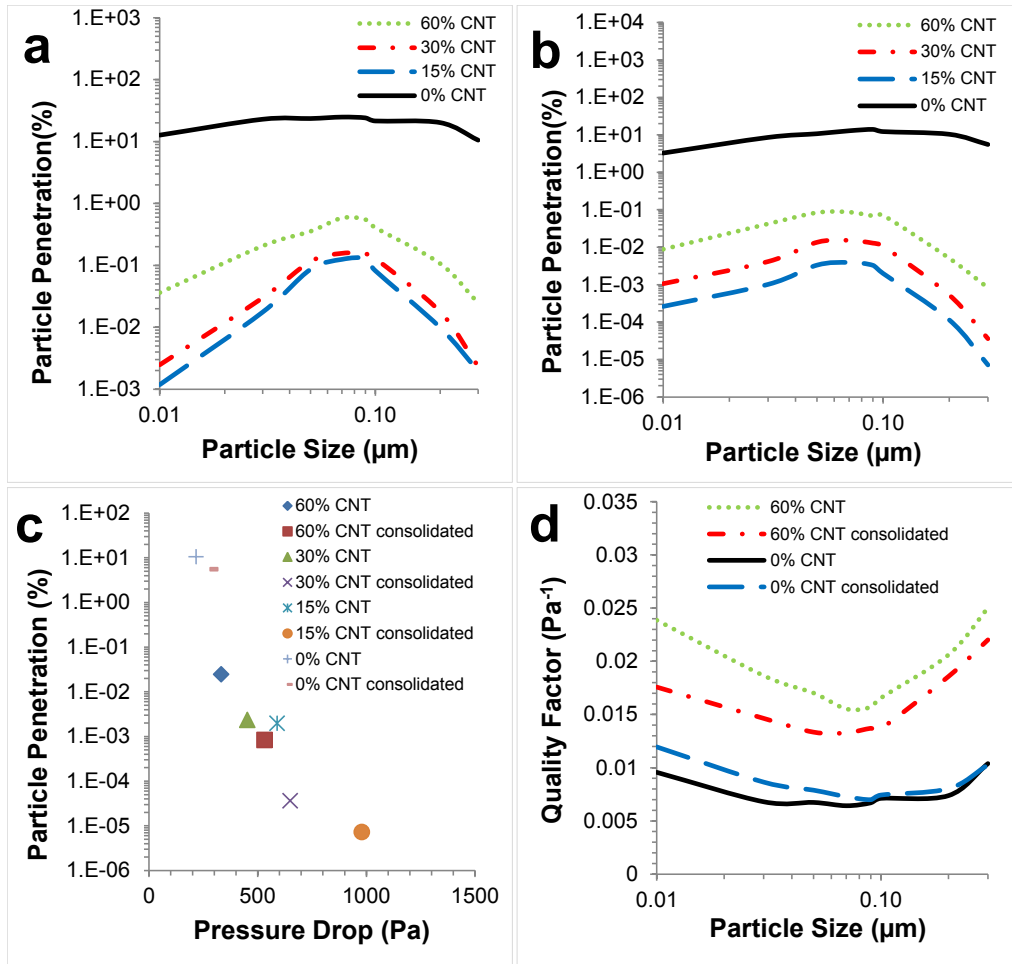


Figure 6.5 (a) The hybrid fabrics with different CNT fiber loading, evaluated for particle penetration for a range of particle sizes at a face velocity of 15 cm/s, (b) The hybrid fabrics with different CNT fiber loading after consolidated under pressure, evaluated for particle penetration for a range of particle sizes at a face velocity of 15 cm/s, (c) Particle penetration fraction of the hybrid fabrics at different CNT fiber loading before and after consolidation as a function of pressure drop at 0.3 μm particle size and 15 cm/s face velocity, (d) Quality factor as a function of DOP particle size, ranging from 0.01 to 0.3 μm , at 15 cm/s face velocity.

The unique combination of high specific surface area, flexibility, light weight, and porous structure with the desired level of high tensile strength makes these CNT – polymer hybrid nonwoven fabrics excellent candidates for use in stand alone barrier fabrics for protective garments. Figure 6.6 shows the barrier and water vapor permeability performance of hybrid fabrics. The water vapor permeability (MVP) of the 7-layer 60% CNT hybrid fabrics in the different structures (as-produced, consolidated, and calendered) is shown in Figure 6.6a. All the CNT hybrid fabric samples showed essentially the same moisture vapor transmission rate (MVTR). However, the as-produced hybrid fabric showed higher MVP compared to consolidated and calendered samples, because the as-produced hybrid fabric had a larger thickness which directly affects the MVP value.

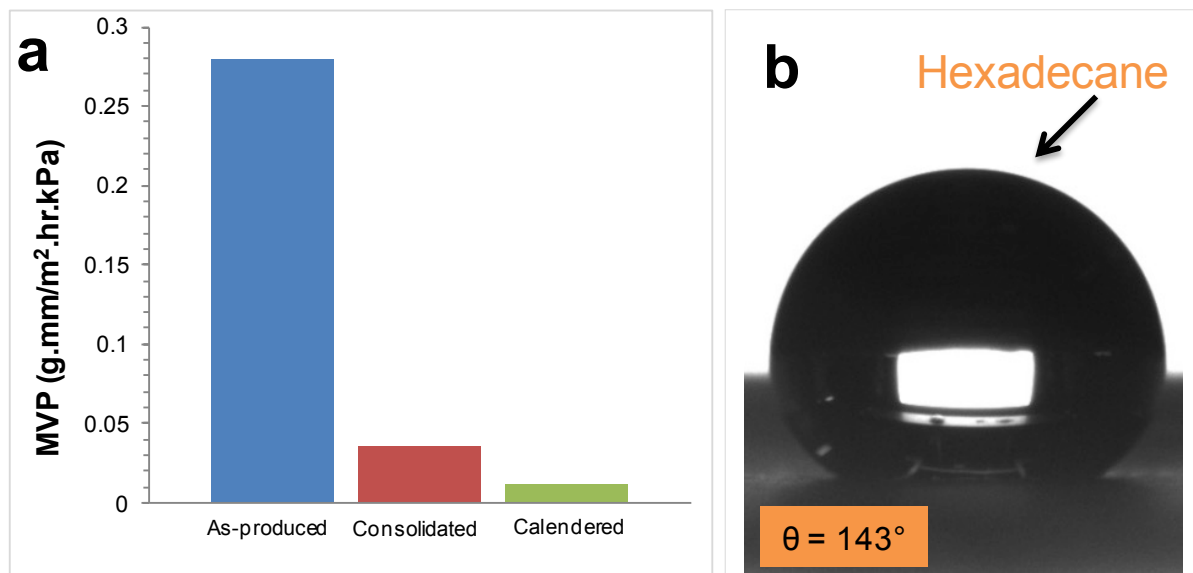
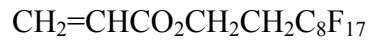


Figure 6.6 a) MVP results for hybrid fabrics, b) A droplet of hexadecane on a 60% CNT consolidated hybrid fabric.

In order to improve the hybrid fabrics performance against chemical agents, the hybrid sheets were treated with a low surface energy chemical, perfluorooctylethyl acrylate^[219] (PFAC8, 1) using pulsed polymerization.



Equation 36

Pulsed plasma polymerisation of PFAC8 on the microsecond-millisecond timescale has been shown to produce a polymer with high levels of structural integrity^[220]. The greater control associated with this technique is due to the limited fragmentation that occurs during the “on” time of the pulse sequence and the conventional gas phase chemistry that occurs during the “off” period. By varying the “on” and “off” times and the radio frequency power level, the process may be optimized and the desired surface characteristics obtained^[221–223].

Pulsed plasma polymerisation of PFAC8 occurs predominantly via its acrylic double bond, depositing a polymer that resembles conventional poly(PFAC8) produced by liquid phase free-radical polymerisation. Once applied to the fiber surfaces of the hybrid materials, the perfluoroalkyl chains in the outermost layer of the thin polymer film orientate themselves normal to the fiber surfaces, forming a sheath of closely-packed CF₃-terminated perfluoroalkyl groups^[220]. The critical surface tension and surface energy values of this structure are exceedingly low (ca 4 mNm⁻¹ and 8 mJm⁻² respectively)^[221,224], resulting in remarkable liquid-repellent properties, especially when applied to fibrous substrates^[219,225,226].

After the plasma treatment, contact angle measurements were made using a series of probe liquids consisting of water, hexadecane, ethylene glycol and di-iodomethane (Table S3, Supporting Information). A droplet of hexadecane on a 60% CNT consolidated hybrid fabric is shown in Figure 6.6b. The contact angle is very high for such a low surface tension organic liquid. The very high contact angle of 143° is attained through a combination of the extremely porous nano-fiber surface and the low surface energy coating^[227]. The combination of high water vapor permeability and protection against harmful liquid chemicals make these hybrid fabrics excellent candidates for chemical protective garments^[228].

6.4 Conclusions

In summary, we have developed a novel process to produce nanoscale nonwovens through a hybridization of high aspect ratio CNTs and electrospun fabrics, which were processed in a way that is conducive to future commercial production. Due to the unique properties of the CNTs, the hybrids showed extremely high tensile strength, small pore size, high specific surface area and electrical conductivity. In order to further examine hybrids properties, they were consolidated under pressure, and also calendered at 70°C . The hybrid fabrics remained porous even after calendering and look similar to thermally spot bonded nonwoven fabrics. After heated calendering, the fabrics' strength increased immensely due to better bonding and interconnection with the CNTs. The specific strength values were larger than for any thermally bonded nonwoven fabrics found in the literature. The fabrics also exhibited very good particle filtration and barrier properties. These novel hybrid fabrics may be desirable as stand alone fabrics in applications such as aerosol and liquid filtration, protective garments,

barrier membranes, tissue scaffolds and catalyst support structures. PEO was utilized as the polymer nanofiber in these hybrid fabrics, however, the technology can easily be extended to many other fiber systems in future studies.

Acknowledgements

The authors acknowledge the Turkish Ministry of National Education for provision of a Ph.D. scholarship to Ozkan Yildiz, and Dr. Yuntian Zhu at NC State University for use of the Shimadzu mechanical tester machine. The authors acknowledge the use of the Analytical Instrumentation Facility (AIF) at North Carolina State University, which is supported by the State of North Carolina and the National Science Foundation. The authors also thank Engin Kapkin for assistance with illustrations.

Chaper 7 Flexible Si – CNT Hybrid Anode Architecture for Lithium-Ion Battery Electrodes Based on a Hybrid CNT-Nanofiber Structure

Ozkan Yildiz^a, Mahmut Dirican^a, Xiaomeng Fang^a, Kun Fu^a, Kelly Stano^a, Xiangwu Zhang^a,
Philip D. Bradford^{a*}

^a Department of Textile Engineering, Chemistry and Science, North Carolina State University, Raleigh, North Carolina 27695, United States

Abstract

Recent battery research has increasingly focused on developing new composite and hybrid electrode structures with higher energy capacity and longer cycle life. Silicon is one of the most promising anode materials for lithium batteries due to its highest known theoretical charge capacity (4,200 mAhg⁻¹). However, silicon anodes have found limited application in commercial batteries because of the significant volume change (up to 400%) of silicon during cycling, which results in pulverization and capacity fading. Here, we present a new method to develop a silicon - carbon nanotube (CNT) hybrid anode architecture using CNT-polymer nanofiber hybridization method. The novel anode material was produced by simultaneously electrospinning PMMA-Si nanofibers onto aligned CNT sheets which were drawn on a grounded, rotating mandrel, and then subsequently decomposing the PMMA electrospun fibers at elevated temperature to create even distribution of Si particles within the CNTs. In order to enhance the mechanical bond between CNT and Si, the whole structure was then coated with pyrolytic carbon via chemical vapor deposition (CVD). The novel

architecture provided sufficient space to accommodate the volume expansion of the Si nanoparticles. The CVD pyrolytic carbon coating helped maintain Si nanoparticles position within CNT sheets and stabilized solid-electrolyte-interface (SEI) formation. The novel freestanding, binder free CNT-Si-C sheet hybrid exhibited improved performance in terms of excellent cycling capacity (1470 mAhg^{-1}), high coulombic efficiency (98%), and good capacity retention of 88% after 150 cycles.

7.1 Introduction

The high energy and power density of lithium-ion batteries (LIBs) have allowed them to dominate the portable electronic markets for over two decades. With continued development, LIBs are now being intensively pursued for transportation applications and grid storage systems. In order to achieve high capacity and long cycle life requirements of these large scale applications, there has been significant effort to explore new materials and design novel structures for high performance LIBs^[146,149,229]. Graphitic material has been widely used as a commercial anode material for lithium-ion batteries because of its low cost, long cycle capacity, and low flat working potential. However, the theoretical capacity of graphite material is 372 mAh/g , which is insufficient to meet the capacity requirements of future portable electronics, and the high energy-storage demands in the transportation or grid storage applications^[230–232]. Therefore, in order to replace the graphite anode material, researchers have focused significant attention on alternative anode materials with higher capacities. Silicon, tin, germanium and their oxides are other alloy types of anodes, the

lithium storage capacities of which are much higher than commercially used intercalation-type graphite anodes^[150,157].

Among all alloy type anodes, silicon (Si) has the highest theoretical capacity of 4200 mAhg⁻¹, which makes it one of the most promising anode materials for next generation lithium-ion batteries^[152,153]. On the other hand, the structural failure induced by the large volume change (up to 400%) of Si during electrochemical cycling causes serious pulverization of active Si material and accelerates the formation of solid electrolyte interphase (SEI)^[156,154,155]. This structural characteristic causes reduced capacity and poor cycling life^[233]. In order to address the large volume change and maintain the structural integrity, several different strategies have been proposed. One of them is reducing the Si particle size to the nanoscale in order to minimize the cracking and pulverization of Si particles^[156]. The other method is creating open spaces for active Si particles in order to accommodate the Si volumetric change during cycling^[234]. The combination of carbon with the silicon structure has drawn significant attention due to carbon's excellent electrical conductivity, large surface area, open pore structure, and superior chemical and electrochemical stability. In addition, coating carbon layer provides structural integrity by buffering the large silicon volume change, which helps form a stable SEI film^[235,236].

There are several different traditional techniques for fabricating Si based electrodes. One technique is using electronically inactive materials such as polymer binder, conducting agent, and copper current collector, because most of the reported Si/C composite anodes are not suitable for direct use in flexible lithium-ion batteries^[56,237]. However, there are

drawbacks of using this method including reduction in the volumetric and gravimetric energy densities, additional time to prepare, and high cost^[56,157]. Another common technique is electrospinning of mixed Si nanoparticles with carbon source polymer solution, such as polyacrylonitrile (PAN)^[238] or polyvinylalcohol (PVA)^[150]. However, some Si particles stay on the fiber surface and react directly with the electrolyte, which causes heavy SEI formation^[238]. Nanoparticles trapped within the nanofibers expand and rupture the fibers after cycling. For both of these reasons, Si-CNF composites have not reached their predicted performance over long term cycling. In order to address these challenges in the traditional methods and to get stable cycling performance, new processing techniques are needed in which binder free electrodes containing Si and carbon can act in a mutually beneficial way and where there is enough free space for Si expansion during cycling yet the Si remains in contact with the carbon phase at all times.

Continuous aligned CNT sheets are excellent candidates for producing electrodes due to their small fiber diameter, high surface area, electrical conductivity, and graphitic structure^[239–241]. Besides their unique properties, CNT sheets can provide an ideal scaffold for loading active materials to accommodate the volume fluctuation during cycling^[56,242]. In this work, a novel technique is created that deposits Si nanoparticles by simultaneously electrospinning PMMA-Si nanofibers onto aligned CNT sheets which are drawn and collected on a grounded, rotating mandrel. The uniform deposition of PMMA-Si electrospun fibers provides homogenous Si deposits inside the CNT sheet. The free-standing electrically

conductive novel architecture CNT-Si sheet hybrids can be used directly as binder-free, high energy electrodes. However, the Si nanoparticles have been easily exposed inside the CNT sheets. Therefore, in order to protect the exposed Si nanoparticles inside of the CNT sheets, and strengthen mechanical bonding between CNTs and Si nanoparticles, the CNT-Si sheet hybrid was coated with nano-scale pyrolytic carbon layer by chemical vapor deposition (CVD) technique. Results showed that the novel architecture CNT-Si sheet hybrid provides more free volume for Si expansion. In addition, the pyrolytic carbon coated CNT-Si-C sheet hybrid improved the initial coulombic efficiency and cycle performance.

7.2 Experimental

7.2.1 CNT Synthesis

Vertically aligned multi-walled carbon nanotubes (MWCNT), with individual CNT diameters of 30 – 50 nm and length of 1 mm, were synthesized on quartz substrate via a modified version of the chlorine mediated chemical vapor deposition process. In this method, first, the catalyst, Iron II chloride (FeCl_2), and quartz substrate were placed inside of the tube furnace, and then the chamber was sealed and pumped to less than 10 mTorr. Then the chamber was heated to 760 °C, after which the growth gases, acetylene (600 sccm), argon (395 sccm), and chlorine (5 sccm) were introduced into the chamber. The reaction took place for 20 min, after which time the chamber was returned the starting conditions (ambient temperature and atmospheric pressure). The height of the CNT array was approximately 1 mm. CNT sheets were drawn from the as-grown forests by a dragging a razor blade across one edge of the CNT array. After starting the drawn CNT sheet, it could be easily attached

the mandrel and drawn up to 0.5 m/s speed. In this study, the dimensions of CNT arrays had of 60 mm width and 100 mm length^[11,243].

7.2.2 Hybrid Fabric Preparation

Poly methyl methacrylate (PMMA) of $M_w = 350,000$ g/mol was purchased from Sigma Aldrich. PMMA solution was prepared by mixing 25 wt% PMMA in dimethylformamide (DMF) solution, and then stirring for one day. Then 15 wt% silicon particles (30-50 nm in diameters that were purchased from Nanostructures & Amorphous Materials, Incorporated) were added in PMMA + DMF solution and then stirred for another day. When PMMA + Si was completely dissolved in DMF, the polymer solution was loaded into a 10 mL syringe with luer-lock connection and used in conjunction with a 1.27 cm, 22 gauge blunt tip needle. The electrospinning apparatus included a syringe pump from New Era Pump Systems (model NE-300), which operated at a flow rate of 1 mL h^{-1} . The high voltage power supply was from Gamma (High Voltage model ES40P-20W/DAM). The operating voltage varied from 10 to 15 kV and the distance between the collector and needle was 15 cm. The mandrel was used as an electrode during the electrospinning process and rotated by a Regulated DC Power Supply (model DIGI 360).

A novel CNT-PMMA+Si hybrid structure was produced by simultaneously electrospinning PMMA + Si nanofibers onto aligned CNT sheets, which were drawn and collected on a grounded, rotating mandrel. The mandrel's diameter was approximately 15 cm and its speed was 0.25 cm/s. After using this novel hybridization method^[190], continuous electrospun PMMA + Si polymer nanofibers were fully integrated among the aligned CNT

sheets trapping them inside the CNT sheets (diameter \approx 30 nm, aspect ratio \approx 50,000). While producing a 30 layer CNT – PMMA+Si hybrid structure through this process, 5 layer CNT sheets were rolled on the top and bottom of the hybrid fabric making a sandwich structure. The 5 layer sheets provided for a structure to enclose PMMA+Si electrospun nanofibers within the CNT sheets. The 40 layer CNT – PMMA+Si hybrid structures were placed onto a quartz substrate and then another quartz substrate was put onto hybrid structure. Then it was transferred into the horizontal tube furnace to decompose the PMMA polymer fibers. The decomposition process was carried out in Ar gas with a flow rate of 500 sccms at 500 °C for 1 hour. In order to deposit pyrolytic carbon onto the silicon deposit CNT + Si hybrid fabric, the sample was inserted into the CVD chamber and heated directly to 760 °C. Then the acetylene gas was introduced to the hybrid sample at a flow rate of 600 sccm at 20 Torr for 30 min^[56]. After the carbon treatment process, the system was purged with Ar gas at a flow rate of 1000 sccm while cooling.

7.2.3 Characterization

The morphology of the samples was investigated by transition electron microscope (TEM, HITACHI HF2000) and field emission scanning electron microscope (FE-SEM, JEOL 6400F). The structure of the hybrid samples was studied by wide angle X-ray diffraction (WAXD, Rigaku Smartlab) and a Renishaw Raman microscope (514 nm).

7.2.4 Electrochemical Evaluation

The electrochemical properties of the hybrid samples were tested using CR 2032 type coin cells. The novel hybrid samples were freestanding, conductive nonwoven mats, which were used directly as the working electrode without addition of binder material or conductive agent. The average working electrode mass was 0.4-0.5 mg. The electrode mass was measured on a balance with a resolution of 0.01 mg. The counter electrode was lithium ribbon (99.9% Aldrich) and the separator was Celgard 2400 membrane. The electrolyte used was 1 M LiPF₆/ethylene carbonate (EC) + dimethyl carbonate (DMC) + diethyl carbonate (DEC) (1:1:1 by volume, MTI Corporation). Coin cells were assembled in a high-purity argon-filled globe box. Galvanostatic charge-discharge experiments were investigated the electrochemical performance at a constant current density of 100 mA g⁻¹ with cut-off potentials between 0.1-2.0 V using a LAND-CT 2001A battery test system. The rate capability tests were evaluated at current densities of 50, 100, 200, 400, and 800 mA g⁻¹ using the same instruments.

7.3 Results and Discussion

In this communication, we present a novel CNT-Si sheet structure, which is lightweight, freestanding, binder-free and flexible as anode for lithium-ion batteries. This novel CNT-Si structure was created from the CNT-polymer hybrid fabric, which was produced by simultaneously electrospinning PMMA-Si nanofibers onto aligned CNT sheet. The super aligned CNT sheet acts as the scaffold, the current collector and electrochemically active substrate onto which electrospun fibers are deposited. The Si nanoparticles are

deposited via PMMA electrospun fibers, which can be easily decomposed at elevated temperature. The homogeneous electrospun PMMA deposition onto aligned CNT structure provides the uniform deposition of Si nano-particles on each CNT sheet layer. The high surface area and high porosity of aligned CNT structure provides to be embedded the Si particles inside of the CNT sheet layers and to accommodate the Si expansion during cycling. This method allowed us to load Si within the CNT sheet without the need for liquid processing. This is crucially important because using a liquid dispersion to deposit the Si particle inside of the CNTs would have created much larger agglomerations of Si particles and huge tightly packed bundles of CNTs due to capillary drying effects^[244]. The electrospun fibers actually help to create a very low density structure which is retained when the polymer portion of the fibers is removed. The density of the CNT-Si hybrid materials was approximately 0.59 g/cm^3 before compressing the structure in the coin cell fabrication. Figure 7.1 shows a schematic of the fabrication process of the novel CNT-Si hybrid in three steps: 1) producing CNT-PMMA-Si fabric by the hybridization method, 2) decomposition of PMMA electrospun fibers in the structure, and 3) CVD carbon coating of novel CNT-Si sheet hybrid. Vertically aligned CNT forest was grown on substrate and was drawn horizontally out onto an electrically conductive mandrel, which served as one of the electrode in the electrospinning process.

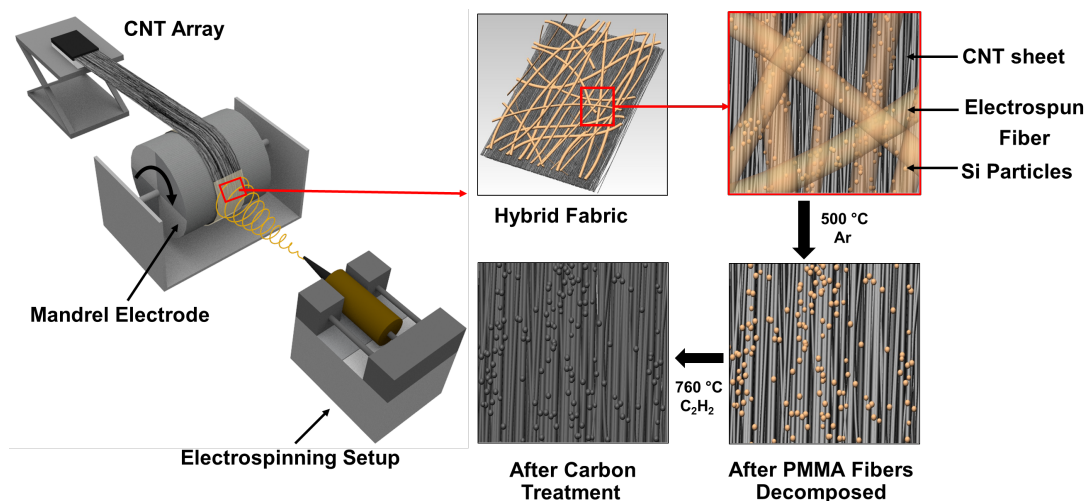


Figure 7.1 Schematic for producing novel CNT-Si and CNT-Si-C sheet structures. CNT-PMMA-Si hybrid fabric was prepared by simultaneously electrospinning PMMA + Si nanofibers onto aligned CNT sheets, which were drawn and collected on a grounded, rotating mandrel. The self-supported hybrid fabric was treated at elevated temperature to decompose PMMA electrospun fibers. A continuous novel CNT-Si-structure was obtained. Then the novel architecture of CNT-Si sheet was coated pyrolytic carbon as the main active anode material for the LIBs.

Figure 7.2 a shows the actual picture of the novel CNT-PMMA-Si hybrid fabric processing method. The CNT-PMMA-Si hybrid fabric was produced on a copper-foil-covered roller. Adjusting the mandrel take up speed during the process easily controlled the mass fraction of the electrospun polymer in the hybrid fabric. The mass fraction of the components in the CNT-PMMA-Si hybrid fabric was 30% CNT, 56% PMMA and 14% Si. Figure 7.2b shows the 30 layer hybrid after each processing step. From left to right, the fabrics are: (1) as-produced CNT-PMMA-Si hybrid fabric; (2) after decomposition of

electrospun PMMA fabric (CNT-Si); and (3) after carbon coating sample (CNT-Si-C). The light yellowish color of the hybrid structure changed to black after carbon coating. The freestanding and binder free CNT-Si-C sheet hybrid shows good flexibility, as seen in Figure 7.2c. The self-supported hybrid structure could be easily integrated into a rolled or stacked battery cell without using any binder or metal current collector. It was found that the freestanding CNT-Si-C hybrid could endure repetitive cycles of bending or folding without developing any damage. Hence, it is feasible that the novel freestanding CNT-Si-C hybrid could be engineered to roll-to-roll process for commercial battery production. In this study, the 12.5 mm diameter disks were punched to use as the anodes in coin cells (Figure 7.2d).

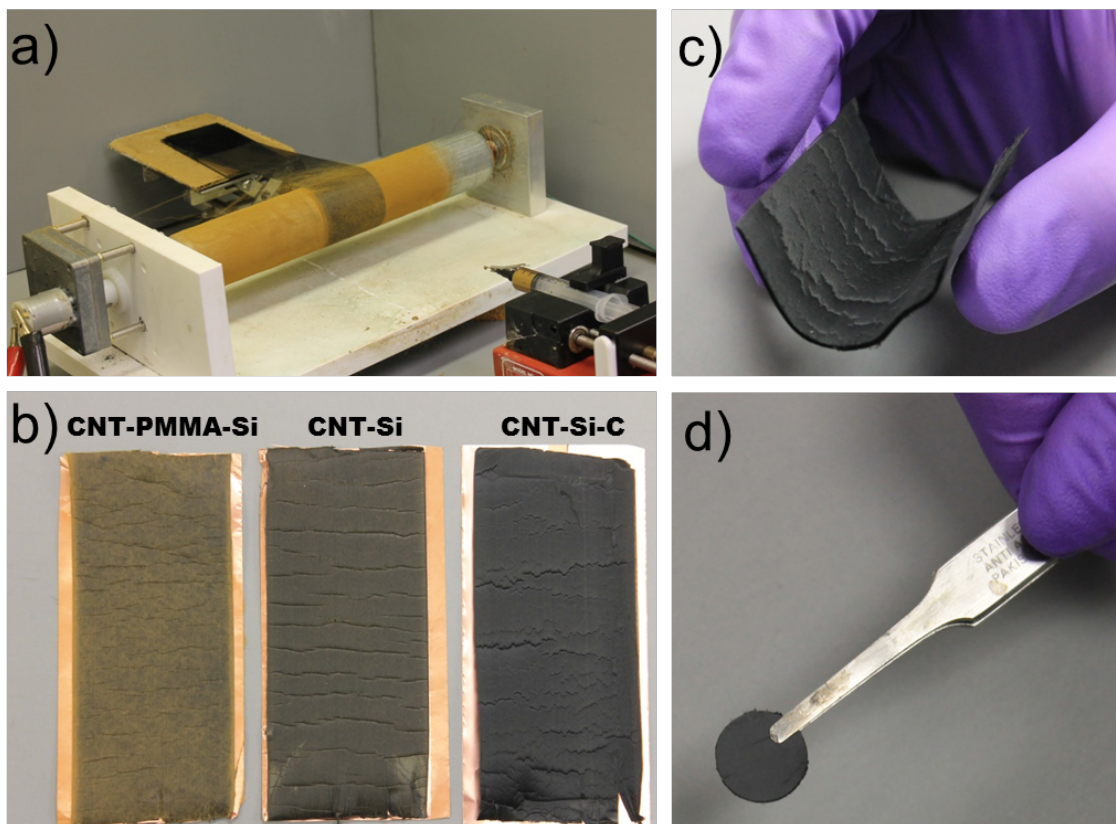


Figure 7.2 (a) Photographic image of the CNT-PMMA-Si hybrid fabric processing setup, (b) Photographic image for each processing method. From left to right, the fabrics are: (1) as-produced CNT-PMMA-Si hybrid fabric; (2) after decomposition of electrospun PMMA fabric (CNT-Si); and (3) after carbon coating sample (CNT-Si-C), (c) Photographs of a flexible novel CNT-Si-C sheet composite with different folded structure, (d) A free-standing and binder-free electrode for lithium ion cell testing.

The morphology of the novel CNT-PMMA-Si hybrid fabric and CNT-Si and CNT-Si-C sheet hybrids was examined using SEM as seen in Figure 7.3. The SEM images of

CNT-PMMA-Si hybrid fabric show that continuous electrospun PMMA-Si fibers coated onto the aligned CNT sheets surface (Figure 7.3a-b). The fibers ranged from 400-450 nm in diameter. Figure 7.3c-d and Figure 7.3e-f show SEM images of novel CNT-Si and CNT-Si-C sheet hybrid structures, respectively. At lower magnifications, it is seen that electrospun PMMA fibers were completely decomposed and Si nanoparticles were dispersed throughout the CNT fabric structure. At high magnifications, the surface morphology of novel CNT-Si and CNT-Si-C sheet hybrids were different and CVD carbon coating could be easily observed from the SEM images.

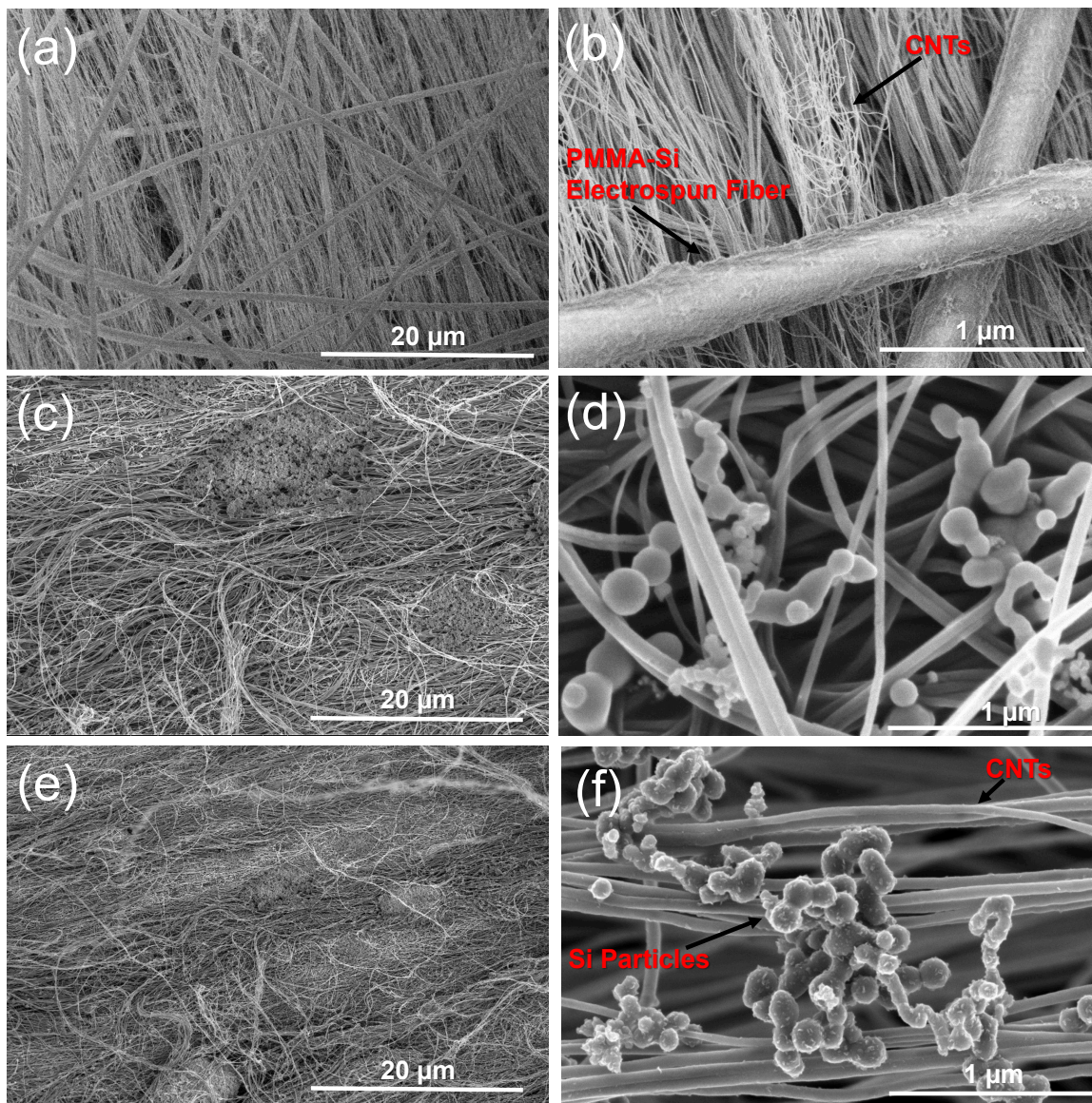


Figure 7.3 Structures of CNT-PMMA-Si, CNT-Si, and CNT-Si-C sheets. Figure a-b is the CNT-PMMA-Si hybrid nonwoven structure at high and low magnification. Figure c-d images of the CNT-Si sheet structure at high and low magnification. Figure e-f are the images of CNT-Si-C sheet structure at high and low magnification.

Figure 7.4 shows TEM images of the novel CNT-Si and CNT-Si-C hybrids. It was observed that the surface of the Si nanoparticles was coated with thin pyrolytic carbon layer of around 20 nm thick. This nanoscale pyrolytic carbon layer was very important for enhancing the bonding between Si nanoparticles with CNTs. In addition it is important for stable SEI formation on the surface of Si during repetitive electrochemical reactions, especially for agglomerated Si nanoparticles between the CNTs.

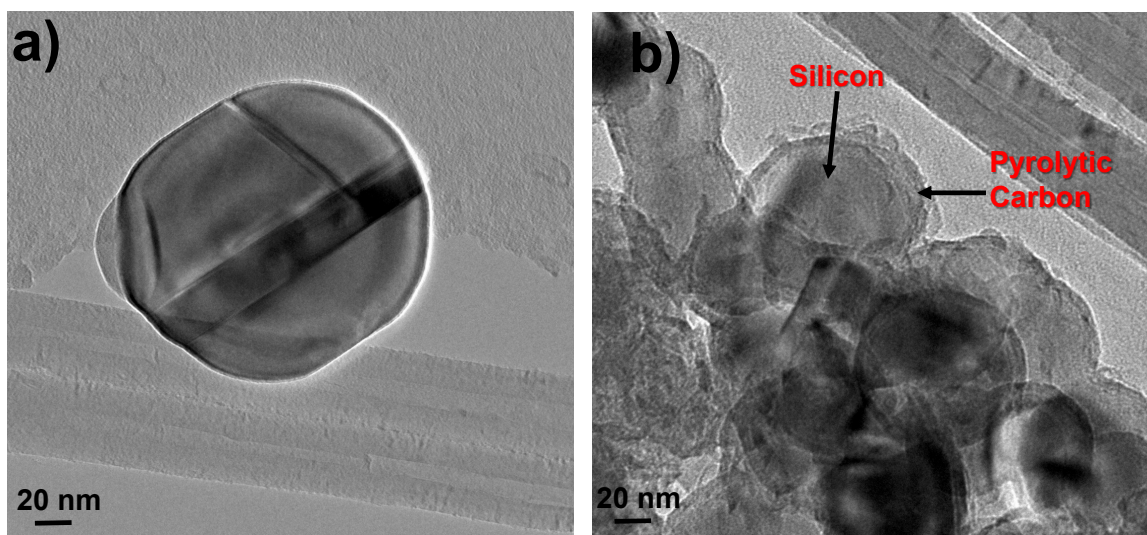


Figure 7.4 TEM images of flexible, novel structures (a) CNT-Si sheet and (b) CNT-Si-C sheet hybrids.

The CNT-Si and pyrolytic carbon coated CNT-Si-C sheet hybrids were further investigated by Raman spectroscopy and X-ray diffraction (XRD). Figure 7.5a shows the peak around 520 cm^{-1} which is related to the silicon Raman phonon vibration. The typical characteristic Si peaks between 480 to 520 cm^{-1} depend on silicon's crystalline size^[245–247]. As the crystalline size increases, the crystalline Si peak shifts to higher wave number, so the sharp Si peaks centered at 520 cm^{-1} reveal the crystalline Si peaks for both CNT-Si and CNT-

Si-C hybrids. Two characteristic carbon peaks are shown on Raman spectra as D-band (1360 cm^{-1}), which is associated with sp^3 bonded amorphous carbon or interstitial defects^[248], and the other one is the G-band (1582 cm^{-1}), indicating the in-plane stretching vibration mode of E_{2g} graphitic crystallites of carbon^[248,249]. The relative intensity ratio (i.e., R-value) of D-band to G-band is used to define the degree of disorder in the structure^[248,249]. Typically, a larger R-value indicates a higher degree of disorder in the structure. As shown in Figure 7.5b, the pristine CNT sheets showed a low D/G ratio (D/G value 0.42) that indicated a graphitic nature of large diameter multiwall CNTs. The R value of novel CNT-Si and CNT-Si-C hybrids are 0.52 and 0.88 respectively. This indicates that the novel CNT-Si-C hybrid is more disordered than the CNT-Si hybrid, which confirms the disordered carbon coating.

The XRD analyses of CNT-Si and pyrolytic carbon coated CNT-Si-C hybrids are shown in Figure 7.5c. The similar diffraction peaks were indexed for these hybrids. Diffraction peaks at 2θ of 29° , 47° , 56° , 69° , 76° , and 88° represent the (111), (220), (311), (400), (311), and (422) planes of Si crystals, respectively^[250,251]. However the pyrolytic carbon coating weakened the intensities of Si peaks for CNT-Si-C hybrid as seen in Figure 7.5. The weak and broad diffraction peak at around $2\theta = 25^\circ$, which could be indexed as the (002) planes, was ascribed to be disordered pyrolytic carbon structure^[56,252,253]. The disordered carbon structure was further confirmed by Raman spectroscopy.

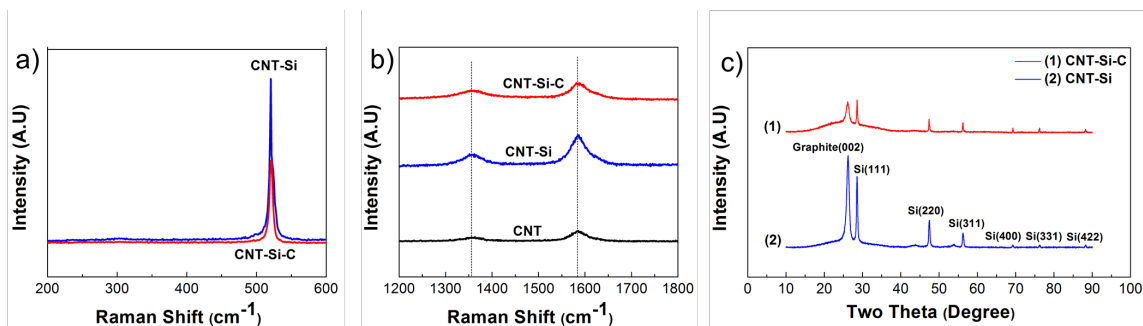


Figure 7.5 (a) Raman spectra of novel CNT-Si and CNT-Si-C sheet hybrids to examine characteristic Si peaks, (b) Raman spectra of novel CNT-Si and CNT-Si-C sheet hybrids to examine characteristic carbon peaks, (c) WAXD patterns of flexible novel (1) CNT-Si-C sheet and (2) CNT-Si sheet hybrids.

In order to evaluate the electrochemical performance of as-prepared hybrid anodes, galvanostatic charge-discharge tests were conducted between 0.1 to 2.0 V at a constant current density of 100 mA g^{-1} . The specific capacities of all electrodes were calculated based on the total mass of hybrid anodes including Si, CNTs, and carbon coating. Figure 7.6 shows the galvanostatic charge-discharge profiles for the first, second and hundredth cycles of CNTs sheets, CNT-Si and CNT-Si-C hybrids. The first-cycle discharge capacities were 207.8, 1973.3, and 1985.9 mAh g^{-1} , respectively, for CNTs sheets and CNT-Si and CNT-Si-C hybrids (Figure 7.6) with coulombic efficiency of 99, 70.2, and 73.85 respectively. Because CNT sheets were composed of only carbon without the Si component, the first cycle discharge capacity of the CNT sheets was much lower than those of CNT-Si and CNT-Si-C hybrids. For the CNTs, the initial discharge and charge capacities reached 207.8 and 206 mAh g^{-1} , respectively, with a coulombic efficiency of 99%. At the second cycle, the charge capacity reduced to 201.2 mAh g^{-1} with a capacity loss of 2.4% (Figure 7.6). On the other

hand, the CNT-Si hybrid showed discharge and charge capacities of 1973.3 and 1433 mAh g⁻¹, respectively, with a coulombic efficiency of 70.2% for the first cycle. The charge capacity of the CNT-Si hybrid decreased to 1427 mAh g⁻¹ with a 0.5 % capacity loss at the second cycle. Initial discharge and charge capacities of the CNT-Si-C hybrid were 1985.9 and 1470 mAh g⁻¹, respectively, with a coulombic efficiency of 73.9%. At the second cycle, the charge capacity of the CNT-Si-C hybrid decreased to 1460.8 mAh g⁻¹ with a 0.007% capacity loss, which was the smallest capacity loss among all electrodes studied. At the 100th cycle, discharge capacities of the CNTs and CNT-Si and CNT-Si-C hybrids decreased to 178.8, 224.4, and 1341.2 mAh g⁻¹, respectively (Figure 7.6). From Figure 7.6, it was also seen that at the first cycle, the CNT-Si hybrid exhibited a long voltage plateau at around 0.2 V; however, this voltage plateau was shortened after CVD carbon coating. The voltage plateau at around 0.2 V could be attributed to the alloying reaction of lithium with silicon particles.

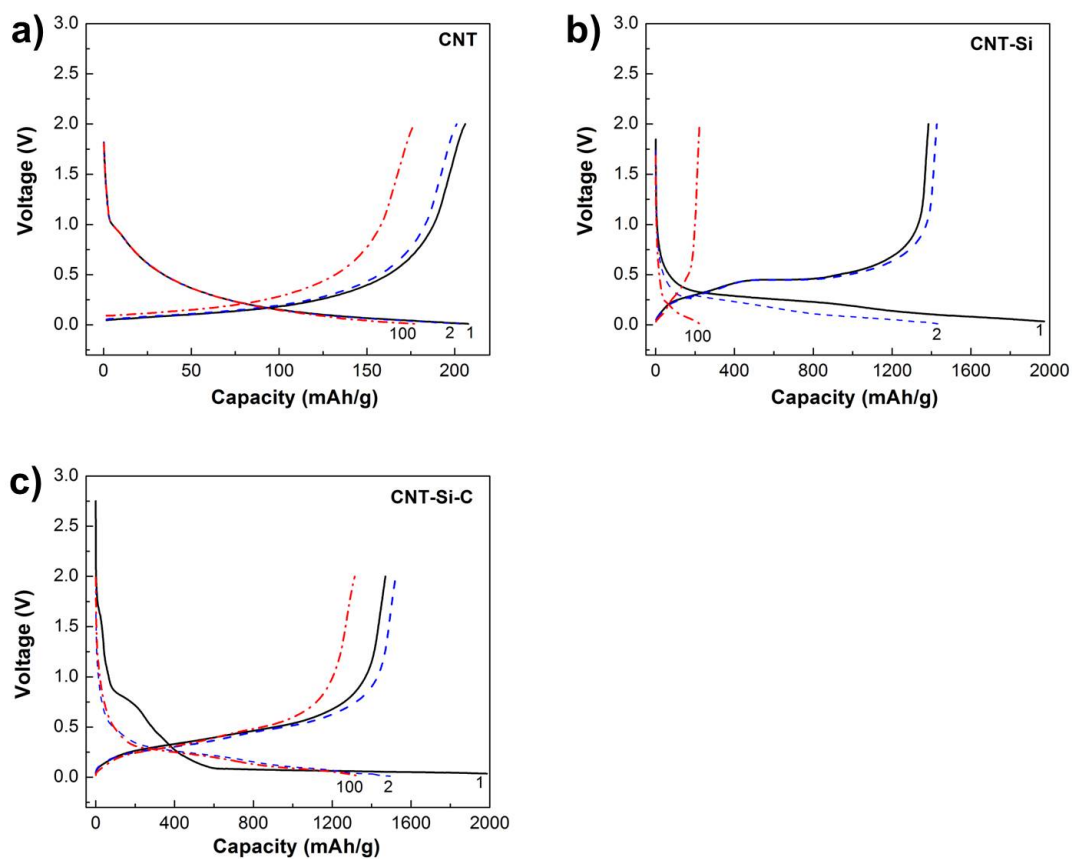


Figure 7.6 Galvanostatic charge-discharge profiles of novel (a) CNT sheet, (b) CNT-Si sheet, and (c) CNT-Si-C sheet composites.

The cycling performance and coulombic efficiency of CNT-Si composite and CVD pyrolytic carbon coated CNT-Si-C hybrid was compared in Figure 7.7. For comparison, the cycling performance of CNTs sheet is also shown in Figure 7.7 since it gives an estimate on how much of the capacity comes from carbon portion of the hybrids. It is seen that for the 150th cycle, the capacity of the CNTs sheet was around $163.9 \text{ mA}g^{-1}$ and the corresponding capacity retention was 79.5%. Cycling performance results showed that for CNT sheet, relatively stable cycling performance and lower capacity was achieved due to the absence of

active Si ingredient. On the other hand, very poor cycling performance was observed for CNT-Si hybrid even though they provided much higher initial capacity than the CNTs sheets. It is seen from Figure 7.7 that at the 150th cycle, the capacity of the CNT-Si hybrid was around 191.3 mAh g⁻¹. Capacity retention and coulombic efficiency of CNT-Si hybrid at the 150th cycle were around 13.3% and 99.1%, respectively. Results demonstrated that although the introduction of Si led to apparent improvement the capacity, the cycling performance of CNT-Si hybrid was not satisfactory due to the insufficient attachment of Si nanoparticles within the CNTs sheets. Therefore the active Si nanoparticles directly contacted electrolyte during electrochemical cycling, which caused serious pulverization and accelerated the formation of SEI. In addition due to the insufficient attachment of Si nanoparticles within the CNT sheet, structural integrity could not be protected during cycling and the Si nanoparticles could not contribute the future cycling performance.

From Figure 7.7, it is seen that the cycling performance of CNT-Si hybrid was improved significantly by CVD pyrolytic carbon coating. The capacity retention and coulombic efficiency of CNT-Si-C hybrid was around 87.8 % and 99%, respectively, at the 150th cycle. This result demonstrated that the nanoscale CVD pyrolytic carbon coating enhanced the attachment of Si nanoparticles within the CNTs sheets and helped maintain the structural integrity of the electrode during the cycling process. The CVD carbon-coating layer also supported more stable SEI growth by preventing direct contact of the electrolyte with the active Si material. Similar effects of nanoscale carbon coating have been observed by Fu, et al., who obtained improved cycling stability for nanoscale CVD carbon-coated electrospun Si/C nanofiber composite anodes^[56].

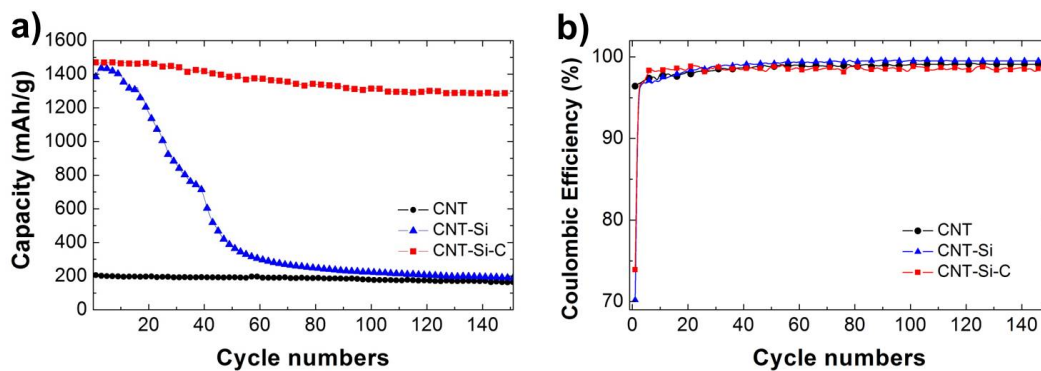


Figure 7.7 Cycling performances and coulombic efficiencies of CNT sheet, CNT-Si, and CNT-Si-C sheet hybrids.

Among the all three samples, the CNT-Si-C hybrid samples had the best cycling performance at high rates. The rate capability of CNT-Si-C sheet was examined under different current densities. The average charge capacity values of CNT-Si-C sheet under 100, 200, 400, and 800 mA g^{-1} were around 1471, 1320, 942, and 721 mA g^{-1} , respectively. The coulombic efficiency remained stable as the current density increased. After repeated cycles at higher current densities, the capacity returned to 1460 mA g^{-1} when the current density was reverted back to 100 mA g^{-1} . The charge capacity (1460 mA g^{-1}) was very close to initial charge capacity, demonstrating the good rate capability of CVD pyrolytic carbon coated novel CNT-Si-C sheet.

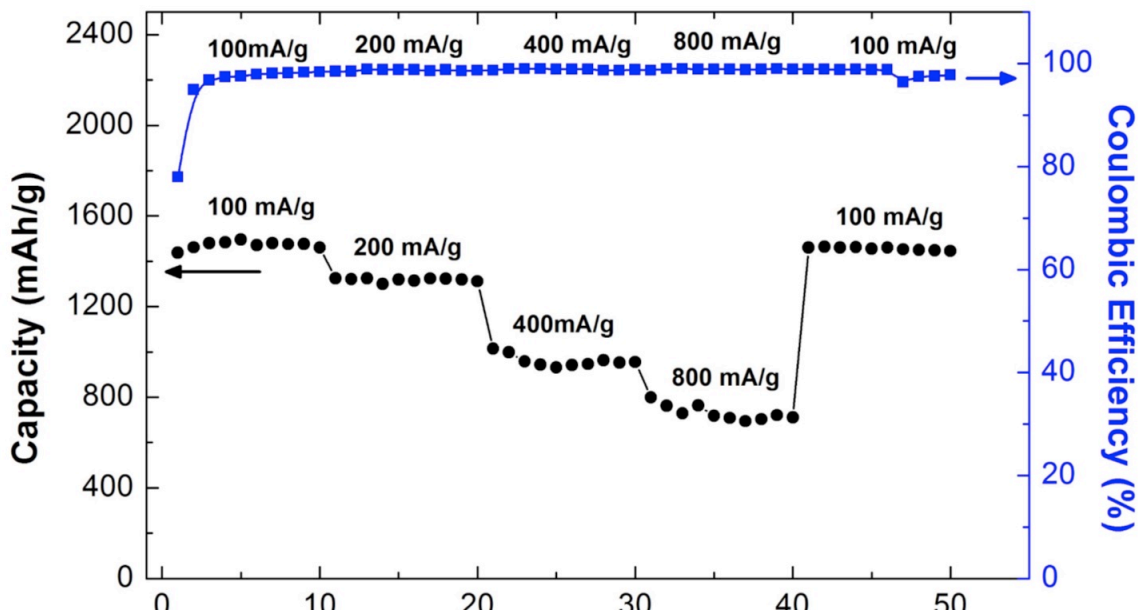


Figure 7.8 Rate capability and coulombic efficiency of CVD pyrolytic carbon coated novel CNT-Si-C sheet hybrid cycled at different current densities.

7.4 Conclusions

Freestanding CNT-Si-C sheet hybrids with a novel architecture were prepared as binder-free anodes for LIBs by a CNT-PMMA-Si hybridization method and decomposition of PMMA electrospun fibers, followed by a CVD pyrolytic carbon coating. This structure is flexible and binder free, and it has sufficient space for volume expansion of Si nanoparticles during cycling. It was found that the CVD pyrolytic carbon coating improved initial coulombic efficiency and stabilized the SEI formation. The pyrolytic carbon coating was also able to enhance mechanical bonding between CNTs and Si in order to constrain Si

nanoparticles in their original locations. This helped maintain the structural stability of electrodes, which led to higher capacity and improved cycle performance. The novel CNT-Si-C sheet hybrid exhibited excellent properties in terms of cycle performance (1285 mAhg⁻¹ at 150th cycle), coulombic efficiency (98%), and capacity retention (88%) after 150 cycles. This novel design can be extended for other materials that suffer from large volume change issues during energy storage.

Chaper 8 Final Conclusions and Future Work

8.1 Conclusions

Research discoveries surrounding the integration of CNT sheets with micro and nano-sized fiber nonwoven textile materials have only begun to explore. The aligned CNT sheets have provided significant improvements in a more diverse range of applications. The objective of the research conducted in this dissertation can be divided in two parts: 1) to explore the effect of drawing aligned CNT sheet in aerosol filtration by embedding them between traditional nonwoven fabrics, 2) to create a novel process to produce nanoscale nonwovens through hybridization of aligned CNT sheet and electrospun fabrics to explore them in aerosol filtration, protective garment and energy storage applications. The followings are a collection of outcomes and conclusions generated from the body of this work.

- Integration aligned CNT sheets with micro-sized fiber nonwoven fabrics are useful technique for preparation high performance aerosol filters. Since CNT sheets have small diameters, low basis weight, low packing density and high porosity, these sheets are a great candidate for air filtration structures. The results showed that integration of aligned CNT sheets either parallel or cross-ply configuration between micro-sized fiber polypropylene nonwoven fabrics exhibited huge increases in aerosol filtration efficiency, and the 3-layer cross-ply structure reached (HEPA) filter criteria. These novel CNT filters have filtration properties that are comparable to electrospun fabrics, making them a viable option for future filtration applications.

- Fabricating multi-layer structure using CNT sheets and micro-sized fiber nonwovens were prepared to evaluate aerosol filtration characteristics. To protect CNT sheets from bundling during winding process, 3-separated layer CNTs multi-layer structures were prepared. The results showed that the architecture of CNT sheet is important and that further improvements could be made through further engineering the multi-layered fabric structure. In addition, fabric porosity
- Stable nanoscale hybrid fabrics, containing both polymer nanofibers and separate and distinct carbon nanotubes (CNTs), were created by simultaneously electrospinning polyethylene oxide (PEO) nanofibers onto aligned CNT sheets which were drawn and collected on a grounded, rotating mandrel. This novel hybridization process addressed all the limitations which could not be succeeded in previous studies, so the hybrids showed high tensile strength, very small pore size, high specific surface area, and electrical conductivity. The calendered hybrids remained still porous and look similar to thermally spot bonded nonwoven fabrics. The hybrids showed excellent aerosol filtration and barrier fabric properties. In this study, PEO was utilized as the polymer nanofiber in these hybrid fabrics, however, the technology can easily be extended to many other polymer/fiber systems in future studies.
- Due to high porosity and electrical conductivity, hybrid fabric processing method was used to prepare silicon-carbon nanotube (CNT) hybrid anode architecture. The flexible and binder free hybrid structure has sufficient space for volume expansion of Si nanoparticles during cycling. The pyrolytic carbon coating enhanced mechanical bond between CNTs and Si nanoparticles, which helped maintain the structural

stability of electrodes and stabilized solid-electrolyte-interface (SEI) formation. The novel CNT-Si-C sheet hybrid exhibited improved performance in terms of excellent cycling capacity, high coulombic efficiency, and good capacity retention.

8.2 Future Work

Research on the aerosol filtration properties of aligned CNT sheets-nonwoven fabric structures was presented in chapters 4 & 5. The results showed that aligned CNT sheets, with individual CNT diameters 25–40 nm, calculated packing density of 6.5×10^{-4} , and thickness of 20 μm , significantly improved filtration efficiency at reasonable pressure drop. Due to the small diameter of CNTs, 3-layer cross-ply structure reached HEPA filter standards at relatively lower pressure drop than the other nano-sized fiber filters in literature.

Higher filtration efficiency and lower pressure drop are obtained when the fiber diameter is smaller than the gas mean free path, which is achieved at the FMF regime. For this reason air filtration in the FMF regime is significant, but challenging. With the current technology, small fiber diameters, less than 100 nm, cannot be produced, so pressure and temperature were adjusted in previous research in order to understand how filtration characteristics change in the FMF regime. Therefore, future research is necessary that will use the smaller diameter aligned CNT sheets to reach the FMF regime, thus showing how aerosol filtration characteristics will change under the standard conditions of the regime.

A novel process of nanoscale nonwovens, produced through the hybridization of CNTs and electrospun fabrics, was presented in chapter 6. The results from chapter 6 showed that the CNT – PEO electrospun hybrids exhibited extremely high tensile strength, small pore

size, high specific surface area, and electrical conductivity. The hybrids remained porous even after calendaring, and the fabric's strength increased significantly due to the better bonding and interactions with the CNTs. In addition, the hybrids exhibited very good aerosol filtration and excellent barrier properties. In this process, the hybrids were created in such a way that the entire CNT sheet layers formed in parallel to each other. Therefore, the hybrids' tensile strength improved only in one direction. Further research is needed to prepare cross-ply hybrid structures with different configuration, such as 2x2, 3x3 or 5x5, to investigate the mechanical, the particle filtration and the barrier properties of hybrids.

The hybridization technique utilized in my research was further examined by changing the electrospun polymer solution, which is discussed in chapter 7. Through the sequence of a CNT-PMMA-Si hybridization method, the decomposition of PMMA electrospun fibers, and a CVD pyrolytic carbon coating, freestanding CNT-Si-C sheet hybrids were prepared as binder-free anodes for LIBs. The results showed that the CNT-Si-C hybrid exhibited excellent properties in terms of cycle performance (1285 mAhg^{-1} at 150th cycle), coulombic efficiency (98%), and capacity retention (88%) after 150 cycles. Importantly, in this study, 30% Si nanoparticles was deposited in the hybrid structure. Thus, future research needs to investigate the effects of Si nanoparticle percent in the hybrid structure on cycle performance, coulombic efficiency, and capacity retention. In addition, it should be studied how pyrolytic carbon deposition time affects capacity and coulombic efficiency of hybrid fabric.

To sum up, the new hybrid fabric processing method introduced by this research was investigated in three main applications: aerosol filtration, barrier fabric, and energy storage. The results showed that this new processing technique exhibited significant advantages in each of these applications. This implies that this is a promising method which, if explored further, can lead to new discoveries in changing the polymer/fiber systems and eventually create improvements in a more diverse range of applications.

REFERENCES

- [1] J. Fang, X. Wang, T. Li, in *Nanofibers - Prod. Prop. Funct. Appl.* (Ed.: T. Lin), InTech, **2011**.
- [2] S. Ramakrishna, K. Fujihara, W.-E. Teo, T. Yong, Z. Ma, R. Ramaseshan, *Mater. Today* **2006**, *9*, 40.
- [3] S. Rodríguez, X. Querol, A. Alastuey, M.-M. Viana, M. Alarcón, E. Mantilla, C. R. Ruiz, *Sci. Total Environ.* **2004**, *328*, 95.
- [4] X. Querol, A. Alastuey, S. Rodriguez, F. Plana, E. Mantilla, C. R. Ruiz, *Atmos. Environ.* **2001**, *35*, 845.
- [5] M. Kampa, E. Castanas, *Environ. Pollut.* **2008**, *151*, 362.
- [6] C. A. P. III, D. W. Dockery, *J. Air Waste Manag. Assoc.* **2006**, *56*, 709.
- [7] M. N. Moore, *Environ. Int.* **2006**, *32*, 967.
- [8] W. Peukert, *Filtr. Sep.* **1998**, *35*, 461.
- [9] N. T. Kim Oanh, N. Upadhyay, Y.-H. Zhuang, Z.-P. Hao, D. V. S. Murthy, P. Lestari, J. T. Villarin, K. Chengchua, H. X. Co, N. T. Dung, E. S. Lindgren, *Atmos. Environ.* **2006**, *40*, 3367.
- [10] C. Wang, Y. Otani, *Ind. Eng. Chem. Res.* **2013**, *52*, 5.
- [11] O. Yildiz, P. D. Bradford, *Carbon* **2013**, *64*, 295.
- [12] W. W.-F. Leung, C.-H. Hung, P.-T. Yuen, *Sep. Purif. Technol.* **2010**, *71*, 30.
- [13] J. Wang, S. C. Kim, D. Y. H. Pui, *J. Aerosol Sci.* **2008**, *39*, 323.
- [14] J. H. Park, K. Y. Yoon, H. Na, Y. S. Kim, J. Hwang, J. Kim, Y. H. Yoon, *Sci. Total Environ.* **2011**, *409*, 4132.
- [15] K. Graham, M. Ouyang, T. Raether, T. Grafe, B. McDonald, P. Knauf, in *Fifteenth Annu. Tech. Conf. Expo Am. Filtr. Sep. Soc. Galvest. Tex.*, **2002**, pp. 9–12.
- [16] S. Zhang, W. S. Shim, J. Kim, *Mater. Des.* **2009**, *30*, 3659.
- [17] B. Ding, J. Yu, *Electrospun Nanofibers for Energy and Environmental Applications*, Springer, **2014**.
- [18] L. Huang, J. T. Arena, S. S. Manickam, X. Jiang, B. G. Willis, J. R. McCutcheon, *J. Membr. Sci.* **2014**, *460*, 241.
- [19] X. Wang, K. Zhang, M. Zhu, B. S. Hsiao, B. Chu, *Macromol. Rapid Commun.* **2008**, *29*, 826.
- [20] Y. Lee, B.-S. Kim, J. H. Hong, S. Park, H. Kim, I.-S. Kim, *J. Polym. Res.* **2012**, *19*, 1.
- [21] G. H. Kim, *Biomed. Mater.* **2008**, *3*, 025010.

- [22] J. Liu, Z. Yue, H. Fong, *Small* **2009**, *5*, 536.
- [23] R. Sen, B. Zhao, D. Perea, M. E. Itkis, H. Hu, J. Love, E. Bekyarova, R. C. Haddon, *Nano Lett.* **2004**, *4*, 459.
- [24] G. M. Kim, R. Lach, G. H. Michler, P. Pötschke, K. Albrecht, *Nanotechnology* **2006**, *17*, 963.
- [25] J. J. Mack, L. M. Viculis, A. Ali, R. Luoh, G. Yang, H. T. Hahn, F. K. Ko, R. B. Kaner, *Adv. Mater.* **2005**, *17*, 77.
- [26] H. Liao, R. Qi, M. Shen, X. Cao, R. Guo, Y. Zhang, X. Shi, *Colloids Surf. B Biointerfaces* **2011**, *84*, 528.
- [27] S. Mazinani, A. Ajji, C. Dubois, *Polymer* **2009**, *50*, 3329.
- [28] S. Mazinani, A. Ajji, C. Dubois, *J. Polym. Sci. Part B Polym. Phys.* **2010**, *48*, 2052.
- [29] G. Wang, Z. Tan, X. Liu, S. Chawda, J.-S. Koo, V. Samuilov, M. Dudley, *Nanotechnology* **2006**, *17*, 5829.
- [30] G. Mathew, J. P. Hong, J. M. Rhee, H. S. Lee, C. Nah, *Polym. Test.* **2005**, *24*, 712.
- [31] S. Iijima, others, *nature* **1991**, *354*, 56.
- [32] L. Liu, W. Ma, Z. Zhang, *Small* **2011**, *7*, 1504.
- [33] Z. Ren, Y. Lan, Y. Wang, *Aligned Carbon Nanotubes: Physics, Concepts, Fabrication and Devices*, Springer Science & Business Media, **2012**.
- [34] M. S. Dresselhaus, G. Dresselhaus, R. Saito, *Carbon* **1995**, *33*, 883.
- [35] J. P. Lu, *Phys. Rev. Lett.* **1997**, *79*, 1297.
- [36] E. T. Thostenson, Z. Ren, T.-W. Chou, *Compos. Sci. Technol.* **2001**, *61*, 1899.
- [37] C. Journet, W. K. Maser, P. Bernier, A. Loiseau, M. L. de la Chapelle, S. Lefrant, P. Deniard, R. Lee, J. E. Fischer, *Nature* **1997**, *388*, 756.
- [38] C. D. Scott, S. Arepalli, P. Nikolaev, R. E. Smalley, *Appl. Phys. A* **2001**, *72*, 573.
- [39] C. J. Lee, D. W. Kim, T. J. Lee, Y. C. Choi, Y. S. Park, Y. H. Lee, W. B. Choi, N. S. Lee, G.-S. Park, J. M. Kim, *Chem. Phys. Lett.* **1999**, *312*, 461.
- [40] J. Kong, A. M. Cassell, H. Dai, *Chem. Phys. Lett.* **1998**, *292*, 567.
- [41] E. Couteau, K. Hernadi, J. W. Seo, L. Thiên-Nga, C. Mikó, R. Gaál, L. Forró, *Chem. Phys. Lett.* **2003**, *378*, 9.
- [42] A. Grüneis, M. H. Rummeli, C. Kramberger, A. Barreiro, T. Pichler, R. Pfeiffer, H. Kuzmany, T. Gemming, B. Büchner, *Carbon* **2006**, *44*, 3177.
- [43] S. B. Sinnott, R. Andrews, D. Qian, A. M. Rao, Z. Mao, E. C. Dickey, F. Derbyshire, *Chem. Phys. Lett.* **1999**, *315*, 25.
- [44] P. M. Ajayan, *Chem. Rev.* **1999**, *99*, 1787.

- [45] H. Yoshida, S. Takeda, T. Uchiyama, H. Kohno, Y. Homma, *Nano Lett.* **2008**, *8*, 2082.
- [46] C. J. Lee, J. Park, J. A. Yu, *Chem. Phys. Lett.* **2002**, *360*, 250.
- [47] C. H. See, A. T. Harris, *Ind. Eng. Chem. Res.* **2007**, *46*, 997.
- [48] K. Jiang, Q. Li, S. Fan, *Nature* **2002**, *419*, 801.
- [49] C. P. Huynh, S. C. Hawkins, *Carbon* **2010**, *48*, 1105.
- [50] X. Zhang, K. Jiang, C. Feng, P. Liu, L. Zhang, J. Kong, T. Zhang, Q. Li, S. Fan, *Adv. Mater.* **2006**, *18*, 1505.
- [51] S. Fan, M. G. Chapline, N. R. Franklin, T. W. Tombler, A. M. Cassell, H. Dai, *Science* **1999**, *283*, 512.
- [52] Y. Wei, K. Jiang, X. Feng, P. Liu, L. Liu, S. Fan, *Phys. Rev. B* **2007**, *76*, 045423.
- [53] A. E. Aliev, C. Guthy, M. Zhang, S. Fang, A. A. Zakhidov, J. E. Fischer, R. H. Baughman, *Carbon* **2007**, *45*, 2880.
- [54] R. S. Prasher, X. J. Hu, Y. Chalopin, N. Mingo, K. Lofgreen, S. Volz, F. Cleri, P. Keblinski, *Phys. Rev. Lett.* **2009**, *102*, 105901.
- [55] J.-H. Kim, K. H. Lee, L. J. Overzet, G. S. Lee, *Nano Lett.* **2011**, *11*, 2611.
- [56] K. Fu, O. Yildiz, H. Bhanushali, Y. Wang, K. Stano, L. Xue, X. Zhang, P. D. Bradford, *Adv. Mater.* **2013**, *25*, 5109.
- [57] A. E. Aliev, J. Oh, M. E. Kozlov, A. A. Kuznetsov, S. Fang, A. F. Fonseca, R. Ovalle, M. D. Lima, M. H. Haque, Y. N. Gartstein, M. Zhang, A. A. Zakhidov, R. H. Baughman, *Science* **2009**, *323*, 1575.
- [58] C. D. Williams, R. O. Robles, M. Zhang, S. Li, R. H. Baughman, A. A. Zakhidov, *Appl. Phys. Lett.* **2008**, *93*, 183506.
- [59] L. Xiao, Z. Chen, C. Feng, L. Liu, Z.-Q. Bai, Y. Wang, L. Qian, Y. Zhang, Q. Li, K. Jiang, S. Fan, *Nano Lett.* **2008**, *8*, 4539.
- [60] X. Wang, Z. Z. Yong, Q. W. Li, P. D. Bradford, W. Liu, D. S. Tucker, W. Cai, H. Wang, F. G. Yuan, Y. T. Zhu, *Mater. Res. Lett.* **2012**, *1*, 19.
- [61] Y. Jia, J. Wei, K. Wang, A. Cao, Q. Shu, X. Gui, Y. Zhu, D. Zhuang, G. Zhang, B. Ma, others, *Adv Mater* **2008**, *20*, 4594.
- [62] Y. Jia, A. Cao, F. Kang, P. Li, X. Gui, L. Zhang, E. Shi, J. Wei, K. Wang, H. Zhu, D. Wu, *Phys. Chem. Chem. Phys.* **2012**, *14*, 8391.
- [63] O. US EPA, “Health | Particulate Matter | Air & Radiation | US EPA,” can be found under <http://www.epa.gov/air/particlepollution/health.html>, **n.d.**
- [64] Y. Song, Y. Zhang, S. Xie, L. Zeng, M. Zheng, L. G. Salmon, M. Shao, S. Slanina, *Atmos. Environ.* **2006**, *40*, 1526.
- [65] C. D. O’Dowd, P. Aalto, K. Hmeri, M. Kulmala, T. Hoffmann, *Nature* **2002**, *416*, 497.

- [66] W. C. Hinds, *Aerosol Technology: Properties, Behavior, and Measurement of Airborne Particles*, J. Wiley, New York, **c1982**.
- [67] P. Li, C. Wang, Y. Zhang, F. Wei, *Small* **2014**, *10*, 4543.
- [68] W. C. Hinds, *Aerosol Technology: Properties, Behavior, and Measurement of Airborne Particles*, Wiley, **1999**.
- [69] B. Maze, H. Vahedi Tafreshi, Q. Wang, B. Pourdeyhimi, *J. Aerosol Sci.* **2007**, *38*, 550.
- [70] “CDC - NIOSH Publications and Products - Guidance for Filtration and Air-Cleaning Systems to Protect Building Environments from Airborne Chemical, Biological, or Radiological Attacks (2003-136),” can be found under <http://www.cdc.gov/niosh/docs/2003-136/>, **n.d.**
- [71] S. K. Batra, *The Nonwoven Fabrics Handbook*, INDA, Association Of The Nonwoven Fabrics Industry, **1999**.
- [72] I. M. Hutten, *Handbook of Nonwoven Filter Media*, Elsevier, **2007**.
- [73] J. Kim, *Investigation on Charge Deterioration of Electrically Charged Filter Media Using Electric Force Microscopy*, North Carolina State University, **2005**.
- [74] J. G. Adiletta, *Fibrous Nonwoven Web*, **1999**, US5954962 A.
- [75] D. Zhang, C. (Qin) Sun, H. Song, *J. Appl. Polym. Sci.* **2004**, *94*, 1218.
- [76] B. Y. Yeom, B. Pourdeyhimi, *J. Mater. Sci.* **2011**, *46*, 5761.
- [77] S. Tanaka, A. Doi, N. Nakatani, Y. Katayama, Y. Miyake, *Carbon* **2009**, *47*, 2688.
- [78] D. Wang, G. Sun, B.-S. Chiou, *Macromol. Mater. Eng.* **2007**, *292*, 407.
- [79] P. Qiu, C. Mao, *ACS Nano* **2010**, *4*, 1573.
- [80] Y. C. Ahn, S. K. Park, G. T. Kim, Y. J. Hwang, C. G. Lee, H. S. Shin, J. K. Lee, *Curr. Appl. Phys.* **2006**, *6*, 1030.
- [81] G. T. Kim, Y. C. Ahn, J. K. Lee, *Korean J. Chem. Eng.* **2008**, *25*, 368.
- [82] B. Y. Yeom, E. Shim, B. Pourdeyhimi, *Macromol. Res.* **2010**, *18*, 884.
- [83] P. P. Tsai, H. Schreuder-Gibson, P. Gibson, *J. Electrostat.* **2002**, *54*, 333.
- [84] P. Gupta, C. Elkins, T. E. Long, G. L. Wilkes, *Polymer* **2005**, *46*, 4799.
- [85] N. Zhu, X. Che, in *Adv. Biomater. Sci. Biomed. Appl.* (Ed.: R. Pignatello), InTech, **2013**.
- [86] D. Hussain, F. Loyal, A. Greiner, J. H. Wendorff, *Polymer* **2010**, *51*, 3989.
- [87] J. Yao, C. Bastiaansen, T. Peijs, *Fibers* **2014**, *2*, 158.
- [88] C.-H. Hung, W. W.-F. Leung, *Sep. Purif. Technol.* **2011**, *79*, 34.
- [89] A. N. Karwa, B. J. Tatarchuk, *Sep. Purif. Technol.* **2012**, *87*, 84.

- [90] G. Viswanathan, D. B. Kane, P. J. Lipowicz, *Adv. Mater.* **2004**, *16*, 2045.
- [91] S. J. Park, D. G. Lee, *Carbon* **2006**, *44*, 1930.
- [92] S. J. Park, D. G. Lee, *Curr. Appl. Phys.* **2006**, *6*, Supplement 1, e182.
- [93] P. Li, Y. Zong, Y. Zhang, M. Yang, R. Zhang, S. Li, F. Wei, *Nanoscale* **2013**, *5*, 3367.
- [94] A. G. Nasibulin, A. Kaskela, K. Mustonen, A. S. Anisimov, V. Ruiz, S. Kivistö, S. Rackauskas, M. Y. Timmermans, M. Pudas, B. Aitchison, M. Kauppinen, D. P. Brown, O. G. Okhotnikov, E. I. Kauppinen, *ACS Nano* **2011**, *5*, 3214.
- [95] A. Moisala, A. G. Nasibulin, D. P. Brown, H. Jiang, L. Khriachtchev, E. I. Kauppinen, *Chem. Eng. Sci.* **2006**, *61*, 4393.
- [96] A. G. Nasibulin, P. V. Pikhitsa, H. Jiang, D. P. Brown, A. V. Krasheninnikov, A. S. Anisimov, P. Queipo, A. Moisala, D. Gonzalez, G. Lientschnig, A. Hassanien, S. D. Shandakov, G. Lolli, D. E. Resasco, M. Choi, D. Tománek, E. I. Kauppinen, *Nat. Nanotechnol.* **2007**, *2*, 156.
- [97] P. Li, C. Wang, Z. Li, Y. Zong, Y. Zhang, X. Yang, S. Li, F. Wei, *RSC Adv.* **2014**, *4*, 54115.
- [98] N. Halonen, A. Rautio, A.-R. Leino, T. Kyllönen, G. Tóth, J. Lappalainen, K. Kordás, M. Huuhtanen, R. L. Keiski, A. Sápi, M. Szabó, Á. Kukovecz, Z. Kónya, I. Kiricsi, P. M. Ajayan, R. Vajtai, *ACS Nano* **2010**, *4*, 2003.
- [99] K.-T. Park, J. Hwang, *Carbon* **2014**, *75*, 401.
- [100] C. Wang, P. Li, Y. Zong, Y. Zhang, S. Li, F. Wei, *Carbon* **2014**, *79*, 424.
- [101] R. C. Brown, *Air Filtration: An Integrated Approach to the Theory and Applications of Fibrous Filters*, Elsevier Science Limited, **1993**.
- [102] K. R. Spurny, *Advances in Aerosol Gas Filtration*, CRC Press, **1998**.
- [103] S. Kuwabara, *J. Phys. Soc. Jpn.* **1959**, *14*, 527.
- [104] J. Happel, *AIChE J.* **1959**, *5*, 174.
- [105] K. W. Lee, B. Y. H. Liu, *Aerosol Sci. Technol.* **1982**, *1*, 147.
- [106] I. B. Stechkina, N. A. Fuchs, *Ann. Occup. Hyg.* **1966**, *9*, 59.
- [107] K. Spurný, *Aerosols Physical Chemistry and Applications*, Gordon And Breach, **1965**.
- [108] C. N. Davies, *Air Filtration*, Academic Press, **1973**.
- [109] S. Dhaniyala, B. Y. H. Liu, *Aerosol Sci. Technol.* **2001**, *34*, 170.
- [110] S. Fotovati, H. Vahedi Tafreshi, B. Pourdeyhimi, *Chem. Eng. Sci.* **2010**, *65*, 5285.
- [111] J. P. Shi, D. E. Evans, A. A. Khan, R. M. Harrison, *Atmos. Environ.* **2001**, *35*, 1193.
- [112] J. Wang, S. C. Kim, D. Y. H. Pui, *Aerosol Sci. Technol.* **2008**, *42*, 722.

- [113] M. Huysmans, A. Dassargues, *Hydrogeol. J.* **2004**, *13*, 895.
- [114] B. Y. Yeom, B. Pourdeyhimi, *J. Mater. Sci.* **2011**, *46*, 3252.
- [115] C. Cercignani, in *Boltzmann Equ. Its Appl.*, Springer New York, **1988**, pp. 40–103.
- [116] S. V. Hering, S. K. Friedlander, J. J. Collins, L. W. Richards, *Environ. Sci. Technol.* **1979**, *13*, 184.
- [117] Z. Zhang, B. Y. H. Liu, *Aerosol Sci. Technol.* **1992**, *16*, 227.
- [118] Q. Wang, *An Investigation of Aerosol Filtration via Fibrous Filters*, North Carolina State University, **2007**.
- [119] D. J. Rader, *J. Aerosol Sci.* **1990**, *21*, 161.
- [120] J. Pich, *J. Colloid Interface Sci.* **1971**, *37*, 912.
- [121] Z.-M. Huang, Y.-Z. Zhang, M. Kotaki, S. Ramakrishna, *Compos. Sci. Technol.* **2003**, *63*, 2223.
- [122] J. Zeng, X. Xu, X. Chen, Q. Liang, X. Bian, L. Yang, X. Jing, *J. Controlled Release* **2003**, *92*, 227.
- [123] K. Y. Lee, L. Jeong, Y. O. Kang, S. J. Lee, W. H. Park, *Adv. Drug Deliv. Rev.* **2009**, *61*, 1020.
- [124] H. Cho, S.-Y. Min, T.-W. Lee, *Macromol. Mater. Eng.* **2013**, *298*, 475.
- [125] T. Courtney, M. S. Sacks, J. Stankus, J. Guan, W. R. Wagner, *Biomaterials* **2006**, *27*, 3631.
- [126] H. Hou, J. J. Ge, J. Zeng, Q. Li, D. H. Reneker, A. Greiner, S. Z. D. Cheng, *Chem. Mater.* **2005**, *17*, 967.
- [127] S. Z. Wu, F. Zhang, X. X. Hou, X. P. Yang, *Adv. Mater. Res.* **2008**, *47-50*, 1169.
- [128] Z. Spitalsky, D. Tasis, K. Papagelis, C. Galiotis, *Prog. Polym. Sci.* **2010**, *35*, 357.
- [129] C. Huang, S. Chen, D. H. Reneker, C. Lai, H. Hou, *Adv. Mater.* **2006**, *18*, 668.
- [130] L. Cao, D. Su, Z. Su, X. Chen, *Ind. Eng. Chem. Res.* **2014**, *53*, 2308.
- [131] W. Wang, P. Ciselli, E. Kuznetsov, T. Peijs, A. H. Barber, *Philos. Trans. R. Soc. Lond. Math. Phys. Eng. Sci.* **2008**, *366*, 1613.
- [132] L.-Q. Liu, D. Tasis, M. Prato, H. D. Wagner, *Adv. Mater.* **2007**, *19*, 1228.
- [133] D. Chen, T. Liu, X. Zhou, W. C. Tjiu, H. Hou, *J. Phys. Chem. B* **2009**, *113*, 9741.
- [134] X.-M. Sui, S. Giordani, M. Prato, H. D. Wagner, *Appl. Phys. Lett.* **2009**, *95*, 233113.
- [135] K. A. Narh, L. Jallo, K. Y. Rhee, *Polym. Compos.* **2008**, *29*, 809.
- [136] M. V. Jose, B. W. Steinert, V. Thomas, D. R. Dean, M. A. Abdalla, G. Price, G. M. Janowski, *Polymer* **2007**, *48*, 1096.

- [137] J. Ji, G. Sui, Y. Yu, Y. Liu, Y. Lin, Z. Du, S. Ryu, X. Yang, *J. Phys. Chem. C* **2009**, *113*, 4779.
- [138] S. D. McCullen, D. R. Stevens, W. A. Roberts, S. S. Ojha, L. I. Clarke, R. E. Gorga, *Macromolecules* **2007**, *40*, 997.
- [139] S. S. Ojha, D. R. Stevens, K. Stano, T. Hoffman, L. I. Clarke, R. E. Gorga, *Macromolecules* **2008**, *41*, 2509.
- [140] K. H. Lee, H. Y. Kim, M. S. Khil, Y. M. Ra, D. R. Lee, *Polymer* **2003**, *44*, 1287.
- [141] D. H. Reneker, I. Chun, *Nanotechnology* **1996**, *7*, 216.
- [142] P. Lu, Y.-L. Hsieh, *ACS Appl. Mater. Interfaces* **2010**, *2*, 2413.
- [143] B. Dunn, H. Kamath, J.-M. Tarascon, *Science* **2011**, *334*, 928.
- [144] M. Winter, R. J. Brodd, *Chem. Rev.* **2004**, *104*, 4245.
- [145] J.-M. Tarascon, M. Armand, *Nature* **2001**, *414*, 359.
- [146] P. G. Bruce, B. Scrosati, J.-M. Tarascon, *Angew. Chem. Int. Ed.* **2008**, *47*, 2930.
- [147] L. Ji, Z. Lin, M. Alcoutlabi, X. Zhang, *Energy Environ. Sci.* **2011**, *4*, 2682.
- [148] M. Armand, J.-M. Tarascon, *Nature* **2008**, *451*, 652.
- [149] J.-M. Tarascon, *Philos. Trans. R. Soc. Lond. Math. Phys. Eng. Sci.* **2010**, *368*, 3227.
- [150] M. Dirican, M. Yanilmaz, K. Fu, O. Yildiz, H. Kizil, Y. Hu, X. Zhang, *J. Electrochem. Soc.* **2014**, *161*, A2197.
- [151] M. Dirican, O. Yildiz, Y. Lu, X. Fang, H. Jiang, H. Kizil, X. Zhang, *Electrochimica Acta* **2015**, *169*, 52.
- [152] Q. Zhang, W. Zhang, W. Wan, Y. Cui, E. Wang, *Nano Lett.* **2010**, *10*, 3243.
- [153] X. Zhang, L. Ji, O. Toprakci, Y. Liang, M. Alcoutlabi, *Polym. Rev.* **2011**, *51*, 239.
- [154] H. Wu, G. Chan, J. W. Choi, I. Ryu, Y. Yao, M. T. McDowell, S. W. Lee, A. Jackson, Y. Yang, L. Hu, Y. Cui, *Nat. Nanotechnol.* **2012**, *7*, 310.
- [155] T. H. Hwang, Y. M. Lee, B.-S. Kong, J.-S. Seo, J. W. Choi, *Nano Lett.* **2012**, *12*, 802.
- [156] X. H. Liu, L. Zhong, S. Huang, S. X. Mao, T. Zhu, J. Y. Huang, *ACS Nano* **2012**, *6*, 1522.
- [157] M. Dirican, O. Yildiz, Y. Lu, X. Fang, H. Jiang, H. Kizil, X. Zhang, *Electrochimica Acta* **2015**, *169*, 52.
- [158] B. Lestriez, *Comptes Rendus Chim.* **2010**, *13*, 1341.
- [159] C. de las Casas, W. Li, *J. Power Sources* **2012**, *208*, 74.
- [160] X.-M. Liu, Z. dong Huang, S. woon Oh, B. Zhang, P.-C. Ma, M. M. F. Yuen, J.-K. Kim, *Compos. Sci. Technol.* **2012**, *72*, 121.

- [161] wei wang, P. N. kumta, *ACS Nano* **n.d.**, 2233.
- [162] Y. Fan, Q. Zhang, C. Lu, Q. Xiao, X. Wang, B. kang Tay, *Nanoscale* **2013**, *5*, 1503.
- [163] Y. Fan, Q. Zhang, Q. Xiao, X. Wang, K. Huang, *Carbon* **2013**, *59*, 264.
- [164] L.-F. Cui, L. Hu, J. W. Choi, Y. Cui, *ACS Nano* **n.d.**, 3671.
- [165] S.-L. Chou, Y. Zhao, J.-Z. Wang, Z.-X. Chen, H.-K. Liu, S.-X. Dou, *J. Phys. Chem. C* **2010**, *114*, 15862.
- [166] S. Miller-Leiden, C. Lohascio, W. W. Nazaroff, J. M. Macher, *J. Air Waste Manag. Assoc.* **1996**, *46*, 869.
- [167] J. (Jim) Zhang, K. R. Smith, *Br. Med. Bull.* **2003**, *68*, 209.
- [168] A. P. Jones, *Atmos. Environ.* **1999**, *33*, 4535.
- [169] K. R. Smith, *Indoor Air* **2002**, *12*, 198.
- [170] I. Oren, N. Haddad, R. Finkelstein, J. M. Rowe, *Am. J. Hematol.* **2001**, *66*, 257.
- [171] T. H. Grafe, K. M. Graham, in *Nonwovens Filtr.-Fifth Int. Conf. Stuttg. Ger.*, **2003**, pp. 1–5.
- [172] K. Desai, K. Kit, J. Li, P. Michael Davidson, S. Zivanovic, H. Meyer, *Polymer* **2009**, *50*, 3661.
- [173] K. M. Yun, C. J. Hogan Jr., Y. Matsubayashi, M. Kawabe, F. Iskandar, K. Okuyama, *Chem. Eng. Sci.* **2007**, *62*, 4751.
- [174] H. J. Patel, S. Kwon, *J. Expo. Sci. Environ. Epidemiol.* **2013**, *23*, 101.
- [175] J. Kayat, V. Gajbhiye, R. K. Tekade, N. K. Jain, *Nanomedicine Nanotechnol. Biol. Med.* **2011**, *7*, 40.
- [176] A. Liu, K. Sun, J. Yang, D. Zhao, *J. Nanoparticle Res.* **2008**, *10*, 1303.
- [177] J. Muller, F. Huaux, D. Lison, *Carbon* **2006**, *44*, 1048.
- [178] H. Peng, M. Jain, D. E. Peterson, Y. Zhu, Q. Jia, *Small* **2008**, *4*, 1964.
- [179] A. Ghemes, Y. Minami, J. Muramatsu, M. Okada, H. Mimura, Y. Inoue, *Carbon* **2012**, *50*, 4579.
- [180] Y. Luo, Z. Gong, M. He, X. Wang, Z. Tang, H. Chen, *Sol. Energy Mater. Sol. Cells* **2012**, *97*, 78.
- [181] W. Liu, H. Zhao, Y. Inoue, X. Wang, P. D. Bradford, H. Kim, Y. Qiu, Y. Zhu, *Compos. Part Appl. Sci. Manuf.* **2012**, *43*, 587.
- [182] X. Wang, P. J. Krommenhoek, P. D. Bradford, B. Gong, J. B. Tracy, G. N. Parsons, T.-J. M. Luo, Y. T. Zhu, *ACS Appl. Mater. Interfaces* **2011**, *3*, 4180.
- [183] Y. Inoue, K. Kakihata, Y. Hirono, T. Horie, A. Ishida, H. Mimura, *Appl. Phys. Lett.* **2008**, *92*, 213113.

- [184] A. Podgórski, A. Bałazy, L. Gradoń, *Chem. Eng. Sci.* **2006**, *61*, 6804.
- [185] X.-H. Qin, S.-Y. Wang, *J. Appl. Polym. Sci.* **2006**, *102*, 1285.
- [186] L. Li, M. W. Frey, T. B. Green, *J. Eng. Fibers Fabr.* **2006**, *1*, 1.
- [187] B. Mazé, H. V. Tafreshi, B. Pourdeyhimi, *J. Eng. Fibers Fabr.* **2008**, *3*, 7.
- [188] R. S. Barhate, S. Ramakrishna, *J. Membr. Sci.* **2007**, *296*, 1.
- [189] N. Wang, Y. Si, N. Wang, G. Sun, M. El-Newehy, S. S. Al-Deyab, B. Ding, *Sep. Purif. Technol.* **n.d.**, *126*, 44.
- [190] O. Yildiz, K. Stano, S. Faraji, C. Stone, C. Willis, X. Zhang, J. S. Jur, P. D. Bradford, *Nanoscale* **2015**, *7*, 16744.
- [191] S. S. Homaeigohar, K. Buhr, K. Ebert, *J. Membr. Sci.* **2010**, *365*, 68.
- [192] R. Gopal, S. Kaur, Z. Ma, C. Chan, S. Ramakrishna, T. Matsuura, *J. Membr. Sci.* **2006**, *281*, 581.
- [193] L. Chen, L. Bromberg, H. Schreuder-Gibson, J. Walker, T. A. Hatton, G. C. Rutledge, *J. Mater. Chem.* **2009**, *19*, 2432.
- [194] R. Bagherzadeh, M. Latifi, S. S. Najar, M. A. Tehran, M. Gorji, L. Kong, *Text. Res. J.* **2012**, *82*, 70.
- [195] B. Ding, E. Kimura, T. Sato, S. Fujita, S. Shiratori, *Polymer* **2004**, *45*, 1895.
- [196] C.-L. Pai, M. C. Boyce, G. C. Rutledge, *Polymer* **2011**, *52*, 6126.
- [197] J.-S. Kim, D. H. Reneker, others, *Polym. Eng. Sci.* **1999**, *39*, 849.
- [198] J. H. Hong, E. H. Jeong, H. S. Lee, D. H. Baik, S. W. Seo, J. H. Youk, *J. Polym. Sci. Part B Polym. Phys.* **2005**, *43*, 3171.
- [199] Z. Ma, M. Kotaki, S. Ramakrishna, *J. Membr. Sci.* **2006**, *272*, 179.
- [200] M. Kang, H.-J. Jin, *Colloid Polym. Sci.* **2007**, *285*, 1163.
- [201] A. Agic, B. Mijovic, *J. Text. Inst.* **2006**, *97*, 419.
- [202] J. S. Jeong, S. Y. Jeon, T. Y. Lee, J. H. Park, J. H. Shin, P. S. Alegaonkar, A. S. Berdinsky, J. B. Yoo, *Diam. Relat. Mater.* **2006**, *15*, 1839.
- [203] L. Y. Yeo, J. R. Friend, *J. Exp. Nanosci.* **2006**, *1*, 177.
- [204] S. Faraji, K. Stano, C. Rost, J.-P. Maria, Y. Zhu, P. D. Bradford, *Carbon* **2014**, *79*, 113.
- [205] J. H. Kim, M. Kataoka, Y. C. Jung, Y.-I. Ko, K. Fujisawa, T. Hayashi, Y. A. Kim, M. Endo, *ACS Appl. Mater. Interfaces* **2013**, *5*, 4150.
- [206] S. Limem, S. B. Warner, *Text. Res. J.* **2005**, *75*, 63.
- [207] H. S. Kim, B. Pourdeyhimi, P. Desai, A. S. Abhiraman, *Text. Res. J.* **2001**, *71*, 965.

- [208] J.-H. Lin, Z.-H. Xu, C.-H. Lei, C.-W. Lou, *Text. Res. J.* **2003**, 73, 917.
- [209] K. Smith, A. A. Ogale, R. Maugans, L. K. Walsh, R. M. Patel, *Text. Res. J.* **2003**, 73, 845.
- [210] D. Zhang, G. Bhat, M. Sanjiv, L. Wadsworth, *Text. Res. J.* **1998**, 68, 27.
- [211] A. Rawal, S. Lomov, T. Ngo, I. Verpoest, J. Vankerrebrouck, *Text. Res. J.* **2007**, 77, 417.
- [212] X. Hou, M. Acar, V. V. Silberschmidt, *J. Eng. Fibers Fabr.* **2009**, 4, 26.
- [213] M. Naebe, T. Lin, W. Tian, L. Dai, X. Wang, *Nanotechnology* **2007**, 18, 225605.
- [214] S. Ramaswamy, L. I. Clarke, R. E. Gorga, *Polymer* **2011**, 52, 3183.
- [215] B. Yoon, S. Lee, *Fibers Polym.* **2011**, 12, 57.
- [216] S. Lee, S. Kay Obendorf, *J. Appl. Polym. Sci.* **2006**, 102, 3430.
- [217] S. Lee, S. K. Obendorf, *Text. Res. J.* **2007**, 77, 696.
- [218] S. Lee, S. K. Obendorf, *Fibers Polym.* **2007**, 8, 501.
- [219] H. J. Lee, C. R. Willis, C. A. Stone, *J. Mater. Sci.* **2011**, 46, 3907.
- [220] S. R. Coulson, I. S. Woodward, J. P. S. Badyal, S. A. Brewer, C. Willis, *Chem. Mater.* **2000**, 12, 2031.
- [221] S. R. Coulson, I. S. Woodward, J. P. S. Badyal, S. A. Brewer, C. Willis, *Langmuir* **2000**, 16, 6287.
- [222] E. J. Kinmond, S. R. Coulson, J. P. S. Badyal, S. A. Brewer, C. Willis, *Polymer* **2005**, 46, 6829.
- [223] C. Tarducci, E. J. Kinmond, J. P. S. Badyal, S. A. Brewer, C. Willis, *Chem. Mater.* **2000**, 12, 1884.
- [224] D. A. Lamprou, J. R. Smith, T. G. Nevell, E. Barbu, C. Stone, C. R. Willis, J. Tsibouklis, *Appl. Surf. Sci.* **2010**, 256, 5082.
- [225] S. A. Brewer, C. R. Willis, *Appl. Surf. Sci.* **2008**, 254, 6450.
- [226] R. Saraf, H. J. Lee, S. Michielsen, J. Owens, C. Willis, C. Stone, E. Wilusz, *J. Mater. Sci.* **2011**, 46, 5751.
- [227] H. Bellanger, T. Darmanin, E. Taffin de Givenchy, F. Guittard, *Chem. Rev.* **2014**, 114, 2694.
- [228] "Dressed for combat," can be found under <http://www.soci.org/chemistry-and-industry/cni-data/2009/7/dressed-for-combat>, **n.d.**
- [229] J. B. Goodenough, Y. Kim, *Chem. Mater.* **2010**, 22, 587.
- [230] J. R. Dahn, T. Zheng, Y. Liu, J. S. Xue, *Science* **1995**, 270, 590.

- [231] H. Wu, G. Zheng, N. Liu, T. J. Carney, Y. Yang, Y. Cui, *Nano Lett.* **2012**, *12*, 904.
- [232] B.-S. Lee, S.-B. Son, K.-M. Park, J.-H. Seo, S.-H. Lee, I.-S. Choi, K.-H. Oh, W.-R. Yu, *J. Power Sources* **2012**, *206*, 267.
- [233] D. S. Jung, T. H. Hwang, S. B. Park, J. W. Choi, *Nano Lett.* **2013**, *13*, 2092.
- [234] S. Chen, M. L. Gordin, R. Yi, G. Howlett, H. Sohn, D. Wang, *Phys. Chem. Chem. Phys.* **2012**, *14*, 12741.
- [235] H. Li, H. Zhou, *Chem Commun* **2012**, *48*, 1201.
- [236] L. Su, Y. Jing, Z. Zhou, *Nanoscale* **2011**, *3*, 3967.
- [237] K. Evanoff, J. Benson, M. Schauer, I. Kovalenko, D. Lashmore, W. J. Ready, G. Yushin, *ACS Nano* **2012**, *6*, 9837.
- [238] K. Fu, L. Xue, O. Yildiz, S. Li, H. Lee, Y. Li, G. Xu, L. Zhou, P. D. Bradford, X. Zhang, *Nano Energy* **2013**, *2*, 976.
- [239] K. Evanoff, J. Khan, A. A. Balandin, A. Magasinski, W. J. Ready, T. F. Fuller, G. Yushin, *Adv. Mater.* **2012**, *24*, 533.
- [240] C. de las Casas, W. Li, *J. Power Sources* **2012**, *208*, 74.
- [241] K. Wang, S. Luo, Y. Wu, X. He, F. Zhao, J. Wang, K. Jiang, S. Fan, *Adv. Funct. Mater.* **2013**, *23*, 846.
- [242] Q. Zhang, J.-Q. Huang, W.-Z. Qian, Y.-Y. Zhang, F. Wei, *Small* **2013**, *9*, 1237.
- [243] S. Faraji, K. L. Stano, O. Yildiz, A. Li, Y. Zhu, P. D. Bradford, *Nanoscale* **2015**, *7*, 17038.
- [244] K. L. Stano, R. Chapla, M. Carroll, J. Nowak, M. McCord, P. D. Bradford, *ACS Appl. Mater. Interfaces* **2013**, *5*, 10774.
- [245] R. Epur, M. K. Datta, P. N. Kumta, *Electrochimica Acta* **2012**, *85*, 680.
- [246] R. L. C. Vink, G. T. Barkema, W. F. van der Weg, *Phys. Rev. B* **2001**, *63*, 115210.
- [247] C. Smit, R. A. C. M. M. van Swaaij, H. Donker, A. M. H. N. Petit, W. M. M. Kessels, M. C. M. van de Sanden, *J. Appl. Phys.* **2003**, *94*, 3582.
- [248] C. Kim, S.-H. Park, J.-I. Cho, D.-Y. Lee, T.-J. Park, W.-J. Lee, K.-S. Yang, *J. Raman Spectrosc.* **2004**, *35*, 928.
- [249] Y.-S. Ding, W.-N. Li, S. Iaconetti, X.-F. Shen, J. DiCarlo, F. S. Galasso, S. L. Suib, *Surf. Coat. Technol.* **2006**, *200*, 3041.
- [250] H. S. Choi, J. G. Lee, H. Y. Lee, S. W. Kim, C. R. Park, *Electrochimica Acta* **2010**, *56*, 790.
- [251] J. Xiao, W. Xu, D. Wang, D. Choi, W. Wang, X. Li, G. L. Graff, J. Liu, J.-G. Zhang, *J. Electrochem. Soc.* **2010**, *157*, A1047.

[252] L. Ji, X. Zhang, *Carbon* **2009**, *47*, 3219.

[253] M. Dirican, Y. Lu, Y. Ge, O. Yildiz, X. Zhang, *ACS Appl. Mater. Interfaces* **2015**, *7*, 18387.